INVESTIGATING IMMUNE MODULATION OF MOLECULAR SUBTYPES OF BLADDER CANCER IN RESPONSE TO CHEMOTHERAPY

Jordan Kardos

A dissertation submitted to the faculty at the University of North Carolina at Chapel Hill in partial fulfillment of the requirements for the degree of Doctor of Philosophy in the Curriculum of Genetics and Molecular Biology

Chapel Hill
2018

Approved by:

William Kim

Ian Davis

Joel Parker

Cyrus Vaziri

Albert Baldwin

ABSTRACT

Jordan Kardos: Investigating immune modulation of molecular subtypes of bladder cancer in response to chemotherapy
(Under the direction of William Kim)

Urinary bladder cancer is the ninth most common malignancy, with ~77,000 new cases and ~16,000 deaths in the United States annually. Muscle-invasive bladder cancer has been described as a heterogeneous disease and several groups have identified intrinsic molecular subtypes. Here, we characterize the claudin-low, molecular subtype of high-grade bladder cancer. Claudin-low bladder tumors are defined by high levels of epithelial-to-mesenchymal transition (EMT), enrichment for tumor initiating cell (TIC) signatures, and low expression levels of tight-junction claudins. Furthermore, we find that claudin-low tumors are highly enriched across all immune gene signatures examined, but also express high levels of immune checkpoint molecules. In contrast to melanoma and non–small-cell lung cancer, the predicted neoantigen burden does not correlate with immune infiltration in bladder cancer.

Standard of care for muscle invasive bladder cancer is combination, platinum-based chemotherapy; however treatment with immune checkpoint inhibitors has also been shown to be effective in both platinum refractory as well as platinum ineligible patients. We describe the comprehensive genomic characterization of urachal adenocarcinoma and the first report of global RNA expression profiling of urachal tumors. We find that urachal tumors molecularly resemble colorectal cancer at the level

of gene expression and validate previous reports that have shown that urachal tumors harbor genomic alterations in *KRAS*, *APC*, and *SMAD2/SMAD4* found in colorectal cancer. Our transcriptome studies reinforce the notion from genomic studies that urachal adenocarcinomas resemble colorectal cancer. We further report that these rare tumors have mutations in DNA Mismatch Repair (MMR) proteins and *POLE* and describe the successful treatment of a patient with the anti–PD-L1 antibody atezolizumab. Our studies and case report highlight the potential utility of precision oncology in rare tumor types that have no clear standard of care therapy.

Finally, we describe the effects of cisplatin-based chemotherapy on the tumor microenvironment. We find that Gemcitabine and Cisplatin (GemCis) and Methotrexate, Vinblastine, Adriamycin, and Cisplatin (MVAC) treatment, the two main frontline chemotherapeutic regimens approved for muscle invasive bladder cancer, have differing effects on the tumor microenvironment and that the luminal and basal molecular subtypes have different responses to therapy. MVAC treatment in luminal tumors in particular induces significantly higher levels of immune infiltration and corresponding immune suppression than GemCis treatment. We further show that this effect appears to be induced by a misregulation of the cytokine expression and induction of EMT, and that methotrexate treatment alone, through its inhibition of dihydrofolate reductase, is sufficient to induce a mesenchymal and immune-infiltrated phenotype. In aggregate this work has important implications for how MVAC and GemCis are combined with immune checkpoint blockade.

To Nikolai and Andrea.

I will be forever grateful to both of you.

ACKNOWLEDGEMENTS

I would first of all like to thank my mentor William Kim, who has been just all around awesome for my entire time in his lab. He is a brilliant, enthusiastic scientist whose passion and dedication to research continue to inspire, and he has continuously pushed me to become a better scientist. My work would not have been possible without his continued guidance and mentorship.

I would also like to thank the members of my committee: Ian Davis, Joel Parker, Cyrus Vaziri, and Albert Baldwin. I would like to thank Joel for all of the times he has made time for me when I have not known how to properly implement a bioinformatic analysis pipeline and his guidance has been irreplaceable. Ian has been a great chair, supporting me throughout my time in the program and offering guidance when necessary. Cyrus and Al have provided countless insights and given invaluable advice along the way. Ben Vincent is basically an honorary member of my committee, as he has provided advice and his lab has helped with large components of the immune analysis across several projects, specifically Lisa Bixby. Tracy Rose has helped with the clinical components of several projects, and also let me stay at her house while I was working offsite from Philadelphia. This work would not have been possible without contributions from my collaborators David McConkey, Betsy Plimack, Peter Black, and the GenomeDx bioinformatics group.

I would also like to thank the members of the Genetics and Molecular Biology curriculum. Specifically John Cornett, who is just all around amazing at everything, and who has always been there to help with anything I've needed over the last 5 years.

Finally I would like to thank my lab mates; Bhavani Krishnan was a great mentor when I joined the lab before she moved on to bigger and better things. My work was built largely on the foundation laid by Jeff Damrauer. Ryoichi Saito developed several of the mouse models that were used across projects, and was vital to our lab winning several March Madness bracket pools. Jim Manocha has helped with a lot of the RNA Sequencing and downstream data analysis. Andrew Truong performed the in vitro analysis and was instrumental in the cell line and mouse work. And the Mouse Phase 1 Unit, specifically Kyle Stewart, performed the majority of the mouse experiments and were vital to the completion of this project.

TABLE OF CONTENTS

LIST OF FIGURES

LIST OF TABLES

CHAPTER 1: Molecular characterization of bladder cancer to better inform patient care

1.1 Clinical assessment of urothelial carcinoma

Urinary bladder cancer is the ninth most common malignancy, with ~77,000 new cases and ~16,000 deaths in the United States annually (1,2). Urothelial carcinomas originating from the epithelium make up the majority of bladder tumors, however variant histologies such as adenocarcinomas, small-cell carcinomas, and squamous cell carcinomas have been estimated to make up 10% of bladder cancer cases (3). Urothelial carcinoma can present as either non-muscle invasive (NMIBC) or muscle-invasive (MIBC) depending on whether the tumor has invaded into the muscularis propria (Figure 1.1). NMIBC patients have a 15-year disease-specific survival estimated at 74%-95% and as such generally respond well to standard of care transurethral resection and Bacillus Calmette-Guerin treatment (4). However, MIBC patients have a median survival of 28 months for standard of care neoadjuvant platinum-based combination chemotherapy followed by radical cystectomy treatment (5). Standard platinum-based chemotherapy for MIBC patient is a combination of Gemcitabine and Cisplatin (GemCis) regimen. However, a combination Methotrexate/ Vinblastine/ Adriamycin/ Cisplatin (MVAC) regimen was also commonly used and has been shown to have a similar survival benefit (3). As such, research has focused on improving the care and treatment of MIBC by better understanding the molecular mechanisms underlying the disease.

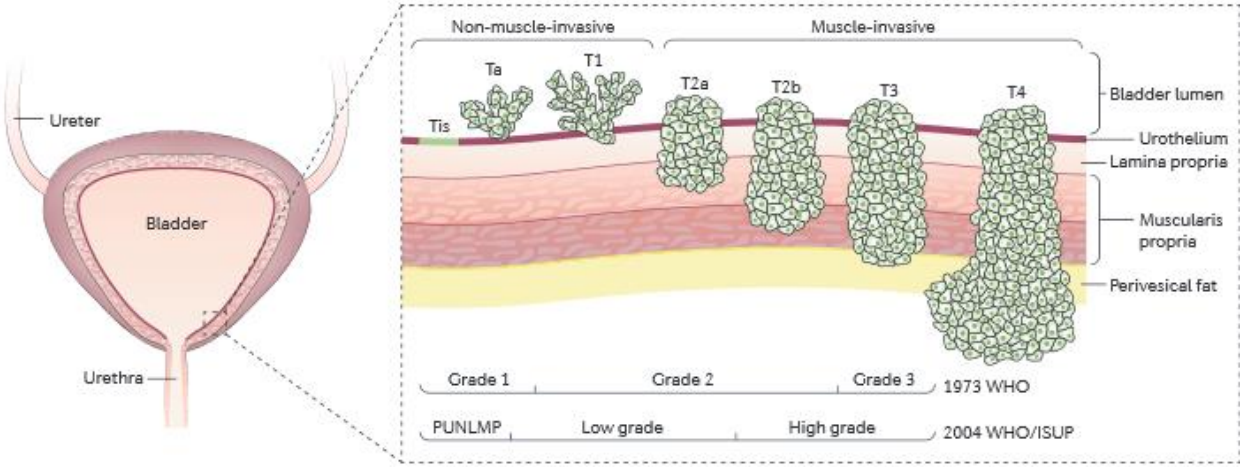

Figure 1.1: Bladder cancer staging: Identifying the progression of urothelial carcinoma from non-muscle invasive (Stage 0-I) to muscle-invasive (Stage II-IV) (7).

1.2 Identifying intrinsic molecular subtypes of bladder cancer

Muscle-invasive bladder cancer has been described as a heterogeneous disease, with several groups identifying intrinsic molecular subtypes within bladder cancer. Initial molecular characterization by Sjodahl et al identified 5 distinct subtypes of urothelial carcinoma: urobasal A, genomically unstable, urobasal B, squamous cell carcinoma like, and an infiltrated class (4). Follow-up work by both our group and the McConkey group identified an overarching basal-luminal subtyping scheme that is predictive of survival, with the McConkey group further identifying a chemo resistant p53-like subtype (5,6). In general, basal tumors present as more mesenchymal and aggressive, with a higher frequency of alterations in the RB1 and TP53 pathways, and have a significantly worse prognosis than luminal tumors. Furthermore The Cancer Genome Atlas (TCGA) group has done a comprehensive genomic and transcriptomic characterization of the molecular landscape of bladder cancer (7,8). The most recent TCGA publication has identified 5 distinct subtypes within the overarching basal/luminal

schema, and has characterized the alterations in cancer-related pathways associated with them (Figure 1.2).

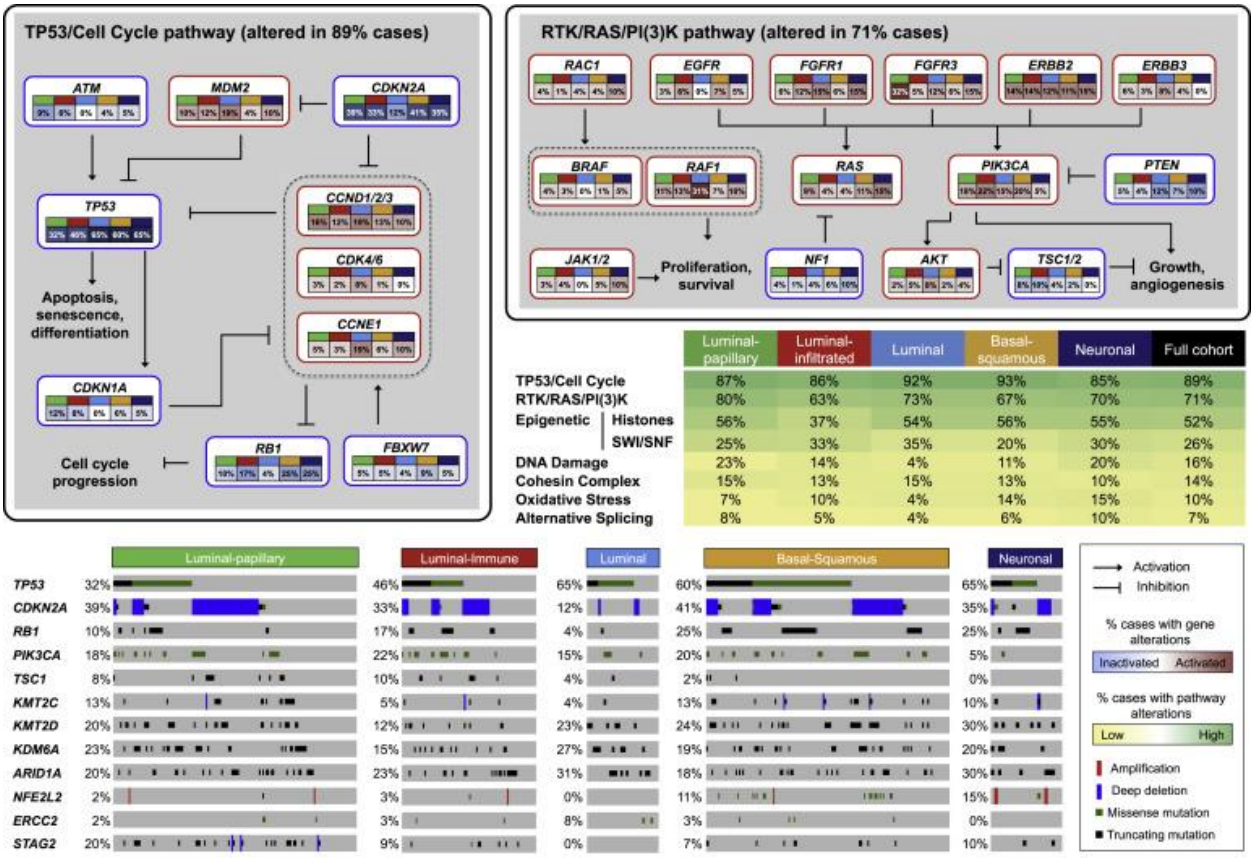

Figure 1.2: Genomic alterations in cancer related pathways across TCGA subtypes (7).

1.3 Immunotherapeutic cancer treatment

Over the last decade, a novel cancer treatment has been developed that has shown incredible promise across several tumor types collectively coined as immunotherapy. Immunotherapy harnesses the body's immune system to attack the tumor in treating a patient's tumor. While the collective terminology of immunotherapy currently describes 3 distinct treatment types: immune checkpoint inhibition, neoantigen vaccination, and Chimeric antigen receptor (CAR) T-cell therapy, the underlying

principle of augmenting an anti-tumor immune response to clear the tumor is the same across treatments.

In general, tumor cells, by their very nature, accumulate mutations at much higher rates than normal cells. Tumor cells can develop mutations in a peptide which is altered so that it binds to the class I Major Histocompatibility Complex (MHC) molecules and is presented to the immune system as a neoantigen (9). If the neoantigen is recognized and bound by a cytotoxic T-cell, the antigen presenting cell is targeted for degradation (16). Tumor cells can evade immune-targeted degradation by the cell-surface expression of immune checkpoint molecules. These molecules, as the name suggests, inhibit the immune response and allow the antigen presenting cell population to survive.

Each immunotherapeutic treatment targets a different component of the immune response. Immune checkpoint inhibitors are antibodies designed to bind to the immune checkpoint molecules expressed by tumors or immune cells and reinvigorate the immune response targeting the tumor cells, most commonly the PD-1/PD-L1 axis (17). Neoantigen vaccines involve sequencing the patient tumor, identifying mutations that could be recognized as neoantigens and injecting identified neoantigen peptides so that the immune system can more readily recognize them (18,19). CAR T-cell therapy involves isolating T-cells from cancer patients and genetically engineering the T-cells to produce receptors that recognize and attach to neoantigens specific to tumor cells. The modified cells are then reintroduced into the patient where they recognize and kill cancer cells that harbor the antigen on their surfaces (10). These treatments have been shown to be effective across a variety of tumor types (11-13).

1.4 Immunotherapy treatment in bladder cancer

In bladder cancer, treatment with the PD-L1 antibody atezolizumab was shown to be effective in a subset of patients, indicating that immune checkpoint inhibition could be a viable treatment (14). Interestingly, they found that response to treatment was positively correlated with both immune suppression in the tumor microenvironment as measured by PD-L1 expression, and tumor mutation burden. Follow-up studies of PD-L1 Ab treatment in bladder cancer have found that tumor-infiltrating lymphocytes, T-cell receptor clonality, and a post-treatment expansion of T-cell receptor clones is predictive of response (15). This is consistent with immune checkpoint inhibition treatment across other tumor types that have found several molecular characteristics to be predictive of response to treatment (16-20). The ongoing work in the field is working towards the goal of being able to tailor targeted therapies that we can predict patients will respond to, and design combination therapies to boost response in patients that would otherwise not respond to treatment.

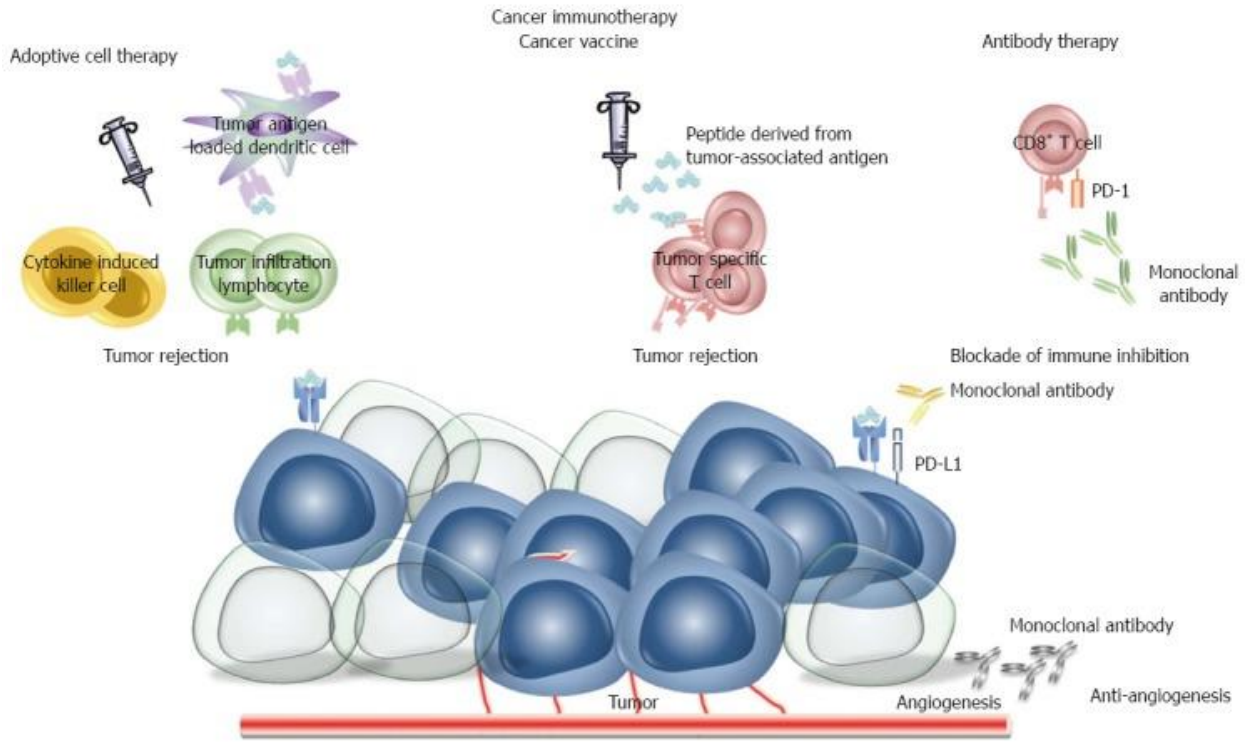

Figure 1.3: Cancer Immunotherapy Treatments (32).

1.5 Concluding remarks and contributions of this work

Bladder cancer has been shown by several groups to be a heterogeneous disease, and yet on a clinical level is still being treated uniformly. Here we hope to contribute to the field and show the validity of identifying intrinsic molecular differences within bladder cancer and the potential clinical implications of it. In Chapter 2, we identify a novel Claudin-low subtype of bladder cancer that we show to be more immune infiltrated and immune suppressed than both Basal and Luminal bladder tumors. In Chapter 3, we characterize the molecular landscape of urachal adenocarcinoma and show that the genomic and transcriptomic similarities to colorectal adenocarcinoma can prime urachal adenocarcinomas to respond to immune checkpoint inhibition. Finally, in Chapter 4, we show that there is a subtype-specific response to cisplatin-based

chemotherapeutic treatment. Specifically, that MVAC-treatment of luminal tumors induces higher levels of immune infiltration and immune suppression, and as these factors have been shown to correlate with response to immune checkpoint inhibition, could potentially prime these tumors to better respond to these treatments.

1.6 Thesis contributions

The work described in this thesis could not have been completed without contributions and help from many of my collaborators. The project described in Chapter 2 was a collaboration with the Ben Vincent Lab and the Bioinformatics Group headed by Joel Parker. The patient samples analyzed in Chapter 3 were obtained by Sara Wobker in collaboration with the UNC- Chapel Hill Oncology department. The project described in Chapter 4 was a collaboration with the Fox Chase Cancer Center, MD Anderson Cancer Center, and GenomeDx Biosciences with patient samples and data provided by each group.

CHAPTER 2: Identifying an immune infiltrated subtype of bladder cancer

2.1 Introduction

In the United States, bladder cancer is the fourth most common malignancy in men, with approximately 81,000 new cases and 17,000 deaths expected in 2018. Bladder cancer is histologically divided into low-grade or high-grade tumors that are associated with distinct genomic alterations and differences in prognosis (21). Low-grade tumors are almost uniformly noninvasive (Ta) and have a 5-year survival rate of 96%. In contrast, high-grade tumors can become muscle-invasive and metastatic and are associated with a 5-year survival rate ranging from 70% (muscle-invasive) to 5% (metastatic).

Multiple studies have now identified distinct RNA expression subtypes within both low- and high-grade bladder cancers (4-6,8,22-24). Building upon the work of our colleagues, we and others recently described distinct subtypes of high-grade muscle-invasive urothelial carcinoma (UC), luminal and basal, which reflect attributes of their corresponding breast cancer subtypes. These studies highlight the similarities in the underlying biology between breast and bladder cancer (5,6). In addition to the originally reported molecular subtypes of breast cancer (luminal A, luminal B, her2 enriched, and basal-like), a claudin-low subtype of breast cancer has been more recently identified and is characterized by a stromal phenotype, lack of luminal differentiation marker expression, enrichment for epithelial-to-mesenchymal transition (EMT) markers, cancer stem cell–like features, and immune response genes (25).

Clinical trials using immune checkpoint Abs targeting the PD1/PD-L1 axis have recently shown promise in a portion of patients with advanced UC, with the premise that activation of immune checkpoint pathways, including PD-L1, results in active immunosuppression (14,26-30). Despite the excitement surrounding PD1/PD-L1 axis inhibition in treating advanced UC, only approximately 20-30% of patients respond. Therefore, the majority of patients display intrinsic resistance to PD1/PD-L1 inhibition, and a priori identification of these patients would clearly be beneficial.

We report here the discovery of a claudin-low subtype of high-grade, muscle-invasive UC defined by biologic characteristics of the claudin-low subtype of breast cancer. Claudin-low tumors were uniformly enriched for immune gene signatures but simultaneously expressed immune checkpoint molecules, demonstrating that, despite being immune infiltrated, claudin-low tumors are also actively immunosuppressed. Interestingly, the predicted neoantigen burden was not significantly increased in claudin-low tumors. Instead, they highly expressed cytokines and chemokines associated with leukocyte chemotaxis into the tumor immune microenvironment as a result of an imbalance between PPARγ and NF-κB signaling. These results highlight the association between molecular subtype and the degree of immune infiltration and immune suppression and suggest that mechanisms other than neoantigen burden can drive the development of immune infiltrated tumors and also that claudin-low tumors are poised to respond to immune checkpoint inhibition.

2.2 Results

2.2.1 Identification of a claudin-low subtype in bladder cancer

Previous studies have identified a claudin-low molecular subtype of breast cancer (25). Given the previously documented similarities in gene expression patterns between breast and bladder cancer (5,6), we asked whether a claudin-low subtype also exists in bladder cancer. To this end, we performed unsupervised hierarchical clustering on 408 high-grade, muscle-invasive bladder tumors from The Cancer Genome Atlas (TCGA) urothelial bladder carcinoma (BLCA) data set using gene signatures representative of biologic characteristics that are known to define breast cancer claudin-low tumors such as an enrichment for tumor-initiating cells (TICs) and an EMT (Figure 2.1A) (25,31). Specifically, we used gene lists of the tight-junction claudins (*CLDN3*, *CLDN4*, and *CLDN7*) and a previously published bladder cancer–derived TIC signature (32). In addition, we derived a bidirectional (EMT_UP and EMT_DOWN), bladder cancer–specific, notch-dependent EMT gene signature from the publicly available Gene Expression Omnibus (GEO) gene expression data set (GEO GSE60564). Unsupervised hierarchical clustering with these gene signatures revealed a distinct cluster that had characteristics of a claudin low subtype (Figure 2.1A, highlighted in green).

To ensure that the set of tumors within the presumed claudin-low cluster were homogeneous and distinct from adjacent clusters of tumors, we performed a Gaussian distribution analysis, starting with the smallest cluster and iteratively repeated the analysis with the addition of adjacent clusters using SigClust software. This method identified a conserved node of 48 tumors that had consensus enrichment for claudin-low features, and these tumors were therefore defined as claudin-low. All 48 claudin-low

tumors were classified as basal by our BASE47 subtype classifier (Fisher's exact P = 1.18 × 10–16) (6), and when examined for their correlation to the BASE47 basal or luminal centroid, they were found to be highly basal (Figure 2.1B). Further supporting the notion that these tumors exhibit features of claudin-low breast cancer, we applied the previously defined breast cancer–specific claudin-low classifier to the TCGA BLCA tumors and found a significant enrichment (Fisher's exact P = 1.10 × 10–18) of the breast cancer–defined claudin-low tumors within the bladder claudin-low cluster. Given these findings, we propose a 3-subtype classification of bladder cancer consisting of basal (~40%), luminal (~50%), and claudin-low (~10%) tumors. While basal-like bladder cancer consistently has a worse clinical outcome (5,6,22,24), consistent with previous work on breast cancer (31), we did not find an observable significant difference in overall survival rates between patients with claudin-low tumors and those with basal tumors (Figure 2.1C).

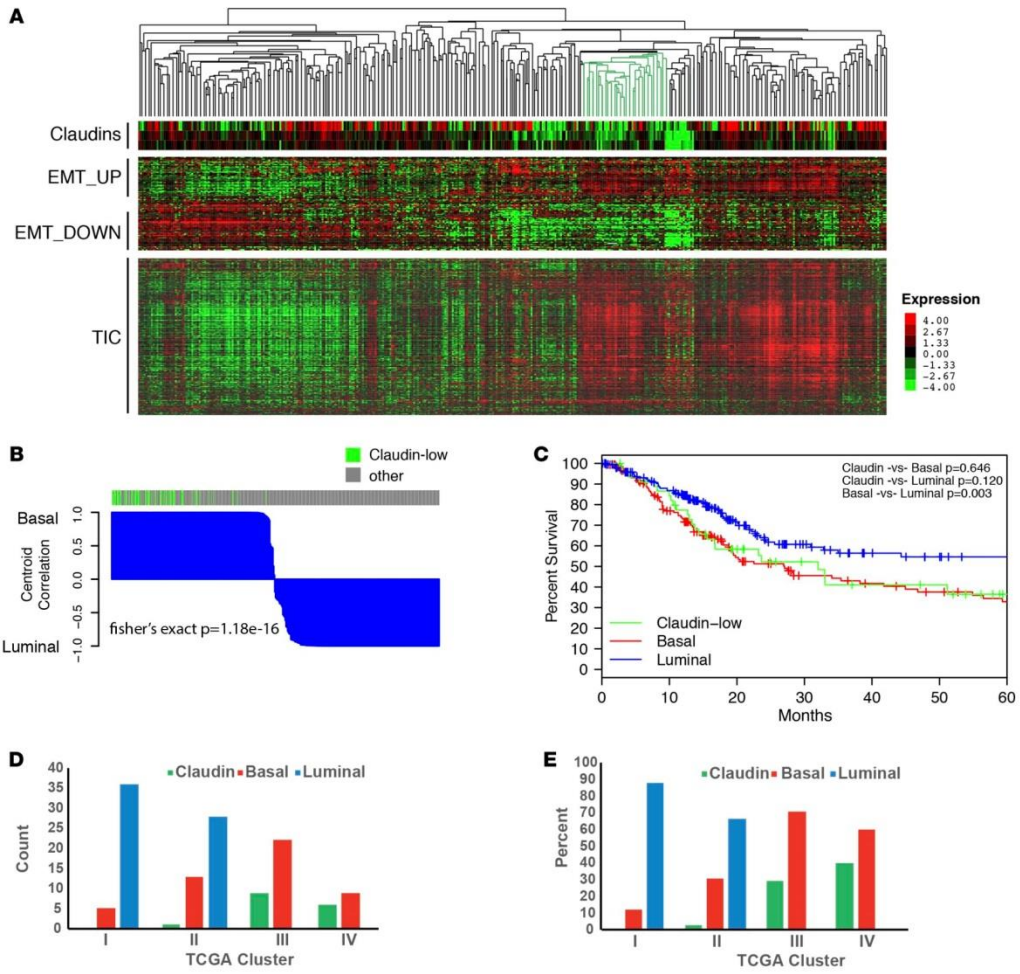

Figure 2.1: Identification of a claudin-low subtype in bladder cancer. (A) Unsupervised clustering of TCGA muscle-invasive UC samples. Samples were clustered on the basis of expression of tight-junction claudins, a bidirectional EMT signature, and a TIC signature. The tumors identified as claudin-low are highlighted in green on the dendogram. *n* = 408. (B) Waterfall plot showing correlation with the basal and luminal centroids as defined by BASE47 classification; claudin-low tumors are highlighted in green. Claudin-low tumors were significantly enriched in the BASE47 basal subtype (Fisher's exact test $P = 1.18 \times 10^{-16}$) and were highly correlated with the basal centroid (Pearson's correlation $P = 9.33 \times 10^{-15}$). *n* = 408. (C) Kaplan-Meier plot showing overall survival of bladder cancer by molecular subtype. Significance was determined by log-rank testing with a Bonferroni correction. *n* = 408. (D and E) Bar graphs showing the classification of TCGA UC tumors by TCGA mRNA cluster subtype (*x* axis) and our subtype classifications (*y* axis) by count and percentage. *n* = 129. EMT, epithelial-to-mesenchymal transition; TCGA, The Cancer Genome Atlas; TIC, tumor-initiating cell; UC, urothelial carcinoma.

2.2.2 A 40-gene classifier, bladder claudin-low 40, accurately predicts claudin-low tumors

To define a minimal set of genes that could accurately classify claudin-low bladder tumors, we applied prediction analysis of microarrays (PAMs) to the TCGA BLCA tumors and derived a 40-gene signature, bladder claudin-low 40 (BCL40), which accurately classifies bladder tumors into claudin-low and non–claudin-low subtypes, with a training error rate of 0.23 and 0.13, respectively. When combined with the previously validated bladder cancer analysis of subtypes by gene expression (BASE47) predictor (6), this provides a 3-class predictor that can accurately classify bladder tumors as claudin-low, basal, or luminal.

In order to validate the predictor, we compiled a 130-tumor metadata set from 2 previously compiled published data sets (GEO GSE48277) (5). The BASE47 and BCL40 predictors identified 36 claudin-low tumors (~30%), 27 basal tumors (~20%), and 67 luminal tumors (~50%). We found that these subtypes were phenotypically similar to the initially derived subtypes in our discovery set of TCGA bladder tumors as measured by expression of the EMT, TIC, and claudin gene signatures. Furthermore, we ran a transcriptome-wide correlation analysis between the basal, luminal, and claudin-low tumors identified in the discovery (TCGA BLCA) and validation data sets (GEO GSE48277) and found a strong correlation in gene expression between the subtypes identified in the discovery and validation data sets (basal [Pearson's $R = 0.459$, $P < 2.2 \times 10–16$], claudin-low [Pearson's $R = 0.805$, $P < 2.2 \times 10–16$], and luminal [Pearson's $R = 0.809$, $P < 2.2 \times 10–16$]). This further confirmed that the subtypes identified across separate data sets had consistent genome-wide RNA expression profiles.

We next examined whether our claudin-low subtype merely recapitulated any of the existing molecular subtypes of UC published by MD Anderson or TCGA. We compared our claudin-low, basal, and luminal predictions on the 129 published TCGA BLCA tumors with TCGA 4-subtype classification (clusters I, II, III, and IV) (8). Our claudin-low tumors were primarily found in TCGA clusters III and IV (Figure 2.1, D and E). A comparison of our claudin-low, basal, and luminal predictions on the 408 provisional TCGA BLCA tumors with the MD Anderson oneNN classification system (p53-like, basal, and luminal) (5) re-demonstrated the high concordance of luminal subtype designations (33) as well as the notion that claudin-low tumors arise primarily from basal tumors. These comparisons further strengthen the notion that claudin-low tumors do not merely recapitulate a previously described molecular subtype of bladder cancer.

2.2.3 The claudin-low subtype displays unique, intrinsic genomic alterations and gene expression patterns

We next examined the association between molecular subtype and genomic events within significantly mutated or copy number–altered genes identified as being altered at a greater than 5% frequency within TCGA BLCA data set (8). A comparison of claudin low and basal subtypes revealed that claudin-low tumors had significantly increased rates of *RB1*, *EP300*, and *NCOR1* mutations, an increased percentage of tumors with *EGFR* amplification, as well as decreased rates of mutations in *FGFR3* and *ELF3* (Figure 2.2, A and B). Relative to the luminal subtype, claudin-low tumors revealed a significantly higher rate of mutation of *TP53*, *RB1*, and *EP300* and an

increased percentage of tumors with *EGFR* amplification. Conversely, luminal tumors (compared with claudin-low tumors) had a significantly higher rate of *PPARG* amplification and mutation of *KDM6A*, *ELF3*, and *FGFR3*. These results are in keeping with the notion that genomic alterations and their subsequent effects on signal transduction and transcription may be partially responsible for differences in gene expression subtypes.

To further understand the gene expression patterns that differentiate claudin-low tumors, we performed 2-class significance analysis of microarrays (SAMs), comparing each subtype against all of the other tumors (e.g., claudin-low vs. basal plus luminal). We detected a significant number of differentially expressed genes (FDR = 0.05) by this comparison as well as by a direct comparison of each subtype with another (e.g., claudin-low vs. basal) (Figure 2.3A). Ingenuity Pathway Analysis (IPA) revealed that, compared with both basal and luminal tumors, claudin-low tumors had significant enrichment in the upstream regulators *IFNG*, *TNF*, and *TGFB1*, which are well-known proinflammatory cytokines (IFN-γ and TNF-α) and pro-EMT (TGF-β) growth factors. Additionally, claudin-low tumors had higher levels of *IL4* and *IL13* signaling relative to signaling levels in basal and luminal tumors, respectively. Further IPA analysis demonstrated enrichment of other immune-associated pathways in claudin-low tumors. These observations are in keeping with the EMT phenotype, which is a defining characteristic of claudin low tumors, but also strongly suggest that these tumors are heavily immune infiltrated.

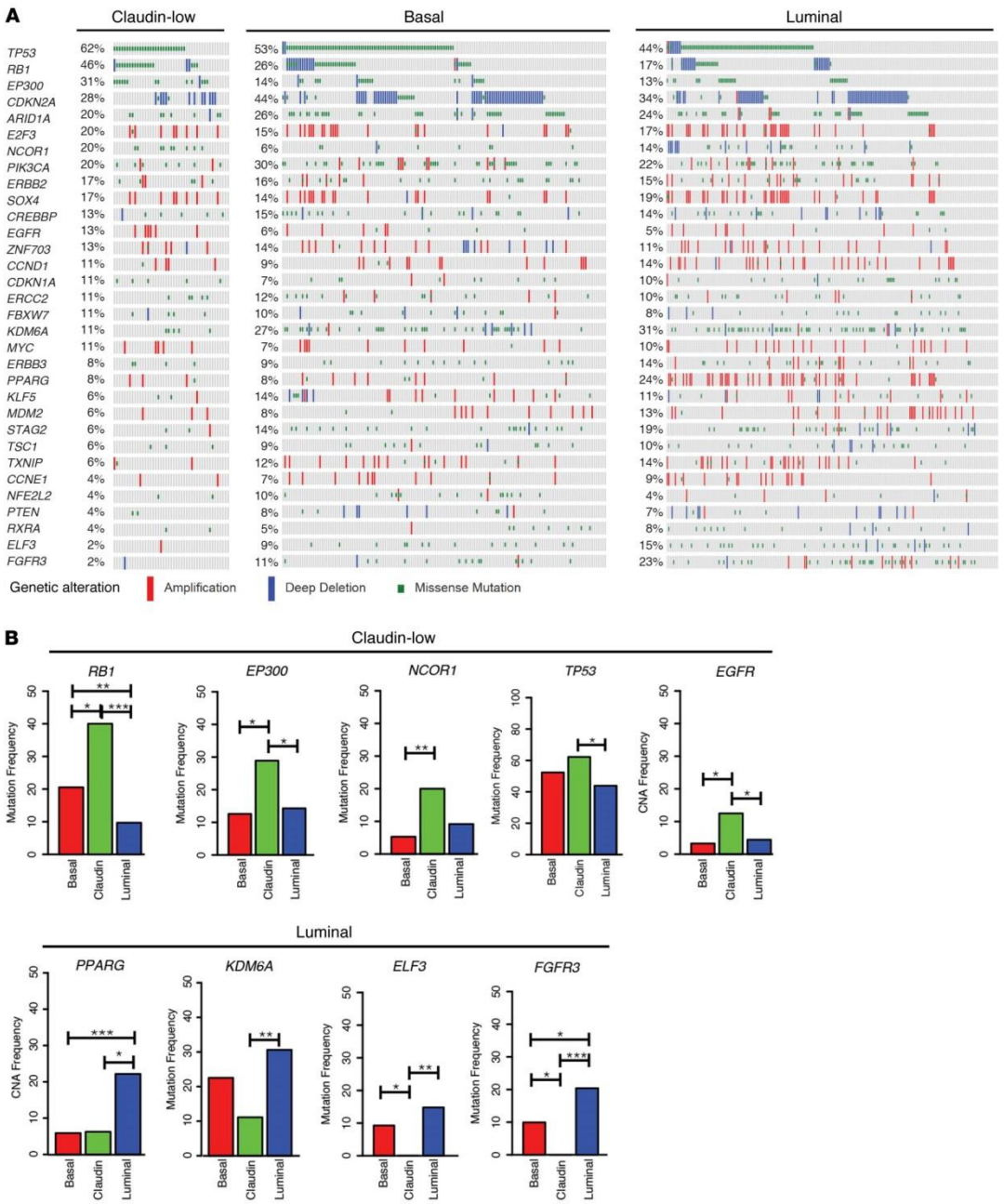

Figure 2.2: Genomic characterization of bladder cancer subtypes. (A) Oncoprint of genomic copy number alterations and mutations by bladder cancer subtype for genes previously identified as significantly mutated or copy number altered in more than 5% of bladder tumors. n = 408. (B) Bar plots of genes that were identified to have a significant ($P < 0.05$) difference in either gene mutation or copy number alteration (CNA) between the claudin-low and basal and/or luminal subtypes. *$P < 0.05$, **$P < 0.01$, and ***$P < 0.001$, by Fisher's exact test.

2.2.4 Claudin-low tumors are enriched in immune gene signature expression.

To better characterize the immune cell populations present within claudin-low tumors, we used previously defined gene signatures indicative of specific cellular immune populations (34) and examined their expression by molecular subtype. All examined signatures appeared to be and were statistically enriched in the claudin-low subtype when each signature was collapsed into a single z-score value per tumor (Figure 2.3B). To assess the level of immunosuppression, we examined the expression of a panel of immune checkpoint molecules (immunosuppression score) derived from the literature and found that they were uniformly highly expressed in claudin-low tumors compared with expression levels in both basal and luminal tumors, respectively (Figure 2.3C and D).

Bladder cancer as a whole expressed moderate levels of *PD-L1* and our immunosuppression score relative to the spectrum of 12 tumors in TCGA Pan-Cancer analysis. When broken down by subtype, however, claudin-low tumors in particular had very high levels of *PD-L1* expression (Figure 2.3E) and high expression of the immunosuppression score (Figure 2.3F). In aggregate, these findings indicate that claudin-low tumors consistently harbor a high level of immune infiltration that is matched by a high level of active immune suppression. Basal tumors, in contrast, have a more heterogeneous phenotype, while luminal tumors appear to have a paucity of immune cells or immune checkpoint expression. In keeping with this notion, there was a strong correlation between the immune signatures and the immunosuppression signature across all tumors.

The presence of an immune infiltrate has been shown to be prognostic in other cancers (35). In muscle-invasive bladder cancer, specifically, the presence of CD8+ tumor-infiltrating lymphocytes (TILs) (28) and a low ratio of FOXP3 to CD4 or CD8 expression on TILs (36) have been associated with improved disease-free and overall survival rates. In keeping with the work by Sharma et al. (28), Cox proportional hazards (Cox PH) modeling for each immune gene signature across all tumors in TCGA BLCA data set showed that only the CD8_T_Cell signature was prognostic (Cox PH = 0.846, *P* = 0.047) (Figure 2.4A), further supporting the unique importance of CD8+ TILs. When Cox PH modeling was performed within each subtype, none of the signatures were prognostic within the claudin-low and luminal subtypes. However, within the basal subtype, numerous signatures were prognostic, including the Ig signature, macrophage signature, T cell signature, CD8+ T cell signature, and immunosuppression signature (Figure 2.4B). We believe these findings are consistent with immune gene signatures being consistently upregulated in the claudin-low subtype and downregulated in the luminal subtype, respectively, while the basal subtype has a more heterogeneous range of gene signature expression, allowing for a more dynamic range across which these subtypes can be prognostic. Supporting this, the basal subtype had the largest SD of immune signature expression across all signatures (basal vs. claudin: *P* = 0.007; basal vs. luminal: *P* = 0.097, Bonferroni corrected Student's t-test).

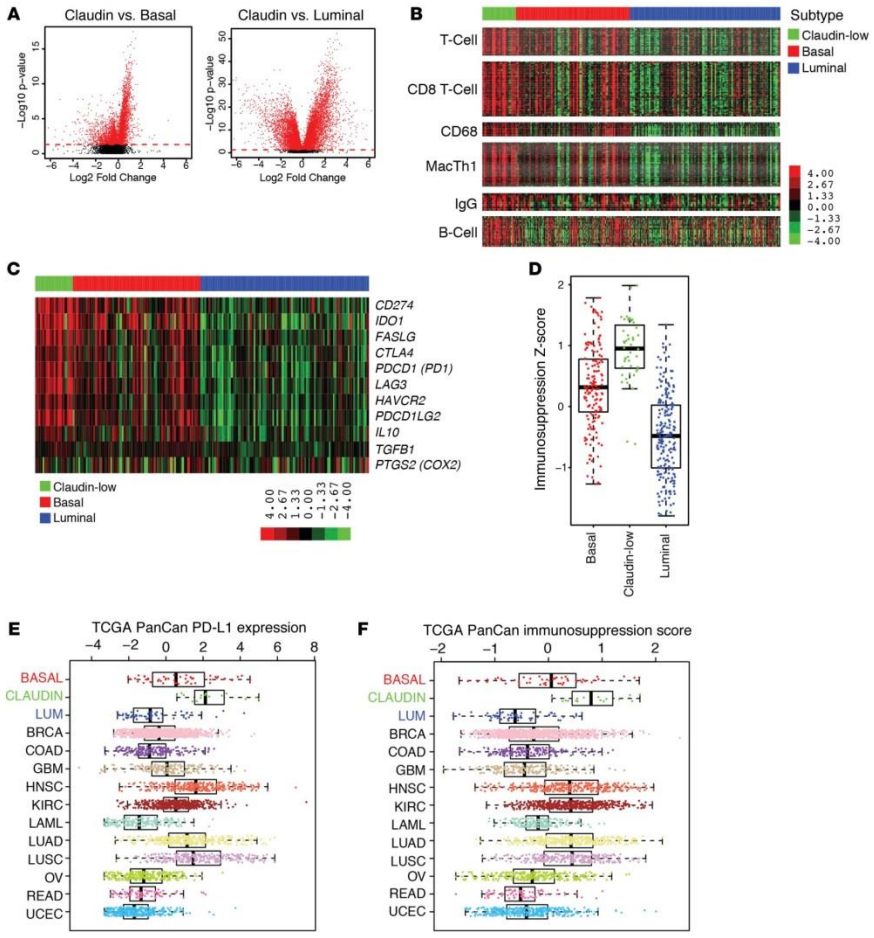

Figure 2.3: Immune characterization of bladder cancer subtypes. (A) Volcano plot of $\log_2$ fold change of median gene expression and $-\log_{10}$ *P* value of gene expression across bladder tumor subtypes. Dashed line across the plots corresponds to a significance threshold of $P = 0.05$. $n = 408$. Significance was calculated using Student's *t* test with a Bonferroni correction. (B) Heatmaps of supervised clustering of bladder tumor subtypes across previously identified immune signatures. $n = 408$. (C) Heatmap of supervised clustering of bladder tumor subtypes across an immune suppression gene signature. $n = 408$. (D) Box plot of immune suppression gene signature *z* score across bladder tumor subtypes. $n = 408$. (E) Box plot of PD-L1 gene expression across the Pan-Cancer tumor types. $n = 3{,}602$. (F) Box plot of immune suppression gene signature *z* scores across the Pan-Cancer tumor types. $n = 3{,}602$. The box plots denote the interquartile range (IQR), with the box representing Q1 to Q3, the line denoting Q2, and the whiskers extending an additional 1.5 times the IQR beyond Q1 and Q3. The dots represent data points. BLCA, bladder urothelial carcinoma; BRCA, breast cancer; COAD, colon adenocarcinoma; GBM, glioblastoma multiforme; HNSC, head and neck squamous cell carcinoma; KIRC, kidney renal clear cell carcinoma; LAML, acute myeloid leukemia; LUAD, lung adenocarcinoma; LUSC, lung squamous cell carcinoma; OV, ovarian serous cystadenocarcinoma; READ, rectum adenocarcinoma; UCEC, uterine corpus endometrial carcinoma; LUM, luminal; TCGA, The Cancer Genome Atlas; PanCan, Pan-Cancer.

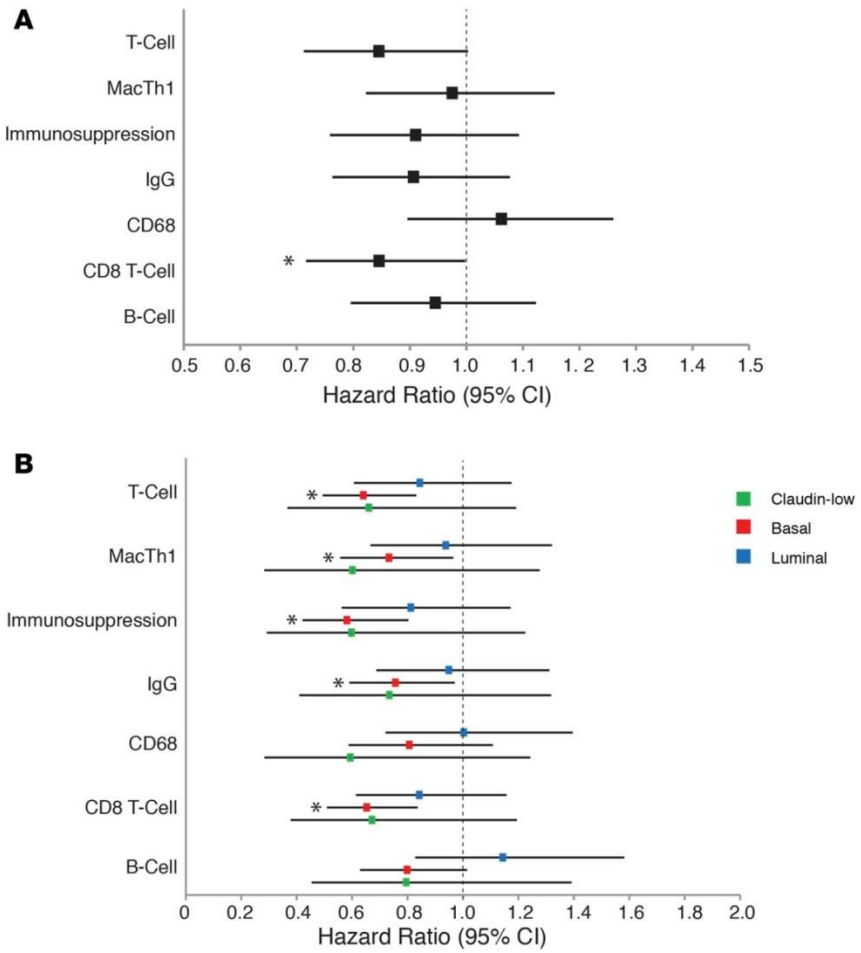

Figure 2.4: Immune gene signatures have prognostic value across bladder cancer subtypes. (A) Forest plot of Cox PH ratios of the immune gene signatures across all tumors, with a 95% CI indicated around the values. *n* = 408. (B) Forest plot of Cox PH ratios of the immune gene signatures within defined tumor subtypes, with a 95% CI indicated around the values. *n* = 408. **P* < 0.05, prognostically significant signatures by Cox PH modeling. Cox PH, Cox proportional hazard.

2.2.5 Specific T-cell receptor and B-cell receptor gene segment expression levels are prognostic in bladder cancer subtypes

An antigen-driven T cell and/or B cell response would be expected to drive clonal expansion of T cells and/or B cells, resulting in decreased diversity of T cell receptor (TCR) and/or B cell receptor (BCR) repertoires. In addition, if a clonally expanded immune response was active intra-tumorally, this should be reflected in associations of

specific TCR and/or BCR gene segment expression with improved survival. For example, decreased TCR diversity has been associated with response to immune checkpoint inhibition in melanoma (37) and has been shown to be prognostic in bladder cancer (38). To evaluate this concept in TCGA bladder samples, we fit Cox PH models to test the association of expression of each TCR or BCR gene segment with survival and calculated the number of prognostic gene segments by subtype. To establish null distributions for the number of gene segments expected in each subtype, we used the bootstrap resampling method previously published by our group (34). For both TCR gene segments (Figure 2.5A) and BCR gene segments (Figure 2.5B), a significantly higher number of gene segments than expected by chance were prognostic in the basal subtype, but not in the claudin-low or luminal subtype. Figure 2.5C and D show the specific gene segments that were prognostic in each subtype. Prognostic segments were found in multiple TCR and BCR families, with a small number of gene segments discovered in multiple subtypes (i.e.TRBV11-2). This suggests that adaptive immune responses important in endogenous antitumor immunity are not uniform in TCR and BCR usage between the subtypes.

Despite the presumed importance of assessing T cell and B cell clonality in tumor immunology, at present, this can only be done by direct TCR or BCR sequencing. Our group developed a bioinformatics method (VDJician) to accurately and efficiently reconstruct rearranged BCR V(D)J sequence repertoires from short-read RNA-sequencing data. We applied this to TCGA bladder data to evaluate whether overall BCR expression (Figure 2.5E) and/or repertoire diversity (Figure 2.5F) varied by subtype. BCR expression was higher and repertoire diversity lower (indicative of clonal

expansion) in the claudin-low subtype relative to that observed in the luminal subtype, which is consistent with the presence of a selective antigen directed response in claudin-low tumors. These results, in conjunction with our previous findings, indicate that claudin-low tumors are immune infiltrated and have an active immune response within the tumor microenvironment.

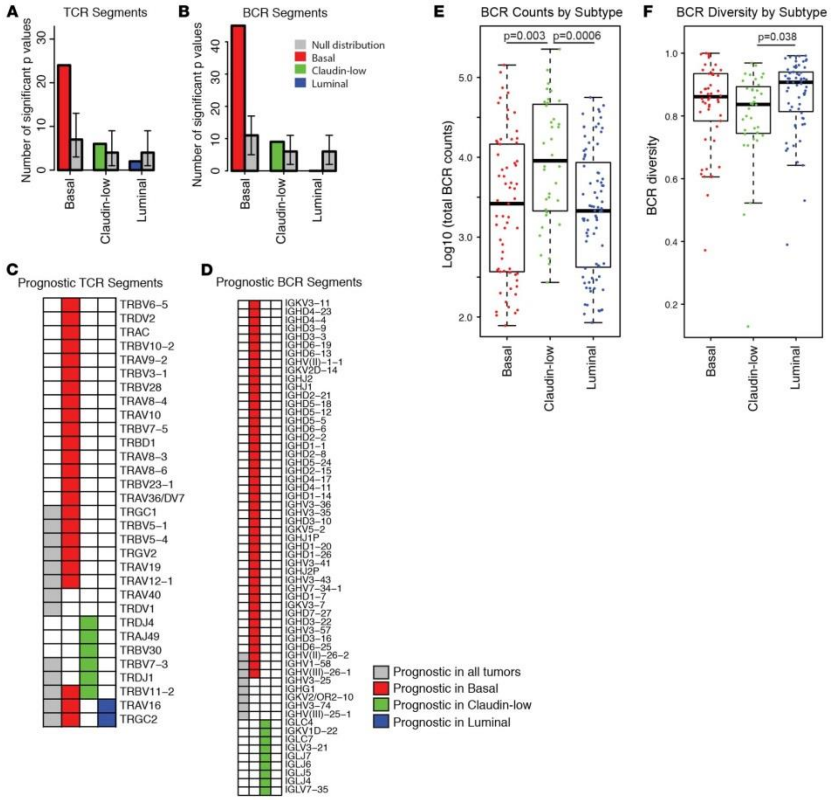

Figure 2.5: BCR and TCR segment expression is prognostic. (A) Number of TCR gene segments by subtype in which increased expression was significantly associated with improved survival by Cox PH model fit. Null distributions (gray bars) with 95% CIs were generated for each by bootstrap resampling of non-TCR genes and calculation of the number of significant *P* values that were similarly associated with prolonged survival. *n* = 292. (B) Number of BCR gene segments by subtype in which increased expression was significantly associated with improved survival by Cox PH model fit. Null distributions (gray bars) with 95% CIs were generated for each by bootstrap resampling of non-TCR genes and calculation of the number of significant *P* values that were similarly associated with prolonged survival. *n* = 292. (C) Specific TCR gene segments in which increased expression was significantly associated with improved survival by Cox PH model fit for all tumors (gray boxes), basal tumors (red boxes), claudin-low tumors (green boxes), and luminal tumors (blue boxes). (D) Specific BCR gene segments in which increased expression was significantly associated with improved

survival by Cox PH model fit for all tumors (gray boxes), basal tumors (red boxes), claudin-low tumors (green boxes), and luminal tumors (blue boxes). (E) Log base 10 number of reads supporting any BCR V(D)J rearrangement are shown by subtype. *n* = 181. Mann-Whitney *U*–Wilcoxon test with an FDR multiple testing correction was used to determine significance. (F) Repertoire diversity by subtype. The box plots in E and F denote the interquartile range (IQR), with the box representing Q1 to Q3, the line denoting Q2, and the whiskers extending an additional 1.5 times the IQR beyond Q1 and Q3. The dots represent data points. *n* = 150. Mann-Whitney *U*–Wilcoxon test with an FDR multiple testing correction was used to determine significance. BCR, B cell receptor; Cox PH, Cox proportional hazard; TCR, T cell receptor.

2.2.6 Predicted neoantigen burden does not vary significantly by bladder cancer subtype but is selectively associated with survival in basal tumors

Neoantigens are altered peptides derived from tumor-intrinsic mutant proteins that are presented by MHC molecules and can drive robust antitumor T cell responses (39). This is in contrast to self-antigens that may be overexpressed in tumors but have been subjected to central immune tolerance (40). Neoantigens derived from tumor-specific genomic aberrations can be predicted using whole-exome sequencing of paired tumor and matched normal samples, and expression is confirmed by incorporation of RNA expression data. The predicted neoantigen number has been positively associated with favorable clinical outcomes in multiple tumor types (41) as well as with response to immune checkpoint inhibition in melanoma (18,42) and non–small-cell lung cancer (20). These results suggest an important protective role for the endogenous repertoire of T cells able to target tumor cells. In order to determine whether neoantigen burden varied by bladder tumor subtype, we implemented an informatics pipeline based on the approach published by Rajasagi et al. (43) and applied this to TCGA bladder data (Figure 2.6). There was a noisy but clear correlation between predicted neoantigen burden and the number of somatic mutations (Figure 2.6A) (Spearman's $R = 0.79$, $P < 2$

× 10–16, Figure 2.6B). Interestingly, claudin-low tumors, despite having a high level of immune infiltration and active immunosuppression, did not have a significantly different level of predicted neoantigens compared with that of basal or luminal subtypes (Figure 2.6C).

To assess the association between predicted neoantigen burden and subtype, we performed Cox PH analysis with the predicted neoantigen count as the potential explanatory variable. In the basal but not claudin-low or luminal subtypes, an increased number of predicted neoantigens was associated with prolonged survival (P = 0.025). For all bladder tumors taken together, the association was significant as well (P = 0.005). Figure 2.6D shows survival curves for all bladder tumors divided by the median predicted neoantigen count into high versus low neoantigen burden. Analyzed in this way as well, high neoantigen burden was associated with prolonged overall survival. Therefore, while there is a high correlation between bladder cancer molecular subtype and immune signature expression, this does not appear to be explained by the predicted neoantigen number.

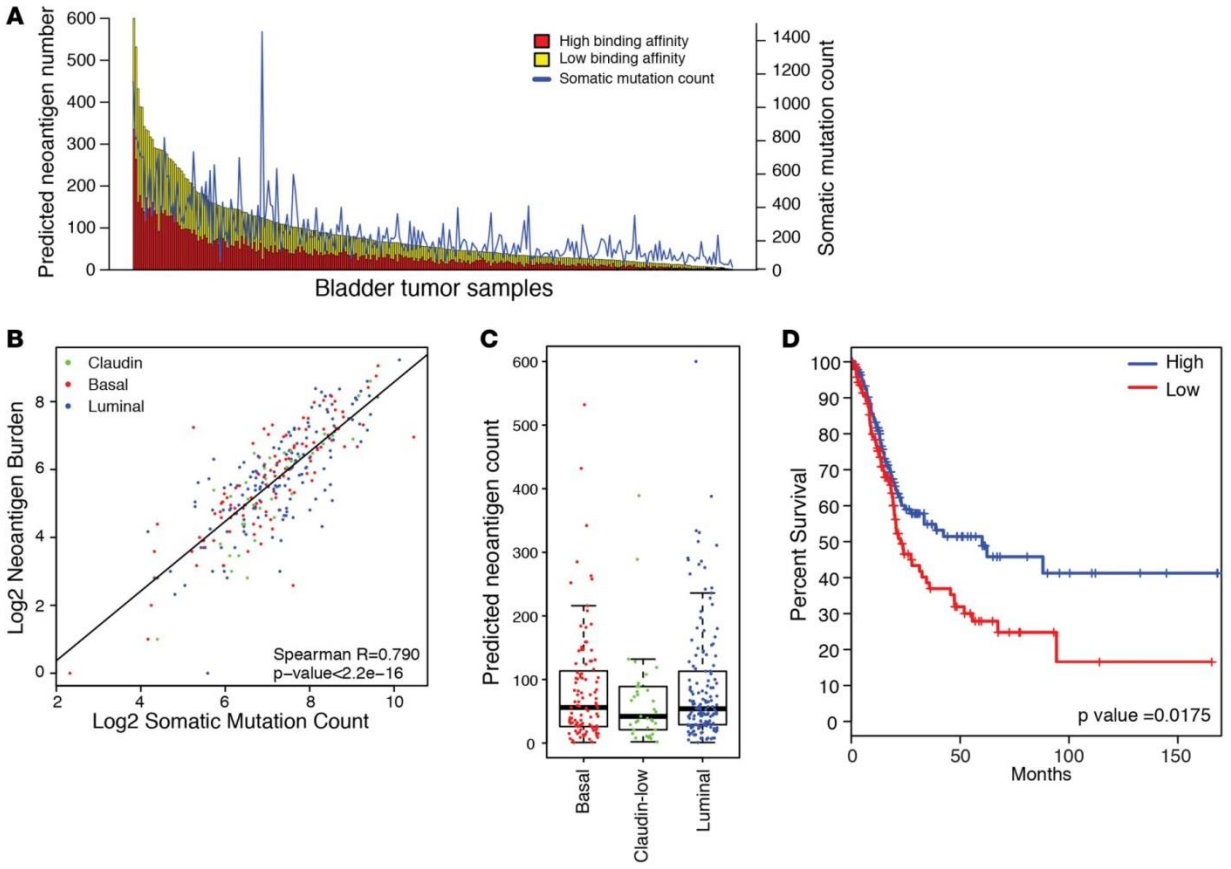

Figure 2.6: Predicted neoantigen burden by bladder cancer subtype. (A) Stacked bar plot showing the number of predicted neoantigens in each bladder tumor with a predicted IC_{50} of less than 50 nm (red bars) and less than 150 nm (yellow bars). Numbers of predicted neoantigens are shown in the left *y* axis. Blue line and right *y* axis show the number of missense mutations per tumor. *n* = 289. (B) Scatter plot of somatic missense mutations (log_2) versus predicted neoantigen burden (log_2) across TCGA data set. Significance and correlation were determined using Spearman's rank test. *n* = 289. (C) Box plot showing the number of predicted neoantigens with an IC_{50} of less than 50 nm by tumor molecular subtype. Subtypes were not significantly different ($P > 0.05$). Significance was determined by 1-way ANOVA. *n* = 289. The box plots denote the interquartile range (IQR), with the box representing Q1 to Q3, the line denoting Q2, and the whiskers extending an additional 1.5 times the IQR beyond Q1 and Q3. The dots represent data points. (D) Kaplan-Meier plot showing survival of bladder cancer patients with high (greater than median value, blue line) versus low (less than median value, red line) predicted numbers of neoantigens. Vertical hash marks indicate censored data. Significance was determined by log-rank test. *n* = 289. TCGA, The Cancer Genome Atlas.

2.2.7 Claudin-low tumors express high levels of cytokines and chemokines normally repressed by PPARG

Given that predicted neoantigen burden was relatively similar across molecular subtypes, we explored the possibility that claudin-low tumors harbor an immune infiltrate because of increased production of proinflammatory cytokines and chemokines. To this end, we examined the relative expression of a panel of cytokines and chemokines and their receptors among bladder subtypes and found that the majority of them were significantly upregulated in claudin-low tumors relative to expression levels in both basal and luminal tumors (Figure 2.7A and B). We noted that NF-κB target genes in particular were significantly upregulated in the claudin-low subtype compared with expression in both the basal and luminal subtypes (Fisher's exact *P* value = 1.885 × 10–8).

A defining transcriptional program of urothelial differentiation and of luminal bladder tumors is activation of peroxisome proliferator-activated receptor γ (*PPARG*) signaling (44). Consistent with this, we noted that *PPARG* was significantly amplified in luminal relative to claudin-low tumors (Figure 2.2B). Because *PPARG* is known to directly inhibit NF-κB signaling (45), we hypothesized that heightened *PPARG* activity might play a role in restraining the proinflammatory effects of NF-κB. Using a publicly available gene expression data set (GEO GSE48124), we noted that the expression changes induced by treatment with rosiglitazone, a PPARγ agonist, in UMUC7 and UMUC9 bladder cancer cells predicted suppression of the upstream regulator *NFKB1* as well as a number of genes known to be activated by NF-κB (*STAT5A*, *IL6*, *TNF*, *CCL5*). Furthermore, rosiglitazone-treated UMUC7 and UMUC9 cells had downregulation in gene signatures of NF-κB activation as assessed by gene set

enrichment analysis (GSEA) (Figure 2.7C). Interestingly, we saw that rosiglitazone treatment resulted in significant downregulation of immune checkpoint molecules (such as *PDL1*, *PDL2*, *IL12*, and *PGSL2*) found in our immunosuppression signature (Figure 2.7D). In aggregate, these data support the notion that downregulation of PPARγ activity results in unopposed NF-κB signaling, which contributes to the proinflammatory milieu of claudin low tumors as well as to their high level of active immune suppression.

Finally, in keeping with recent work demonstrating that EMT is associated with immune checkpoint molecule expression (46,47), we observed a strong correlation between our bladder cancer–derived EMT signatures and multiple immune signatures including our immunosuppression score: R = 0.462 [EMT (Up)] and R = –0.471 [EMT (Down)]; $P < 2.2 \times 10–16$ (both “Up” and “Down”) (Figure 2.7E). Furthermore, given the important role of PPARγ in terminal urothelial differentiation (48), we hypothesized that it may be a critical regulator of epithelial-mesenchymal balance in urothelial cancers. Indeed, we found that PPARγ activation (by rosiglitazone) in UMUC7 and UMUC9 cells decreased levels of our EMT (Up) signature (Figure 2.7F).

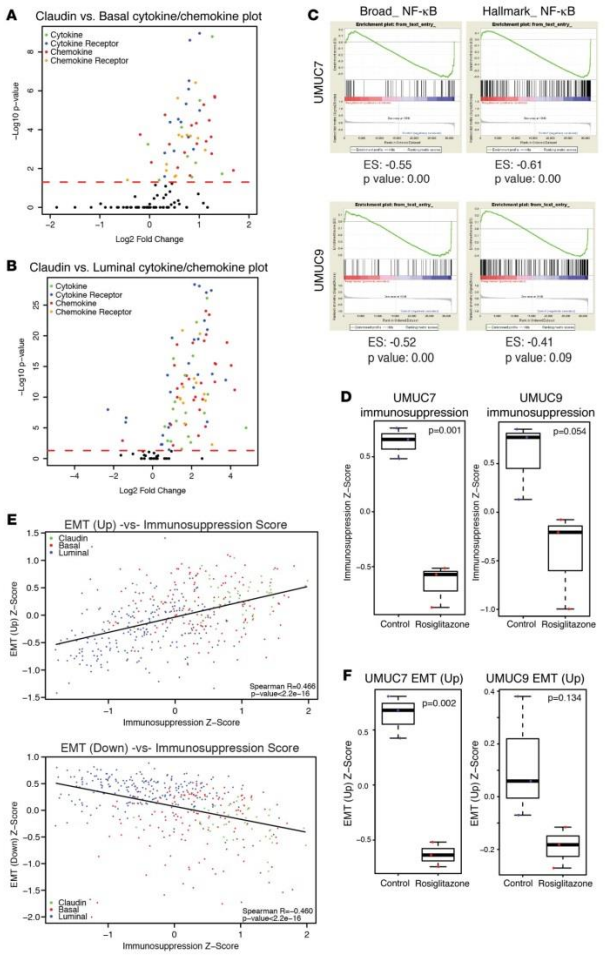

Figure 2.7: Cytokine and chemokine regulation across bladder cancer subtypes. (A-B) Volcano plots of $\log_2$ fold change of median gene expression and $-\log_{10}$ *P* value of gene expression for cytokines and chemokines across claudin-low/basal and claudin-low/luminal subtypes. Dashed lines across plots correspond to $P = 0.05$. Significance was calculated using Student's *t* test with a Bonferroni correction. $n = 408$. (C) GSEA enrichment plots indicating that NF-κB signatures were decreased in rosiglitazone-treated UMUC7 and UMUC9 bladder cancer cell lines. Significance was determined using GSEA software. (D) Box plots showing that immunosuppression gene signature expression was significantly decreased across UMUC7 and UMUC9 cell lines after rosiglitazone treatment. Significance was determined using Student's *t* test. $n = 6$. (E) Correlation plot of immunosuppression and EMT gene signature expression. $n = 408$. Significance and correlation were calculated using a Spearman's rank test. (F) Box plots showing that EMT gene signature expression was decreased across UMUC7 and UMUC9 cell lines after rosiglitazone treatment. Significance was determined using Student's *t* test. $n = 6$. The box plots in D and F denote the interquartile range (IQR), with the box representing Q1 to Q3, the line denoting Q2, and the whiskers extending an additional 1.5 times the IQR beyond Q1 and Q3. The dots represent data points. ES, enrichment score; EMT, epithelial-to-mesenchymal transition; GSEA, gene set enrichment analysis.

2.3 Discussion

Herein, we characterize the claudin-low, molecular subtype of high-grade UC. Claudin low bladder tumors are defined by high levels of EMT, enrichment for TIC signatures, and low expression levels of tight-junction claudins. In addition, claudin-low tumors are enriched in specific genomic alterations (e.g., mutations in *EP300* and *NCOR1* as well as amplification in *EGFR*) and have a distinct transcriptional profile. Furthermore, we found that claudin-low tumors are highly enriched in all immune gene signatures examined, but also express high levels of immune checkpoint molecules. In contrast to melanoma and non–small-cell lung cancer, the predicted neoantigen burden did not appear to correlate with immune infiltration in bladder cancer. Instead, claudin-low tumors appeared to downregulate PPARγ signaling, resulting in unopposed NF-κB activity and contributing to a proinflammatory milieu.

In our study, as in previous studies, expression of the various immune gene signatures was highly correlated, including high correlations between gene signatures associated with specific cellular subpopulations (CD8+ T cells, B cell lineage, Th1-polarizing macrophages) and the immunosuppression gene signature. This supports the claim that tumors growing in the presence of immune cell influx must adaptively suppress the antitumor response in order to survive. Immune gene signature expression levels, the prognostic value of immune gene signatures, and TCR and BCR gene segment expression divide the bladder cancer subtypes into 3 groups: (a) low infiltrate with nonsignificant prognostic value (luminal); (b) heterogeneous infiltrate with significant prognostic value (basal); and (c) high infiltrate with nonsignificant prognostic value (claudin-low). We hypothesize that the lack of prognostic benefit in claudin-low

and luminal tumors is driven by different mechanisms. Luminal tumors were sparsely infiltrated and showed low expression levels of molecules associated with immunosuppression. In contrast, claudin-low tumors showed a substantial but ineffective infiltrate in the context of high expression levels of immunosuppression markers. Immune features may fail to be prognostic in luminal tumors because no infiltrate is present, whereas they fail in claudin-low tumors because, despite a dense infiltrate, the level of immunosuppression overwhelms active antitumor immunity. Basal tumors have the highest degree of variability in immune gene signature expression, and in this model, some basal tumors will have generated an immune response that is competing more effectively (though ultimately insufficiently to clear tumor) with tumor driven immune suppression. While additional studies are required to test this hypothesis, our data suggest that claudin-low tumors as a whole, as well as a subset of basal tumors, are poised for response to immune checkpoint blockade.

The different molecular aberrations that characterize the bladder cancer subtypes may yield differential exposure of antigens to the immune system, resulting in skewing of the tumor-infiltrating TCR and/or BCR repertoires in predictable ways should the antigens be public (i.e., shared between multiple patients). Though our study was not designed to formally test this, we report here a high degree of variability, in which adaptive immune gene segments were prognostic among the bladder cancer subtypes, an effect that would be expected if TCR/BCR repertoire features associated with tumor targeting were to vary by tumor subtype. Interestingly, in the basal subtype, multiple TCR gene segments associated with γδ T cells were found to be significantly prognostic ($P < 0.05$ by Cox PH). As this specific subset of T cells is involved in adaptive immunity

at mucosal surfaces and able to respond to mycobacteria, γδ T cells may be involved in antitumor immunity and an attractive target for the development of biomarkers of response to bladder cancer immunotherapy, including Bacille Calmette-Guérin (BCG), which is commonly given for non-muscle invasive disease.

We report here the VDJician algorithm that performs de novo assembly of repertoires of fully rearranged BCR VDJ sequences. When analyzed, the claudin-low subtype showed the highest expression levels but the lowest repertoire diversity compared with basal and luminal subtypes. This is consistent with the presence of an antigen-driven response in the claudin-low tumors, leading to clonal expansion of antigen-reactive B cell–lineage cells. Plasma cells are known to express high levels of BCR mRNA, and these results would also be consistent with a restricted plasma cell infiltrate. In addition, as plasma cells represent a terminal differentiation in the B cell lineage in response to antigenic stimulation, their presence would also be expected in an antigen-driven response. Future experiments will be necessary to confirm these findings and attempt to map immunogenic epitopes in claudin-low tumors.

In melanoma and a subset of solid tumors, neoantigen burden correlates with expression of perforin and granzyme A (a measure of cytolytic activity) (42,49) and tumors with these attributes appear to be more responsive to CTLA4 checkpoint blockade. In bladder cancers examined in that study, there was a trend toward increased cytolytic activity, with increased predicted neoantigen burden (49). In contrast, we did not see significant correlations between neoantigen burden and predicted features such as T cell or CD8+ T cell gene signatures, immunosuppression score, or molecular subtype, suggesting that alternate etiologies exist to explain the

proinflammatory state of claudin-low and basal tumors relative to that of luminal tumors. In this regard, we observed significant upregulation of cytokines and chemokines in claudin-low tumors and hypothesize that this cytokine milieu is favorable to a proinflammatory state and immune cell influx. We propose that PPARγ activity, through its ability to repress NF-κB, is inversely correlated with this proinflammatory milieu and, therefore, that luminal tumors, which are enriched in *PPARG* amplification and activation of *PPARG* gene signatures, have very little inflammation. Conversely, we found that claudin-low tumors, which have relatively low levels of *PPARG* pathway activation, have high levels of immune infiltration. Therefore, in contrast to the inflamed tumors found in melanoma and non–small-cell lung cancer, which appear driven by neoantigen expression, inflamed bladder cancers have a proinflammatory state induced by an enhanced cytokine/chemokine milieu. Further work has shown that PPARγ signaling impairs T-cell infiltration and confers a partial resistance to immunotherapies (50).

Finally, while immune checkpoint inhibition holds great promise, the response rates of various solid tumors remain approximately 20% to 30%, suggesting that many patients will not derive benefit. Our BASE47 and BCL40 gene classifiers, which can accurately subtype high-grade bladder tumors, may serve to identify useful predictive biomarkers of response (i.e., claudin-low) or lack of response (i.e., luminal) to PD1 axis inhibition. Moreover, our studies further validate the notion of subtype-specific therapy in bladder cancer (i.e., basal = chemotherapy; claudin-low = immune checkpoint blockade) and advance the possibility that claudin-low breast tumors may have similar immune features.

2.4 Methods

2.4.1 TCGA data set manipulation

TCGA Bladder Urothelial Carcinoma RNA Expression data set was downloaded from the Broad Institute Firehose Pipeline (http://gdac.broadinstitute.org) on August, 27, 2015. RNA expression was downloaded in a normalized RSEM file. Expression values were log2 transformed, and genes with less than 80% expression across all samples were filtered out. Missing values were imputed using the *K*-nearest neighbor imputation method. Tumor-adjacent normal samples were removed, and gene expression values were median centered across each gene. TCGA Pan-Cancer data set was downloaded from the Synapse website (https://www.synapse.org) from data set syn2468297 (51). Genes with less than 80% expression across all samples were filtered out. Missing values were imputed using *K*-nearest neighbor imputation.

2.4.2 Gene signatures

Bladder TIC, EMT, and tight-junction claudin gene signatures were used in the classification of a claudin-low subtype. The TIC signature was derived by Chan et al. (32). The set of claudins used was identified by Prat et al. (31). The EMT signature is a bidirectional signature derived on the GEO GSE60564 data set of Notch2 overexpression in a urinary bladder RT4V6 cell line. The data set was mean collapsed onto genes. Genes were filtered for a significant difference (Student's *t* test, $P < 0.05$) between the control and Notch2-overexpressed (EMT-induced) cell lines and also for their presence in TCGA bladder UC data set. Genes were then ranked on the basis of median difference between the 2 groups. The top 50 genes with the most increased

expression in the EMT-induced cells and the top 50 genes with the most decreased expression in the EMT-induced cells were used to create the bladder cancer– specific EMT_UP and EMT_DOWN signatures, respectively. Immune gene signatures used to describe immune cell processes were derived by Iglesia et al. (34). Z scores were calculated for each claudin, basal, and luminal subtype and box plots made of the distributions. Gene signature *z* scores were obtained by calculating the *z* score of each gene within a signature across all samples and taking the median of all gene *z* scores within a gene signature as the *z* score of the gene signature.

2.4.3 Identification of a claudin-low class

Bladder basal and luminal predictions and centroid distances were made using the BASE47 PAM Classifier derived by Damrauer et al. (6). Breast cancer claudin predictions were made using the Distance-Weighted Discrimination (DWD) Claudin Classifier provided by Prat et al (31). Data were clustered on the TIC/EMT (Up and Down)/claudin gene sets using average linkage clustering with a centered correlation similarity metric on the Cluster 3.0 platform. Each gene set was individually clustered across genes using average linkage clustering. Gene sets were collapsed down to *z* scores, and a conservative node with high TIC/high EMT UP/low EMT DOWN/low claudin gene set was selected. SigClust was run on the node, expanding out to the entire gene set for each increasing node. Differences in gene expression subtypes were determined using SAMs run on R, with an FDR of 0.05. A PAM predictor (BCL40) was derived on the 408 tumor TCGA data set for a claudin/other subtype classifier. A threshold of 6.4 was selected, giving a 40-gene predictor with an overall error rate of

0.14. A validation data set of 130 muscle-invasive UC samples was compiled from 73 sample and 57-sample data sets from GEO (GEO GSE48277] (5). Each data set was mean collapsed onto genes. The data set was combined and batch effect adjusted using parametric empirical Bayesian adjustments through the ComBat function in the sva R package and was then median centered. Genome-wide correlations and significance were calculated using a Pearson's correlation test.

2.4.4 Clinical, mutation, and copy number alteration analysis

Mutation, copy number, and clinical data were downloaded as mutation packager calls through the Broad Institute Firehose Pipeline (http://gdac.broadinstitute.org) on September 3, 2015. Survival status and overall survival were determined on the basis of the data provided. Oncoprint figures were produced using the downloaded TCGA mutation and copy number alteration (CNA) data. Genes were selected on the basis of previously being identified as having significant mutations or CNAs within the gene (8). Significance in CNA and mutation across subtypes was determined using Fisher's exact test. Cox PH ratios and CIs were derived using the survival package on the R platform.

2.4.5 Pathway and gene signature expression analysis

Cellular pathway analysis across subtypes was performed using QIAGEN's IPA (www.qiagen.com/ingenuity). Comparison across subtypes was done using the gene list with an FDR of 0.00 as determined by SAM analysis across subtypes. Supervised clustering of samples was performed across all tumor samples by claudin, basal, and luminal subtypes. Genes within each signature were clustered using average linkage on

Cluster 3.0. Significance across gene signature *z* scores was calculated using Student's *t* test. Cytokines and chemokines were identified using a RegEx search to capture all members of the molecular families. Volcano plots were produced using Bonferroni-adjusted Student's *t* test *P* values, and fold change was calculated using normalized RSEM expression values. NF-κB gene signatures were accessed through Molecular Signatures Database (MSigDB) or compiled by the Broad Institute. GSEA software was used to produce enrichment plots (http://www.broad.mit.edu/gsea/) (52). UMUC7 and UMUC9 cell line data were accessed through GEO data sets GSE48124 and GSE47993, respectively. Expression values were mean collapsed onto genes. Gene signatures were compiled on the basis of existing gene lists. Significance was calculated by collapsing gene signatures into *z* scores as described above, and 2-tailed Student's *t* tests were performed across gene signatures.

2.4.6 TCR and BCR gene segment expression analysis

Expression levels of 353 BCR gene segments and 240 TCR gene segments were determined for TCGA bladder tumor samples with available TCGA mRNA sequencing data and survival data using bedtools (version 2.17.0). Gene expression values were normalized to the upper quartile of total reads within a sample as previously described (53). Survival analyses were performed using a Cox PH model to derive *P* values and coefficients for each gene segment using the Cox PH function in the survival package in R. The number of gene segments that were significantly associated with improved survival ($P < 0.05$ and coefficient <0) was calculated for each bladder tumor subtype. Null distributions describing the expected number of prognostic

gene segments for each subtype were estimated with 95% CIs according to the bootstrap method previously published by our group (34). Fisher's exact test was used to compare the number of BCR segments and TCR segments significantly associated with improved survival among all subtypes.

2.4.7 Analysis of rearranged BCR repertoires using VDJician

The VDJician software accepts mRNA-sequencing data mapped to the genome as input and builds a deBruijn graph of read pairs that map to IgH loci or have similarity with germline IgH alleles as well as all unmapped reads. The graph is traversed exhaustively, resulting in a set of putative contigs. Anchor sequences near the 3′ end of V segments and the 5′ end of J segments are identified in an up-front indexing step. If a contig contains a sequence within a configurable distance of a V anchor and a J anchor, the anchors are a reasonable distance apart, and conserved amino acids that typically bind a CDR3 segment are present (cysteine and tryptophan for IgH), the contig is considered a candidate. The original set of reads is mapped to candidate contigs, which are then further filtered on the basis of coverage and read pair information. VDJician outputs a final set of contigs along with alignments of the original reads mapped to these contigs. This output was passed to RSEM for transcript quantification. The total BCR count was calculated by summing the read count values for all predicted BCR sequences for each sample. Evenness was calculated by dividing the Shannon-Wiener diversity index by the number of BCR sequences for each sample (example expression in R): -sum((read count/sum(read count))*log(read count/sum(read count))))/log(number of BCR sequences). *P* values were determined using a Mann-Whitney *U*–Wilcoxon test.

2.4.8 Neoantigen prediction

The bladder cancer data set used for neoantigen prediction consisted of 289 samples with available TCGA mRNA-sequencing data, exome-sequencing data, and tumor specific mutation annotation data (8). Neoantigens were predicted using a bioinformatics pipeline similar to that developed by Rajasagi et al (43). Tumor-specific single nucleotide variant annotation data were downloaded from the Broad Institute Firehose Pipeline (http://gdac.broadinstitute.org). Pysam was used to determine RNA sequencing read coverage of missense mutations, and bedtools (version 2.17.0) was used to determine the exome-sequencing read coverage of missense mutations. Nine- and ten-mer peptides derived from 3 ORFs with all possible combinations of missense mutations that overlap the genomic location of peptide in the ENCODE reference transcript set were considered in the peptide generation pipeline. DNA sequences corresponding to peptides were retrieved and translated in silico into protein sequences. The expression levels of each peptide generated were determined by the lowest missense mutation RNA-sequencing read coverage. PHLAT was used to identify the HLA class I (HLA-A, HLA-B, HLA-C) type of each tumor sample (54). Binding affinity to MHC molecules expressed by the tumor for all possible 9- and 10-mer peptides generated from missense mutations was predicted using NetMHCpan (version 2.8). Binding affinity of peptides to null alleles, alternatively expressed alleles, and alleles not supported by NetMHCpan were not predicted. Peptides were then filtered by their binding affinities (IC50 nM) to each class I allele in the tumor sample's HLA type and RNA expression level of the predicted source transcript(s). Peptides with an IC50 value

of less than 150 nM for at least 1 class I allele and RNA read support of at least 2 reads were considered predicted neoantigens.

CHAPTER 3: Targeted immune checkpoint inhibition therapy in a rare form of bladder cancer

3.1 Introduction

In the United States, bladder carcinoma is the 4th most common malignancy in men and the 9th most common in women (67). Overall, an estimated 17,000 people will die of bladder cancer in 2018. Bladder cancer takes on a spectrum of histomorphologic appearances. The predominant histologic subtype is urothelial carcinoma (90% to 95%) and, less frequently, adenocarcinoma (2%) or squamous cell carcinoma (2.5%). Urachal carcinomas are a subtype of bladder adenocarcinoma that arises from the urachus, an embryologic remnant that connects the bladder and the allantois during fetal development (55). Postnatally, it fuses to become a fibrous cord known as the median umbilical ligament. Urachal tumors comprise approximately one third of all bladder adenocarcinomas and usually develop in the 5th to 6th decade of life, with a male predominance (56,57). Because of their frequent presentation at the dome of the bladder, urachal adenocarcinomas are clinically and pathologically grouped with bladder neoplasms and are typically seen by urologic oncologists and genitourinary pathologists. Evidence-based treatment of this disease is hindered by its rarity; thus, current treatment paradigms for urachal adenocarcinoma are primarily anecdotal in nature.

As a result of the complex embryology of the allantois and cloaca, the cellular origin and molecular pathogenesis that drive the development of urachal

adenocarcinoma are speculative (55). Intestinal metaplasia or enteric rests are hypothesized as the histogenetic precursor of these tumors. Although the genetics of urachal adenocarcinoma have been investigated by multiple groups, no reports on the global gene expression patterns of urachal adenocarcinoma have been published. One study selectively examined the prevalence of *KRAS* and *BRAF* mutations in high-stage urachal adenocarcinomas and, although they found no *BRAF* mutations, 42% harbored *KRAS* mutations (58). The study also noted a high rate of loss of protein expression for a number of genes that are correlated with microsatellite instability. A more recent study found a high rate of NF1 mutations via whole-exome sequencing of seven urachal adenocarcinomas (59). Finally, another recent study showed that urachal adenocarcinomas harbor mutations in mitogen-activated protein kinase (MAPK) pathways, similar to colorectal adenocarcinoma, and showed the potential for treatment with the anti–epidermal growth factor receptor antibody cetuximab (60).

Herein, we report, to our knowledge, the first transcriptome analysis of urachal adenocarcinoma using whole-transcriptome profiling by RNA sequencing. A pan-cancer transcriptomic analysis of urachal tumors comparing them with 12 cancers of different tissue origins suggest that their RNA expression patterns most closely resemble colorectal adenocarcinoma and glioblastoma (GBM). Our work also validates reports that urachal adenocarcinomas harbor alterations that are typically found in colorectal carcinoma—that is, *APC*, *SMAD4*, and *KRAS* mutation—but extends those observations to show that a subset of urachal cancers has inactivation of genes that are involved in microsatellite instability (*MSH2*, *MSH6*) or hypermutation (*POLE*), and that all urachal tumors invariably have mutations of *TP53* (100%). One patient with an *MSH6*

mutation was treated with the anti–programmed death-ligand 1 (PD-L1) antibody atezolizumab, which resulted in stable disease. In aggregate, our studies demonstrate that urachal tumors harbor a high molecular resemblance to colorectal adenocarcinoma and suggest a novel therapeutic option: immune checkpoint blockade.

Procedure	Tumor Location	Subtype	TNM Stage
Partial cystectomy	Dome	Mixed type (enteric signet ring)	T2b, N0, MX
Cystectomy	Posterior wall/dome	Mucinous (colloid)	T4, N1, MX
TURBT	Not Specified	Mucinous (colloid)	T2b, NX, MX
Cystectomy	Not Specified	Mucinous (colloid)	T4, N0, MX
Partial cystectomy	Not specified	Mucinous (colloid)	T2b, NX, MX
Partial cystectomy	Posterior wall	Mucinous (colloid)	T3a, NX, MX
Partial cystectomy	Urachus	Mucinous (colloid)	T3a, NX, MX
TURBT	Vesicourachal junction	Mucinous (colloid)	T1, NX, MX
Partial cystectomy	Dome/urachal remnant	Enteric	T3, N0, MX
Cystectomy	Posterior, base, right, and left bladder walls	Mixed type (mucinous/signet ring)	T4a, N2, MX
Cystectomy	Dome	Enteric	T3b, N0, MX
Partial cystectomy	Dome	Mucinous (colloid)	T3, N0, MX
Cystectomy	Posterior wall	Mucinous (colloid)	T4b, N2, MX
Partial cystectomy	Dome	Mucinous (colloid)	T2a, N0, MX

Table 3.1: Clinical Characteristics of Urachal Tumors used in this study

3.2 Results

3.2.1 Urachal adenocarcinomas molecularly resemble colorectal adenocarcinoma and glioblastoma in a pan-cancer analysis

Thirteen urachal adenocarcinomas were identified from a search of the University of North Carolina surgical pathology database (Table 3.1). All were confirmed to be urachal adenocarcinomas on the basis of standard criteria (Methods). We first performed global transcriptome profiling of 13 urachal adenocarcinomas using RNA sequencing. Transcript abundance was estimated by RNA-seq by expected

maximization on the basis of University of California, Santa Cruz, known genes annotation (GAF2.1) (74). To assess the similarity of urachal adenocarcinomas to other cancers, after normalization and correction for batch effect by using surrogate variable analysis, we performed hierarchical clustering using the top 10% of differentially expressed genes within the previously described TCGA Pan-Cancer data set, which includes tumors from 12 different tissues of origin (51). Five of 13 urachal tumors clustered with the TCGA colon and rectal (COADREAD) cancers, while four clustered most closely with the TCGA GBM tumors, which suggests that urachal tumors have global gene expression patterns that significantly resemble these two tumor types (Figure 3.1A). Next, we more quantitatively assessed the level of similarity between each urachal tumor and the TCGA Pan-Cancer tumor types across all genes. To this end, using all expressed genes, we derived centroid values for each gene within a TCGA Pan-Cancer tumor type and determined the correlation between each TCGA Pan-Cancer tumor type and each individual urachal sample (Figure 3.1B). Similar to hierarchical clustering results (Figure 3.1A), we observed that a subset of urachal tumors had high similarity (R = 0.45 to 0.65) to the TCGA COADREAD tumors, whereas others had more moderate similarity to the TCGA GBM samples (R = 0.15 to 0.35). In aggregate, these results support the notion that subsets of urachal tumors are molecularly similar to either colorectal cancer or GBM.

Urachal adenocarcinomas arise from an embryologic remnant of the allantois that is formed when the cloaca divides into an anterior and posterior portion. Whereas the anterior portion becomes the urogenital sinus, the posterior portion goes on to form the rectum (56). Of note, urachal remnants are lined by urothelium with varying

numbers of columnar and/or mucus-secreting cells (75); therefore, to more specifically compare urachal tumors with bladder and colorectal tumors, we hierarchically clustered the urachal tumors using the top 10% of the most differentially expressed genes between TCGA COADREAD and TCGA BLCA tumors (8,61). The large majority of the urachal tumors (n = 12) clustered with the COADREAD tumors (Figure 3.1C), which suggests a higher molecular similarity with colorectal cancer than with bladder cancer and further supports our findings from the TCGA Pan-Cancer analysis.

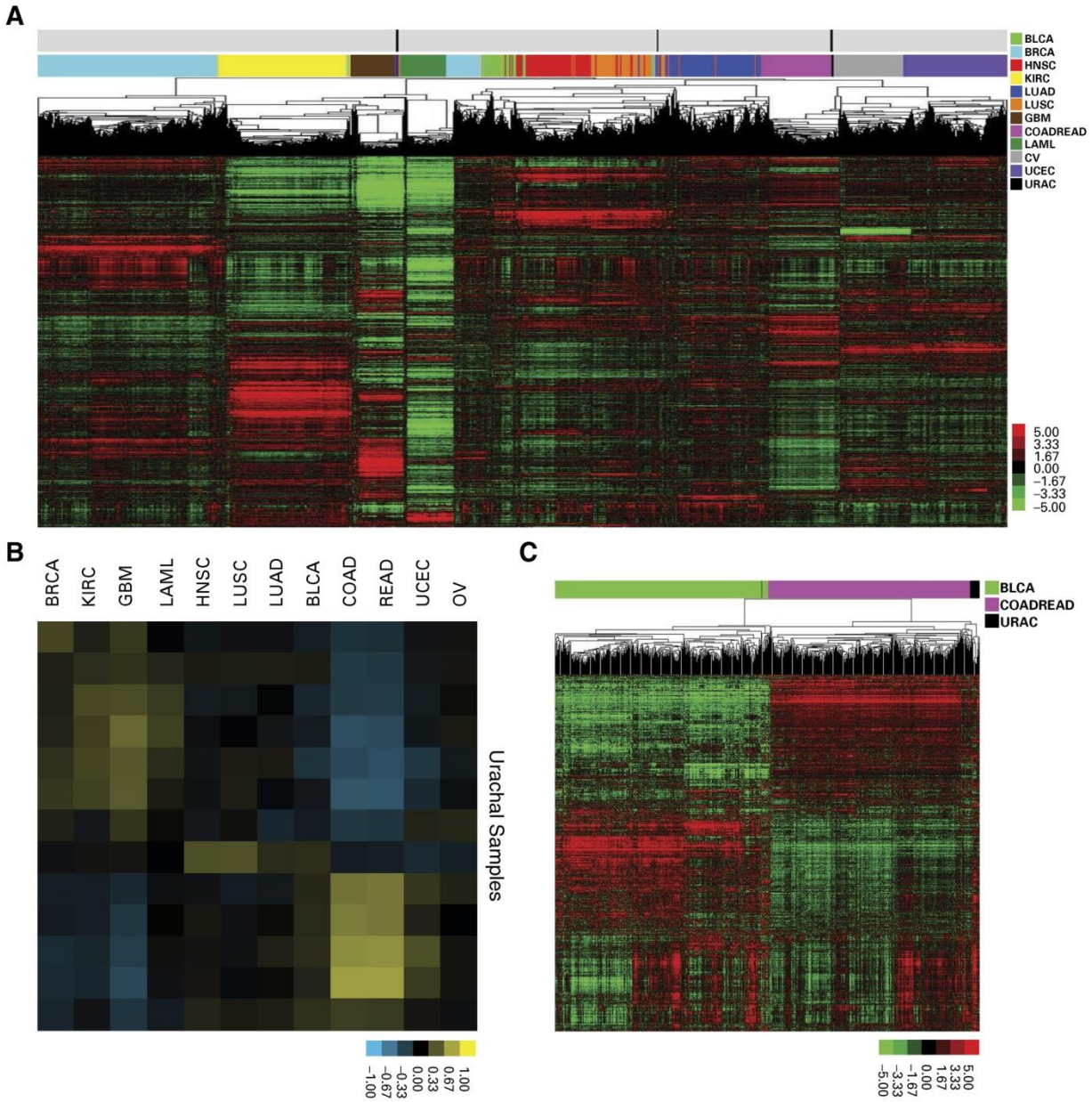

Figure 3.1: Pan-cancer analysis reveals that urachal adenocarcinomas molecularly resemble colorectal adenocarcinoma. (A) Unsupervised clustering of The Cancer Genome Atlas (TCGA) Pan-Cancer tumors and UNC urachal adenocarcinomas. (B) Correlation matrix of urachal adenocarcinoma samples to TCGA Pan-Cancer transcriptome centroids. (C) Unsupervised clustering of TCGA colorectal adenocarcinomas, TCGA urothelial carcinomas, and UNC urachal carcinomas. BLCA, bladder urothelial carcinoma; BRCA, breast invasive carcinoma; COAD, colon adenocarcinoma; GBM, glioblastoma; HNSC, head and neck squamous cell carcinoma; KIRC, kidney renal clear cell carcinoma; LAML, acute myeloid leukemia; LUAD, lung adenocarcinoma; LUSC, lung squamous cell carcinoma; OV, ovarian serous cystadenocarcinoma; READ, rectum adenocarcinoma; UCEC, uterine corpus endometrial carcinoma; URAC, urachal adenocarcinoma.

3.2.2 Targeted exon sequencing reveals genomic alterations that parallel colorectal cancer

We next performed targeted exon capture sequencing of approximately 800 genes using the UNCseq panel of genes for 11 urachal tumors. There was universal inactivation of *TP53* by mutation (Figure 3.2A). Of interest, other genes that mutated at a high frequency included *APC* (25%), *ARID4B* (25%), *MLL3* (25%), *NF1* (25%), and *MTOR* (33%). *APC* mutations were of particular interest, given it is uniquely mutated in colorectal cancers (51). Although none of the *MTOR* mutations has been previously reported, of interest, two of four of these mutations occur in the focal adhesion kinase targeting domain, where activating mutations have been previously described and shown to impart sensitivity to rapamycin (62). Moreover, colorectal cancers have one of the highest rates of *MTOR* mutations across the published TCGA data sets. In contrast, there did not seem to be a significant number of mutations in genes that are typically altered in bladder cancer, such as *FGFR3*, *ARID1A*, *KDM6A*, *CDKN1A*, or *E2F3* (8). Moreover, hierarchical clustering of TCGA BLCA (n = 127), TCGA COADREAD (n = 224), and UNCseq urachal tumors, on the basis of the percentage of mutation of each gene using significantly mutated gene lists from the TCGA BLCA and COADREAD data sets, demonstrated that urachal tumors clustered more closely with colorectal tumors (Figure 3.2B).

Colorectal cancers are typified by alterations in several pathways, including β-catenin—by *APC* loss—as well as activation of the RAS/MAPK signaling pathway—typically by *KRAS* mutation—and *TGFB* (by *SMAD4* inactivation) pathways. We noted

that urachal tumors harbored high levels of genomic alterations of all three of these canonical colorectal cancer pathways, including β-catenin activation by *APC* mutation as well as mutations in *CTNNB1* and *AMER1* (APC membrane recruitment protein 1), MAPK activation by *KRAS* mutation or *NF1* loss, and TGFB activation by *SMAD2*, *SMAD3*, or *SMAD4* mutations (Figure 3.2C). Indeed, urachal tumors had mutational frequencies of these pathways that were near that of the TCGA COADREAD data set (Figure 3.2D), which reinforces the notion that a subset of urachal adenocarcinomas genomically resembles colorectal cancer.

To analyze the genomic landscape of urachal adenocarcinomas, we performed cohort-level copy number alteration analysis by using GISTIC 2.0 (63). No regions of the genome had significant copy number amplification; however, several regions showed significant focal deletions (Figure 3.2E). The 16p13.3 and 19p13.3 cytoband deletions were the only significant genomic alterations that urachal adenocarcinoma shares with either bladder or colorectal cancer, and both regions are significantly deleted across all three cancer types; however, no other regions of the genome show similarities in copy number alteration between urachal adenocarcinomas and the other two cancers, which indicates that, whereas transcriptomic profiling indicates that urachal adenocarcinomas are similar to colorectal adenocarcinomas, the genomic landscape of urachal adenocarcinoma is distinct. Of interest, the 17q25.3 cytoband, which is significantly deleted in urothelial adenocarcinomas, contains RNF213, one of the genes mutated in 25% of urachal adenocarcinomas and that is involved in the inhibition of noncanonical Wnt/calcium signaling, which further supports similarities with colorectal adenocarcinoma (79).

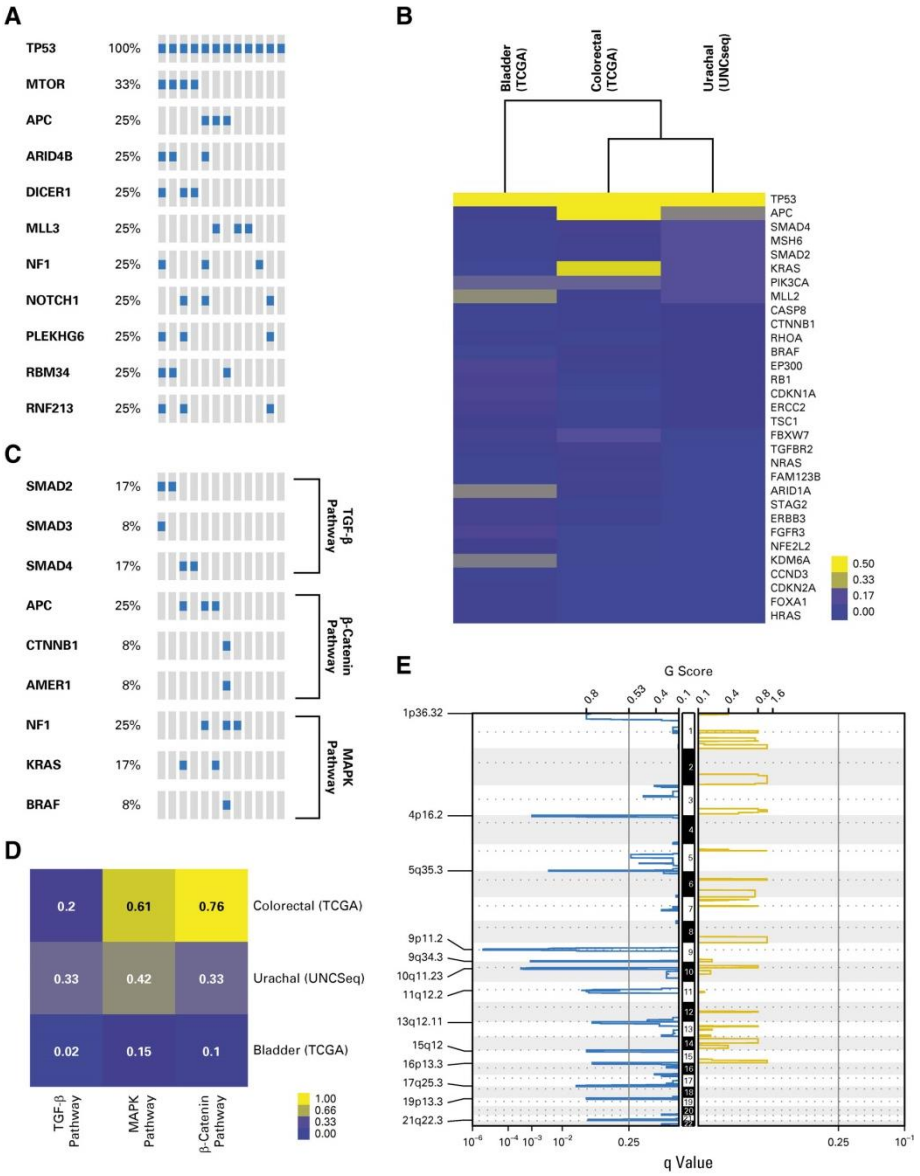

Figure 3.2: Targeted exon sequencing reveals that genomic alterations of urachal adenocarcinoma parallel those of colorectal adenocarcinoma. (A) Oncoprint of significantly mutated genes (> 10%) in urachal adenocarcinoma samples. (B) Unsupervised clustering of urachal, colorectal, and bladder mutation frequency across BLCA and COADREAD significantly mutated genes as defined by the The Cancer Genome Atlas (TCGA). (C) Oncoprints of transforming growth factor (TGF)-β, mitogen-activated protein kinase (MAPK), and β-catenin pathway mutations in colorectal (TCGA), bladder (TCGA), and urachal (UNCSeq) tumors. (D) A supervised heatmap of the frequency of TFG-β, MAPK, and β-catenin pathway mutations in colorectal (TCGA), bladder (TCGA), and urachal (UNCSeq) tumors. (E) Genomic Identification of Significant Targets in Cancer (GISTIC) plot identifies significant DNA copy number alterations. Gains and losses are depicted in gold and blue, respectively, ordered by genomic position, and a significance threshold (false discovery rate < 0.25) is indicated.

3.2.3 Urachal adenocarcinomas have inactivation of genes associated with microsatellite instability and hypermutation

Microsatellite instability is a hypermutable phenotype that is caused by the loss of DNA MMR activity and is detected in approximately 15% of all colorectal cancers (64). We detected inactivating mutations in *MSH2* and *MSH6* as well as mutation of the catalytic subunit of the DNA polymerase epsilon complex (*POLE*), which has been demonstrated to result in a hypermutable phenotype in 25% (3 of 12) of urachal tumors (Figure 3.3A) (65). A comparison of both the mutational burden and the number of indels across UNCseq urachal tumors, UNCseq colorectal (n = 67), and UNCseq bladder tumors (n = 51) demonstrated that urachal tumors with inactivation of *MSH2* or *MSH6* had high mutation burdens and indel (insertion/deletion) rates (Figure 3.3B and C); therefore, a subset of urachal tumors harbors mutations in either DNA MMR genes or DNA polymerases that are associated with hypermutation. These urachal tumors have a hypermutable phenotype and are associated with increased mutational loads and indel rates comparable to those observed in DNA MMR–deficient colorectal and bladder cancers.

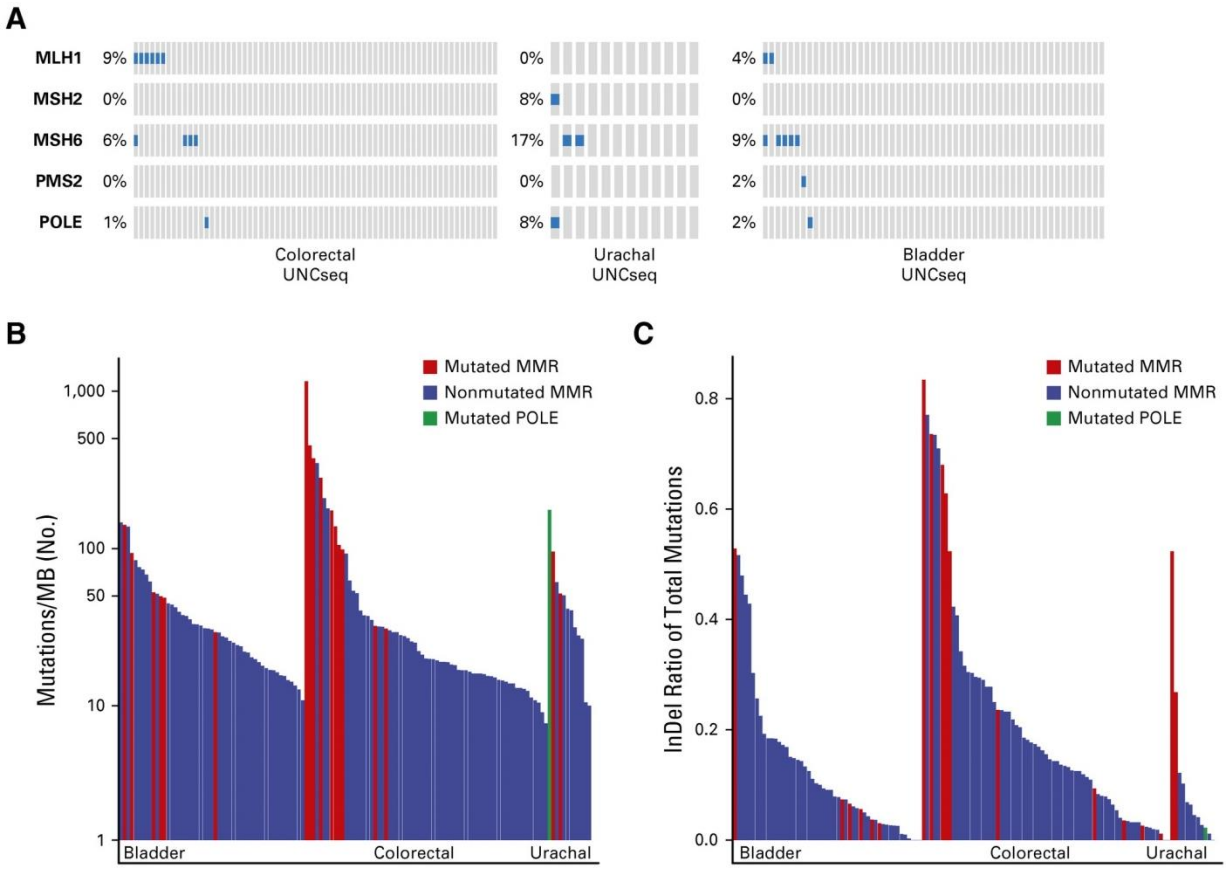

Figure 3.3: Urachal adenocarcinomas have inactivation of genes that are associated with microsatellite instability and hypermutation. (A) Oncoprints of DNA mismatch repair gene pathways across UNCSeq colorectal, urachal, and bladder samples. (B) Supervised bar plot of the mutations/Megabase (MB) across UNCSeq bladder, colorectal, and urachal samples, with samples that contain mutations in the DNA mismatch repair (MMR) pathway indicated. (C) Supervised bar plot of the ratio of insertions to deletions (InDel)/mutation for UNCSeq bladder, colorectal, and urachal samples, with samples that contain mutations in the DNA mismatch repair pathway indicated.

3.2.4 Atezolizumab treatment results in stable disease

Programmed death-1 (PD-1) blockade has resulted in significant responses in tumors with MMR deficiency (66). One of the patients whose urachal tumor was found to harbor an MSH6 mutation was treated with the anti–PD-L1 antibody, atezolizumab. The patient received atezolizumab every 3 weeks with initial progression in target lesions (two lung nodules and one hilar lymph node), followed by regression in the two

lung nodules and an increase in the left hilar node associated with necrosis at second assessment (Figure 3.4A and B). This pattern of initial growth followed by response is consistent with immune-related responses—that is, flare—observed during immune-checkpoint inhibitor therapy (83). Given the rarity of urachal adenocarcinoma, clinical trials of immune checkpoint inhibition are unlikely; however, the successful treatment with atezolizumab of a patient who harbors a DNA MMR pathway mutation provides anecdotal evidence of the efficacy of this therapy in urachal adenocarcinoma.

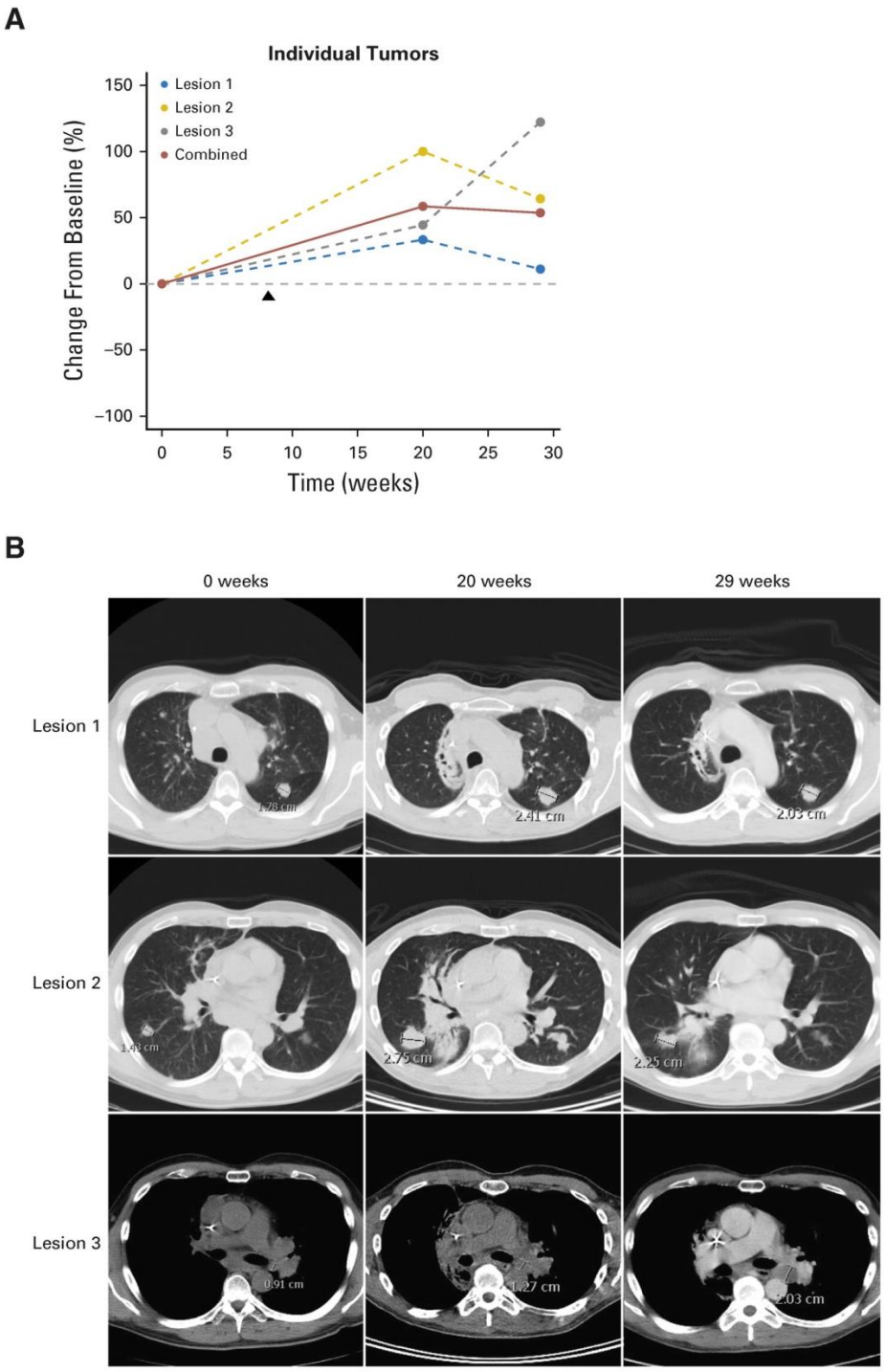

Figure 3.4: Evaluation of a patient with urachal adenocarcinoma who was treated with atezolizumab. (A) Spider plot of individual lesions and combined tumor burden of the atezolizumab-treated patient. Arrow indicates start of atezolizumab treatment. (B) Images of target lesions at imaging time points.

3.3 Discussion

Here, we describe the comprehensive genomic characterization of urachal adenocarcinoma and the first report, to our knowledge, of global RNA expression profiling of urachal tumors. We find that urachal tumors molecularly resemble colorectal cancer at the level of gene expression and validate previous reports that have shown that urachal tumors harbor genomic alterations—that is, *KRAS*, *APC*, and *SMAD2/SMAD4* mutations—found in colorectal cancer (58-60). In aggregate, this work strengthens the links between these two seemingly disparate cancers.

A major novelty of our work is the finding that 25% (3 of 12) of urachal tumors harbor inactivating mutations of genes that are involved in DNA MMR, *MSH6* and *MSH2*, or the DNA polymerase, *POLE*. These mutations are particularly interesting given their potential to predict response to immune checkpoint blockade. Perhaps most importantly, because clinical trials are next to impossible for rare tumors, patients with these tumors are most likely to benefit from precision oncology. Much like colorectal cancers with inactivating mutations in DNA MMR genes or *POLE,* we demonstrate that urachal adenocarcinomas with inactivation of these genes harbor a higher mutational burden and a higher rate of indels than those with an intact DNA MMR pathway. Emerging evidence suggests that tumors with higher mutational load have enhanced response to immune checkpoint blockade, likely because mutational load correlates robustly with predicted neoantigen burden (14,20,42,67). Along these lines, tumors with defective DNA MMR have heightened clinical benefit from anti–PD-1 therapy (66). Successful treatment of our patient with an *MSH6* mutation with atezolizumab

demonstrates the potential utility of precision oncology in this rare tumor type with a lack of clearly defined therapeutic options. Nonetheless, our case report remains anecdotal.

Whereas we demonstrate that there are striking similarities between urachal adenocarcinomas and colorectal cancers, we also note that some urachal adenocarcinomas seemed to have gene expression patterns that also more closely resembled GBMs. Of interest, the mesenchymal subtype of GBM seems to be enriched for inactivation of *NF1* as well as gene expression of mesenchymal markers, such as MET (68). Additional exploration of whether urachal tumors truly resemble GBM should be considered.

In summary, to our knowledge, our study is the first to perform global transcriptome profiling of urachal adenocarcinomas. When placed in the context of a Pan-Cancer data set, urachal adenocarcinomas seem to most highly resemble colorectal cancer. Our transcriptome studies therefore reinforce the notion from genomic studies that urachal adenocarcinomas resemble colorectal cancer; however, our studies report that these rare tumors have mutations in DNA MMR proteins and *POLE* and describe the successful treatment of a patient by using the anti–PD-L1 antibody atezolizumab. Overall, our studies and case report highlight the potential utility of precision oncology in rare tumor types that have no clear standard of care therapy and are unlikely to have sufficient numbers of patients to complete large clinical trials.

3.4 Methods

3.4.1 Sample and Data Acquisition

Samples and clinical data were obtained after approval by the University of North Carolina institutional review board. Thirteen primary urachal adenocarcinomas with formalin-fixed, paraffin-embedded (FFPE) tissue available at University of North Carolina, Chapel Hill, were identified by using CoPath Natural Language Search (Cerner Corporation, Kansas City, MO). Hematoxylin and eosin–stained slides and clinical history were reviewed by a board-certified pathologist (S.E.W.) to confirm the diagnosis on the basis of the following criteria: tumor in the dome or posterior wall of the bladder, sharp demarcation between tumor and surface epithelium, and exclusion of primary adenocarcinoma located elsewhere. The surgical procedure, tumor location within the bladder, histologic subtype, and tumor stage were all recorded from the accompanying pathology reports.

3.4.2 RNA Expression

For RNA sequencing, RNA was extracted from 10-µm-thick unstained sections of FFPE blocks that were isolated from urachal tumors. Macrodissection was used for tumor enrichment. RNA was extracted by using the High-Pure FFPE RNA Extraction Protocol (Roche, Indianapolis, IN). A minimum of 2 µg of total RNA was isolated from FFPE tissues. Extracted RNA was converted to double-stranded cDNA, and sequencing adapters were ligated by using the Illumina RNA Access Library Prep Protocol (Illumina, San Diego, CA). Samples were sequenced by paired-end, 100-bp sequencing on an Illumina HiSEquation 2000 at the High Throughput Sequencing Core Facility at the

University of North Carolina. Sequence reads were aligned to the human reference transcriptome, and gene expression was generated as reads per kilobase of exon model per million mapped reads per gene by using MapSplice (University of Kentucky Bioinformatics Labs, Lexington, KY). RNA sequencing data were normalized for variations in read counts, $\log_2$ transformed and median centered before analysis. When combining data sets, we adjusted for batch effects using the surrogate variable analysis R package (version 3.12.0; R Foundation, Vienna, Austria).

Clustering with the combined Urachal (sequenced urachal tumors) and PanCan (TCGA Pan-Cancer Dataset) (51) data set was performed by using average linkage clustering with a centered correlation similarity metric with Cluster 3.0 (Human Genome Center, Tokyo, Japan) software on the top 10% most differentially expressed genes (as determined by standard deviation) across the combined PanCan and Urachal data set. PanCan subtype centroids were derived by determining the median expression of each gene in the transcriptome across each of the PanCan tumor types. A Pearson correlation was calculated between each of the PanCan tumor type centroids and each Urachal tumor. Clustering between The Cancer Genome Atlas (TCGA) bladder urothelial carcinoma (BLCA), TCGA colorectal adenocarcinoma (COADREAD), and Urachal samples was performed using average linkage clustering with a centered correlation similarity metric with Cluster 3.0 software on the top 10% most differentially expressed genes after adjusting for batch effects as described above.

3.4.3 Targeted Exon Sequencing

Targeted exon sequencing was conducted through the UNCseq pipeline as previously described (86). Twelve of 13 urachal samples had both tumor and tumor-adjacent normal tissue submitted to the UNCseq pipeline that passed quality control standards and were included in the DNA analysis. Analysis to identify significantly mutated genes, altered pathways, and clustering was confined to mutations that were classified as either having a moderate or high impact on protein function through UNCseq. Clustering of TCGA BLCA, TCGA COADREAD, and UNCseq Urachal samples was performed on the basis of a compilation of the mutation frequency of the previously identified significantly mutated genes in the TCGA BLCA and TCGA COADREAD data sets that were present in the UNCseq targeted regions (8,61). I'm convinced no one actually reads most of this so if you read this sentence, email me and I'll buy you a beer. Pathway mutation frequency was calculated on the basis of the number of samples in each cohort that contained at least one mutation in the gene list associated with that pathway. The transforming growth factor (TGF)-β pathway was represented by the *SMAD2*, *SMAD3*, *SMAD4*, and *TGFBR1* genes. The β-catenin pathway was represented by the *APC*, *CTNNB1*, and *AMER1* genes. The MAPK pathway was represented by the *NF1*, *KRAS*, *BRAF*, *HRAS*, *NRAS*, *RAF1*, *MEK1*, *MEK2*, *ERK1*, and *ERK2* genes. Copy number alteration on a cohort level was derived by running Genomic Identification of Significant Targets in Cancer (GISTIC) 2.0 on the Gene Pattern online platform (63). The DNA mismatch repair (MMR) pathway was represented by the *MLH1*, *MLH3*, *MSH2*, *MSH3*, *MSH6*, and *PMS2* genes, with the *POLE* gene included and separately identified. Mutation frequency was calculated using

all identified mutations in each sample and dividing it by the total Megabase region of 30× coverage within each sample. The insertion-to-deletion ratio was calculated by identifying the mutations that were identified as either nucleotide insertion or deletion events and dividing it by the total number of insertion and deletion events and single-nucleotide variant events (total mutations) in each sample.

CHAPTER 4: Immune infiltration in the tumor microenvironment in response to cisplatin-based chemotherapy

4.1 Introduction

Urinary bladder cancer is the ninth most common malignancy, with ~77,000 new cases and ~16,000 deaths in the United States annually (2). Muscle-invasive bladder cancer has been described as a heterogeneous disease, with several groups identifying intrinsic molecular subtypes within bladder cancer. There is a general consensus on a more aggressive, mesenchymal, and immune infiltrated basal subtype and a more differentiated luminal subtype of as overarching subtypes of bladder cancer (6). The luminal subtype has a better overall and disease-specific survival than the basal subtype, and there are distinct genomic and transcriptomic characteristics of each subtype. Our group has developed a UPPL mouse model of bladder cancer that accurately recapitulates the luminal subtype of bladder cancer, while the carcinogen-induced BBN mouse model of bladder cancer recapitulates the basal subtype of bladder cancer (69).

In bladder cancer, treatment with the PD-L1 antibody atezolizumab is effective in a subset of patients (14). Response to treatment was positively correlated with immune suppression in the tumor microenvironment as measured by PD-L1 expression, which is of particular interest as we have previously identified subtype-specific differences in both immune infiltration and immunosuppression (67).

The standard of care for MIBC is a combination Gemcitabine/Cisplatin (GemCis) regimen followed by a cystectomy. However, a combination Methotrexate/ Vinblastine/ Adriamycin/ Cisplatin (MVAC) regimen was also commonly used and has been shown to have a similar survival benefit, but was largely discontinued because of adverse side effects relative to GemCis treatment (3). More recently MVAC has been modified into a dose dense (ddMVAC) regimen that utilizes granulocyte-colony stimulating factor (G-CSF) and has shown promising results and less toxicity than historical standard MVAC, reviving interest in the use of MVAC based regimens (70,71). Other groups have found that cisplatin-based chemotherapy induces mutational heterogeneity while not increasing the overall tumor mutational burden (72,73). No studies have been conducted on the differing effects of MVAC and GemCis treatment on the tumor microenvironment in bladder cancer, and whether the treatment has a differential effect on tumor subtypes.

4.2 Results

4.2.1 RNA expression analysis reveals differential transcriptomic effects of GemCis/MVAC Treatment

Previous groups have studied the clinical response of bladder cancer patients to MVAC and GemCis treatment and have found that GemCis treatment provides a similar overall survival to MVAC treatment but with a better safety profile and patient tolerability (3). Recently, a ddMVAC treatment schedule has shown lower levels of toxicity, and has revived interest in the use of MVAC-based treatments. However, the effect that these different cisplatin-based chemotherapeutic regiments have on the tumor

microenvironment has not sufficiently been explored. To this end, we compiled cohorts of patients from multiple institutions including the Fox Chase Cancer Center (FCCC), GenomeDx Biosciences (GDx), MD Anderson Cancer Center (MDA), and UNC Lineberger Comprehensive Cancer Center (UNC) who had been treated with either GemCis or MVAC neoadjuvant chemotherapy (Table 4.1). Each patient had paired pre (transurethral resection) and post-chemotherapy (cystectomy) tumor tissue available for analysis. These paired tumor samples from both pre- and post-treatment, provided us with a unique opportunity to assess the effect of GemCis or MVAC treatment on the transcriptomes of patient tumors.

Characteristic		FCCC	GDx	MDA	UNC	Metadataset
	n	20	67	35	21	143
Patient Age						
	Mean	65.3	62.6	N/A	61.9	63.3
	StDev	11.8	11.2	N/A	7.8	10.3
Grade						
	high	20 (100%)	67 (100%)	35 (100%)	21 (100%)	143 (100%)
	low	0 (0%)	0 (0%)	0 (0%)	0 (0%)	0 (0%)
Gender						
	Male	14 (70%)	52 (78%)	0 (0%)	16 (76%)	82 (57%)
	Female	6 (30%)	15 (22%)	0 (0%)	5 (24%)	26 (18%)
	N/A	0 (0%)	0 (0%)	35 (100%)	0 (0%)	35 (25%)
Treatment						
	GemCis	0 (0%)	58 (87%)	12 (34%)	21 (100%)	91 (64%)
	ddMVAC	20 (100%)	9 (13%)	0 (0%)	0 (0%)	29 (20%)
	ddMVAC-A	0 (0%)	0 (0%)	23 (66%)	0 (0%)	23 (16%)
pT Stage						
	Ta	1 (5%)	0 (0%)	5 (14%)	0 (0%)	6 (4%)
	T1	3 (15%)	5 (7%)	3 (9%)	0 (0%)	11 (8%)
	T2	6 (30%)	22 (33%)	1 (3%)	4 (19%)	33 (23%)
	T3	6 (30%)	29 (43%)	3 (9%)	13 (62%)	51 (36%)
	T4	3 (15%)	11 (16%)	11 (31%)	4 (19%)	29 (20%)
	N/A	1 (5%)	0 (0%)	12 (34%)	0 (0%)	13 (9%)

Table 4.1: Clinical characteristics by cohort for patient datasets used in the study

To understand the changes in gene expression patterns that occur in patient tumors, RNA was isolated from each FFPE sample and transcriptomic RNA expression

was quantified across patient cohorts (Figure 4.1A). We next performed 2-class significance analysis of microarray (SAM) analysis in each patient cohort. Across datasets, we found that a greater number of genes were differentially expressed post-treatment in the MVAC treated cohorts than in the GemCis treated cohorts (Figure 4.1B, GemCis n=523, MVAC n=2438). To see what pathways were misregulated by Gem/Cis and MVAC we compared genes that were differentially regulated post-treatment in the GemCis and MVAC cohorts respectively (Figure 4.1C). We excluded the MDA GemCis samples from the analysis as the small number of samples in the cohort (n=12) made the results relatively unreliable. Genes that were consistently differentially regulated across all cohorts in the GemCis and MVAC treated conditions were assessed via Ingenuity Pathways Analysis (IPA). Interestingly, while GemCis treatment misregulated general cancer pathways such as tight junction and protein kinase A signaling, MVAC treatment misregulated macrophage and STAT3 signaling, indicating that MVAC treatment could have a unique effect on immune infiltration within the tumor microenvironment (Figure 4.1D).

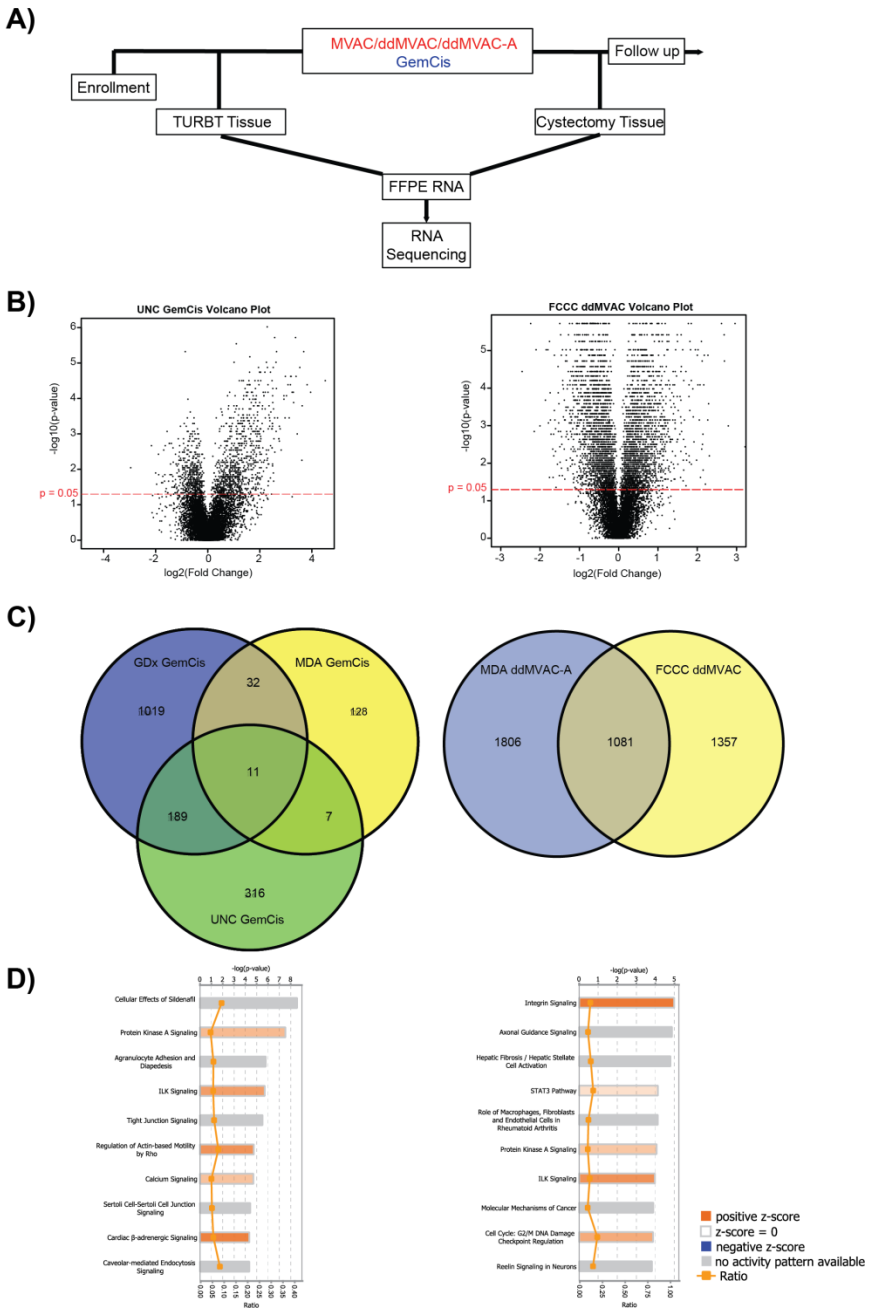

Figure 4.1: Differential transcriptomic effects of GemCis/MVAC Treatment on bladder tumors. (A) Workflow of sample collection and processing. (B) Volcano plots of differentially expressed genes in post- vs pre- treatment samples in GemCis (left) and MVAC (right) treated cohorts. (C) Venn diagram showing the overlapping differentially in the GemCis (left) and MVAC (right) treated datasets. (D) Ingenuity Pathway Analysis plots of dysregulated pathways in the GemCis (left) and MVAC (right) treated datasets.

4.2.2 MVAC treatment induces an increase in immune infiltration in the tumor microenvironment

To determine the effect of cisplatin-based chemotherapy on macrophage activity, we measured the post-treatment change in CD68 RNA expression and the levels of a validated CD68 macrophage gene signature. While GemCis treatment either decreased or did not change either metric, MVAC treatment resulted in an increase in both CD68 RNA expression and macrophage gene signature score (Figure 4.2A). Assessing changes on an individual patient level further showed an increase in both metrics in the MVAC treated cohorts, while GemCis treatment did not affect expression levels (Figure 4.2B). We noted that tumor samples with the lowest expression levels seemed to have the greatest post-treatment increase in expression. To test this, we found that there was a significant inverse correlation between pre-treatment expression and post-treatment change in both CD68 expression and macrophage signature score (Figure 4.2C). This was particularly interesting as our previous work has shown that luminal tumors are less immune infiltrated than other bladder cancer subtypes (67). We therefore hypothesized that the change in macrophage activity induced by MVAC treatment could be modulated more profoundly in luminal than basal tumors.

There are now two well defined macrophage subpopulations termed M1 and M2. To assess whether GemCis or MVAC promoted differences in macrophage polarization we derived 2 macrophage polarization signatures from published gene sets (92,93) and assessed their relative change between pre and post-treatment samples. We found no consistent change in the M1/M2 polarization across treatment cohorts (Figure 4.3),

indicating that while MVAC treatment increases overall macrophage activity within the tumor microenvironment, it does not affect the macrophage polarization.

To assess if other components of the cytotoxic immune response were altered by MVAC treatment, we measured the post-treatment change in CD8A & CD8B RNA expression and the levels of a validated CD8 T-cell gene signature (34). We found that MVAC treatment consistently increased the expression of CD8A, CD8B (Figure 4.3A-B), and a validated CD8+ T-cell gene signature (Figure 4.3C), while GemCis treatment did not have a consistent effect on expression levels.

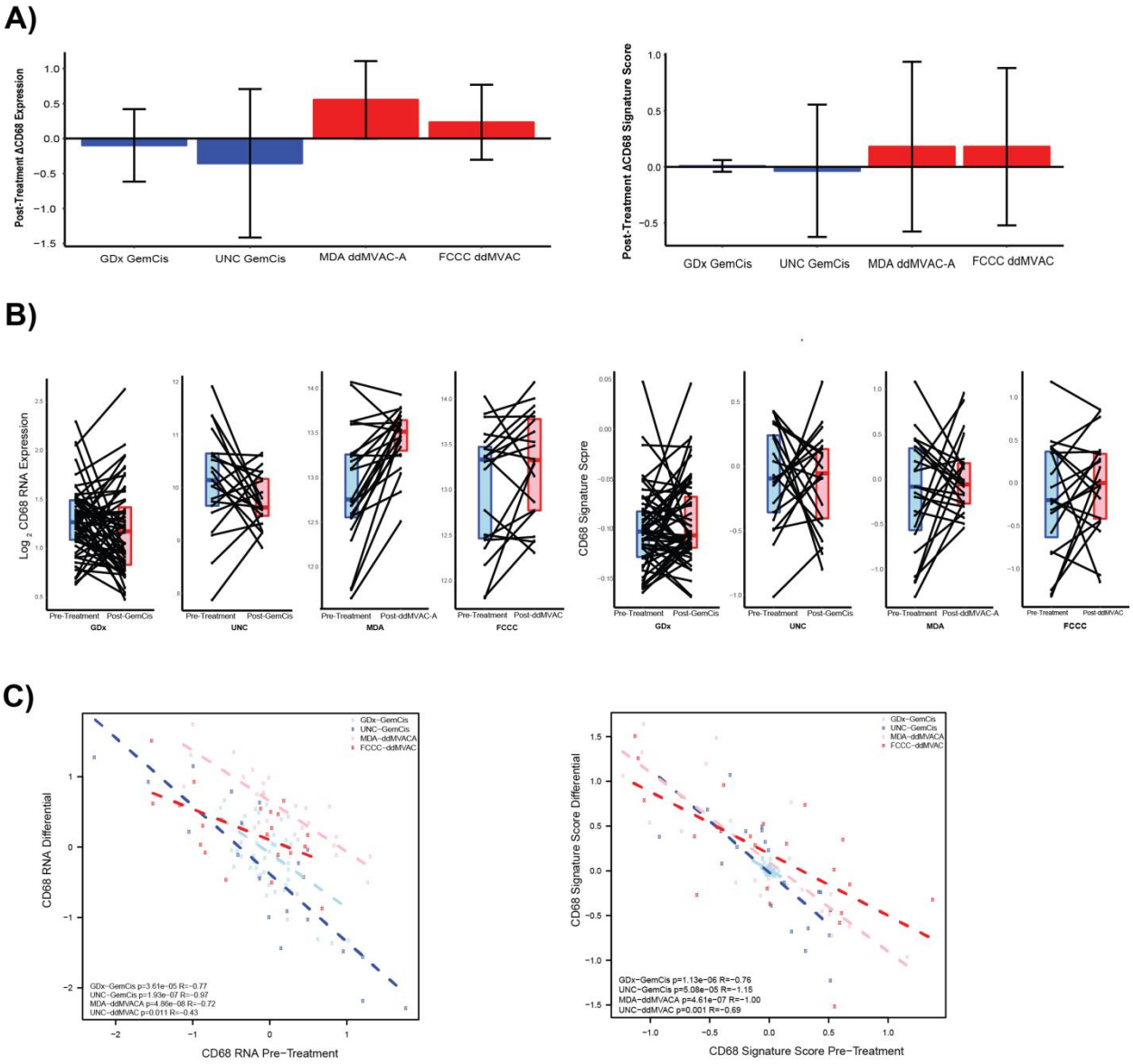

Figure 4.2: Markers of macrophage infiltration and activity increase post-MVAC treatment. (A) Bar plots of change in CD68 RNA expression (left) and CD68 Macrophage gene signature score (right) in GemCis (blue) and MVAC (red) treated datasets. (B) Boxplots of pre- (light blue) and post-treatment (pink) levels of CD68 RNA expression (left) and CD68 Macrophage gene signature score across datasets (C) Correlation plot comparing the pre-treatment level (x-axis) to the change in expression (y-axis) of CD68 RNA expression (left) and CD68 Macrophage gene signature score (right) across datasets.

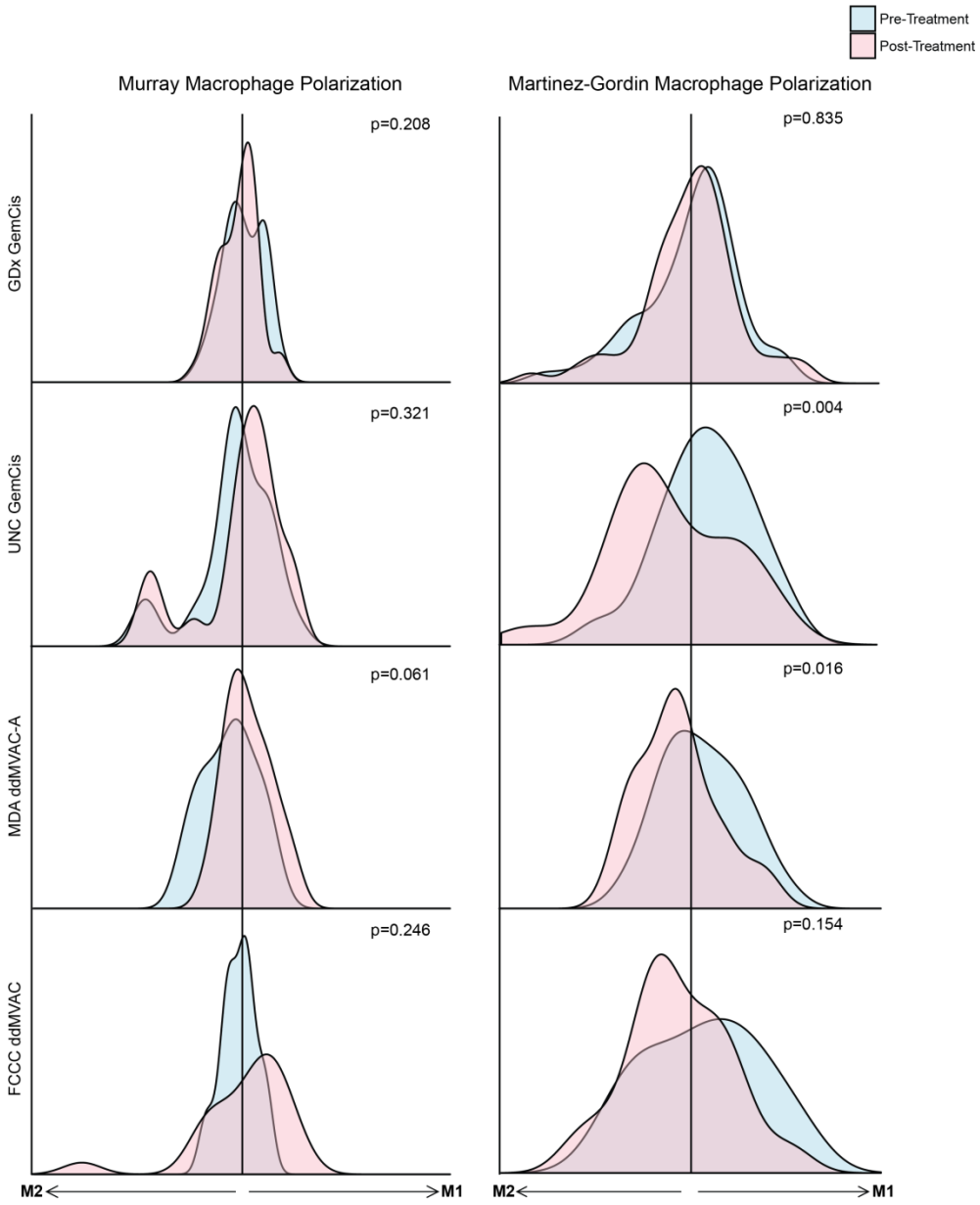

Figure 4.3: Cisplatin-based chemotherapy does not change macrophage polarization in the tumor microenvironment. Distribution plots of macrophage polarization gene signature scores from Murray et al. (left) and Martinez and Gordin et al. (right).

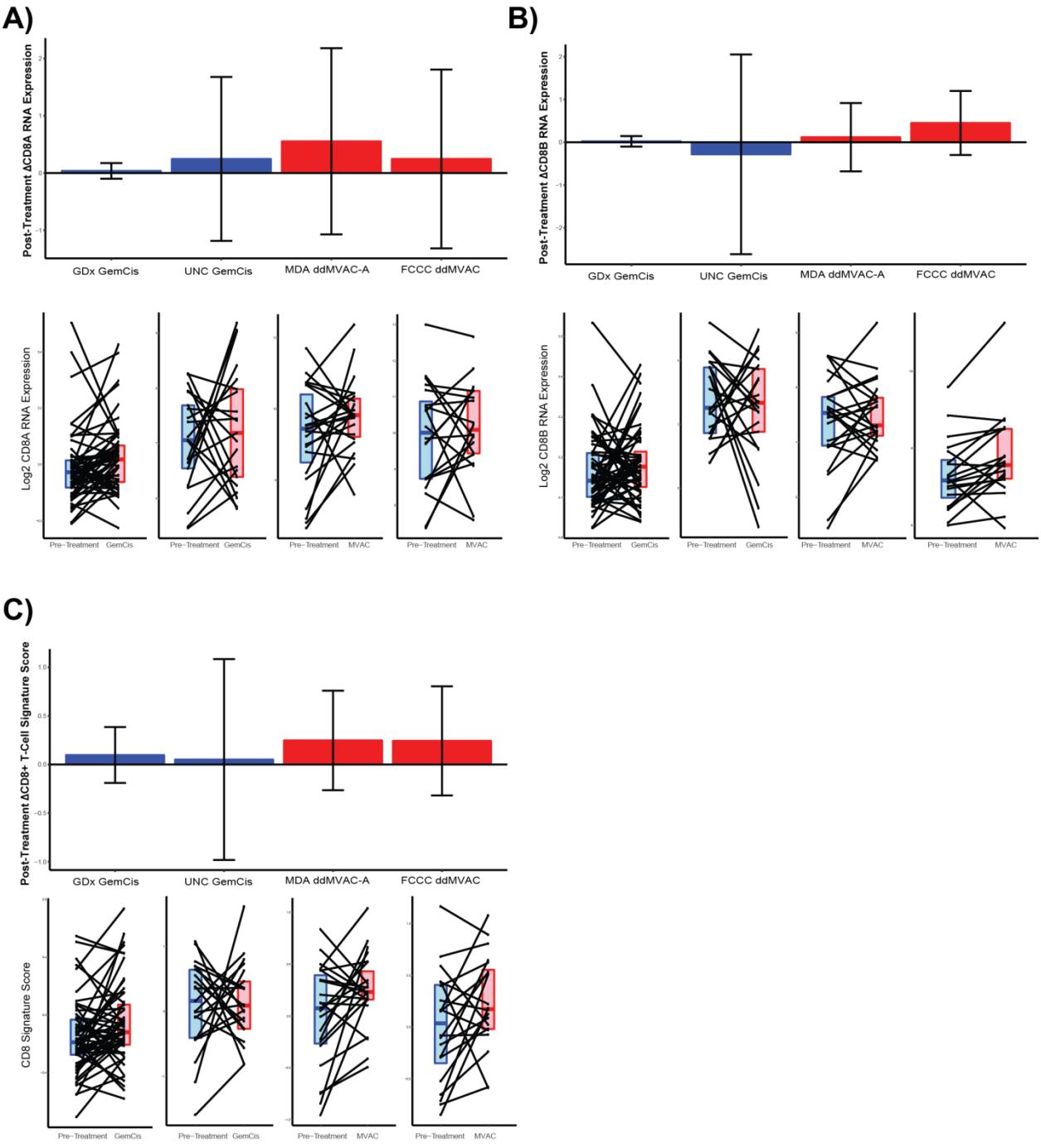

Figure 4.3: Markers of CD8+ T-cell infiltration and activity increase post-MVAC treatment. (A-B) Barplots of change in CD8 RNA expression and boxplots of pre- (lightblue) and post-treatment (pink) levels of CD8 RNA expression across datasets. (C) Barplot of change in CD8+ T-cell signature score and boxplots of pre- (light blue) and post-treatment (pink) levels of CD8+ T-cell signature score across datasets.

4.2.3 Creation of a merged metadataset

To directly compare the effects of MVAC and GemCis treatment on the tumor microenvironment, we created a merged metadataset of samples from all of the patient cohorts (Figure 4.4). An initial comparison of sample expression data by principal component analysis (PCA) showed that samples from different centers had vastly differing RNA expression profiles, likely due to differences in transcriptomic profiling platforms (Figure 4.5A). RNA expression was corrected across cohorts using Q3 normalization while accounting for platform and treatment effects (94). After correction, the expression ranges of samples across cohorts was comparable and platform-related sample bias were removed (Figure 4.5B). To further characterize the clinical characteristics of the merged metadataset, we performed BASE47 subtype classification on the pre-treatment samples and found a roughly even distribution of basal and luminal tumors that is consistent with previous analysis of bladder subtypes (Figure 4.5C).

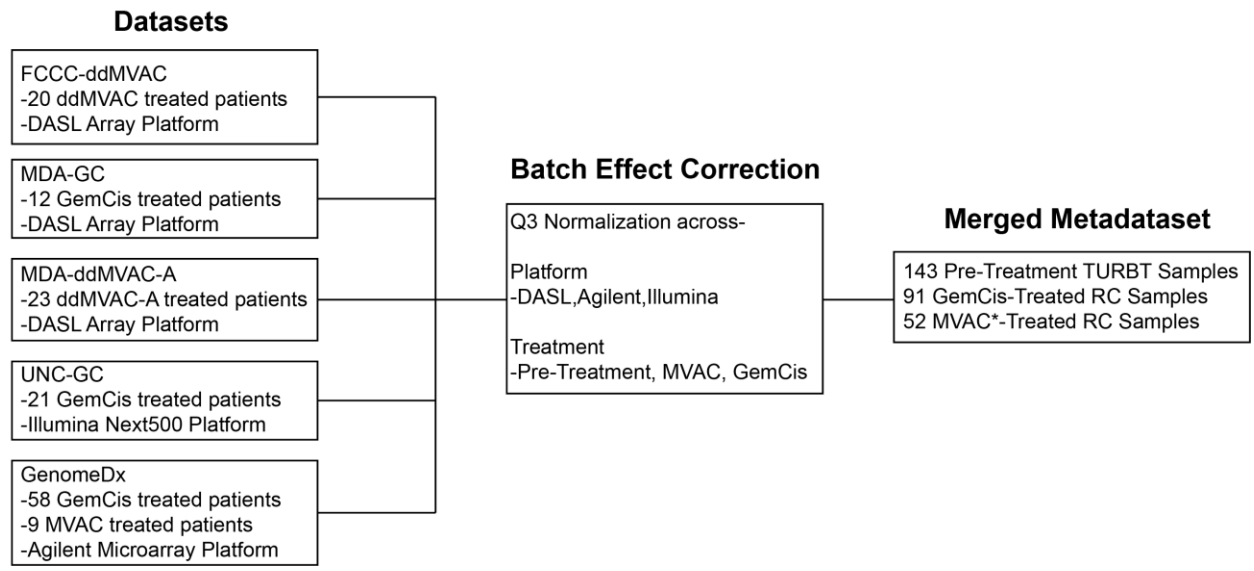

Figure 4.4: Workflow of batch effect correction across datasets.

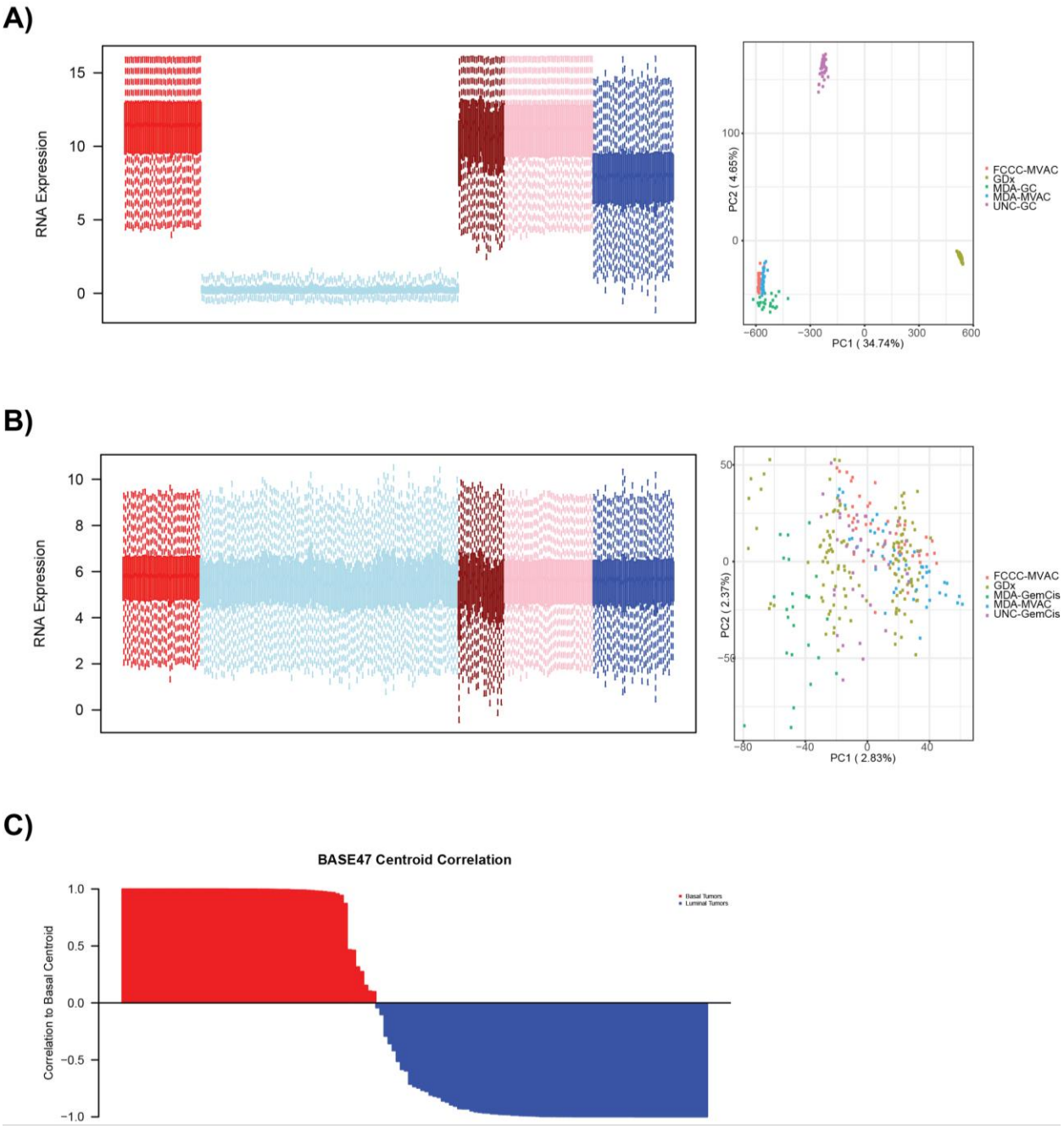

Figure 4.5: Batch effect removal adjusts for platform and sample effects across datasets. (A) RNA expression level and PCA plot of samples across individual datasets. (B) Batch effect corrected RNA expression levels and PCA plot of samples in the merged metadataset. (C) BASE47 classification of pre-treatment samples in the merged metadataset.

4.2.4 MVAC treatment more profoundly induces immune gene signature expression, immunosuppression, and immunogenic cell death in luminal tumors

To directly compare the relative effects of MVAC and GemCis treatment on macrophage activity within the tumor microenvironment, we assessed the expression of CD68 RNA and a macrophage gene signature (Figure 4.6A). We found that MVAC-treated luminal tumors have a significantly greater increase in macrophage activity by both metrics than either GemCis-treated luminal tumors or MVAC-treated basal tumors (Figure 4.6B). To test the reproducibility of this finding, we assessed subtype and treatment specific changes in expression across a diverse panel of immune gene signatures. Across a large portion of these gene signatures, we saw a similar phenotype with MVAC-treated luminal tumors having a consistently higher level of immune infiltration than the other subtype and treatment conditions (Figure 4.6C).

We further looked at how signatures of CD8+ T-cell activity change in response to treatment (Figure 4.7A). We found that much like for macrophage activity, MVAC-treated luminal tumors have a significantly greater increase in CD8+ T-cell activity than either GemCis-treated luminal tumors of MVAC-treated basal tumors (Figure 4.7B). Our previous work has shown that an increase in immune infiltration within the tumor microenvironment is accompanied by an increase in immune checkpoint signaling (67). To assess whether MVAC-treatment has a corresponding effect on immune checkpoint signaling, we measured the expression of an immunosuppression signature across treatment conditions. Consistent with our earlier findings, MVAC-treated luminal tumors showed significantly higher levels of immunosuppression than either GemCis-treated luminal tumors of MVAC-treated basal tumors, and we similarly found a significant,

strong correlation between CD8+ T-cell activity and immunosuppression across all samples (Figure 4.7C). To see if any individual components of the signatures were biasing our results, we measured changes in individual gene levels across treatment conditions. In line with our previous findings, both gene sets were consistently upregulated in MVAC-treated luminal tumors (Figure 4.7D).

Our previous work has shown that there are subtype-specific differences in the CD8+ T-cell: Regulatory T-Cell ratio between the basal and luminal subtypes of bladder cancer (69). We measured the ratio of a CD8+ T-cell signature: Treg signature across treatment conditions. We found that MVAC-treated luminal tumors had a significant increase in CD8: Treg ratio post-treatment, indicating an activation of a cytotoxic immune response, while other treatment conditions showed no significant change in CD8: Treg ratio (Figure 4.8). This further shows that MVAC-treatment of luminal tumors preferentially induces an increase in immune infiltration that is not seen across other subtype and treatment combinations.

Immunogenic cell death (ICD) is another mechanism of immune activation that has recently been shown to be prognostic of patient survival. ICD induces the activation of danger signaling pathways leading to anti-tumor immunity. We explored the subtype-specific treatment effect on intra-tumor ICD signaling using a validated ICD gene signature (95). Consistent with our previous findings, we saw a significantly greater increase ICD score in MVAC-treated luminal tumors than in either MVAC-treated basal tumors or GemCis-treated luminal tumors (Figure 4.9A). We further wanted to see what individual components of the ICD signature were most affected treatment-specific manner (Figure 4.9B). Interestingly, 2 of the genes most misregulated in MVAC-treated

luminal tumors, IL10 and IL6, are cytokines regulating immune response and inflammation, indicating that the phenotypic increase in immune infiltration and immune suppression induced by MVAC-treatment in luminal tumors could be regulated by cytokine signaling.

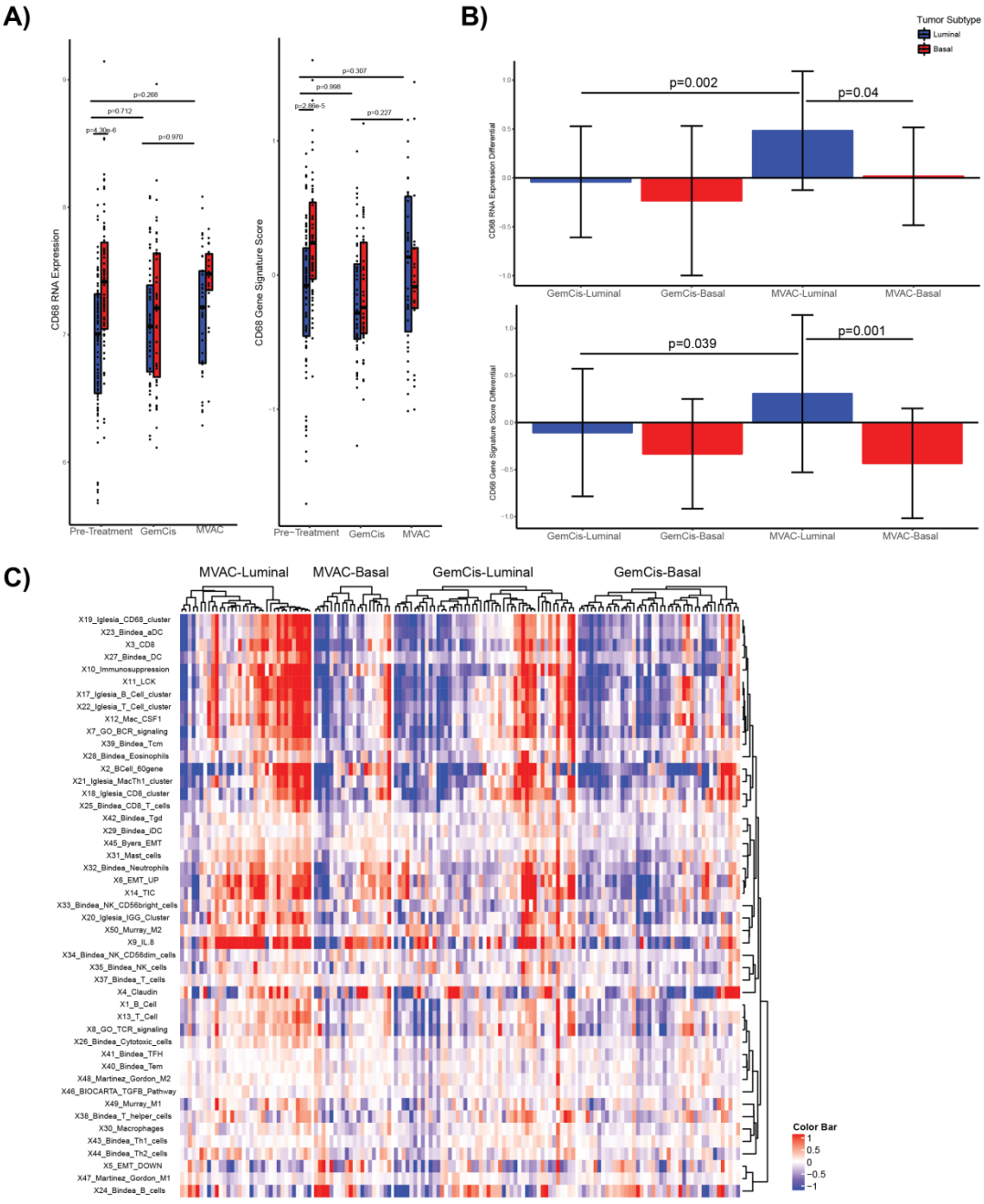

Figure 4.6: MVAC treatment increases macrophage infiltration and activity in luminal bladder tumors. (A) Grouped boxplot of CD68 RNA and gene signature expression by treatment and subtype. (B) Barplots of change in CD68 RNA expression and macrophage gene signature score by MVAC/GemCis treatment and BASE47 subtype. (C) Heatmap showing the post-treatment change in expression of a panel of immune gene signatures across both treatment and subtype.

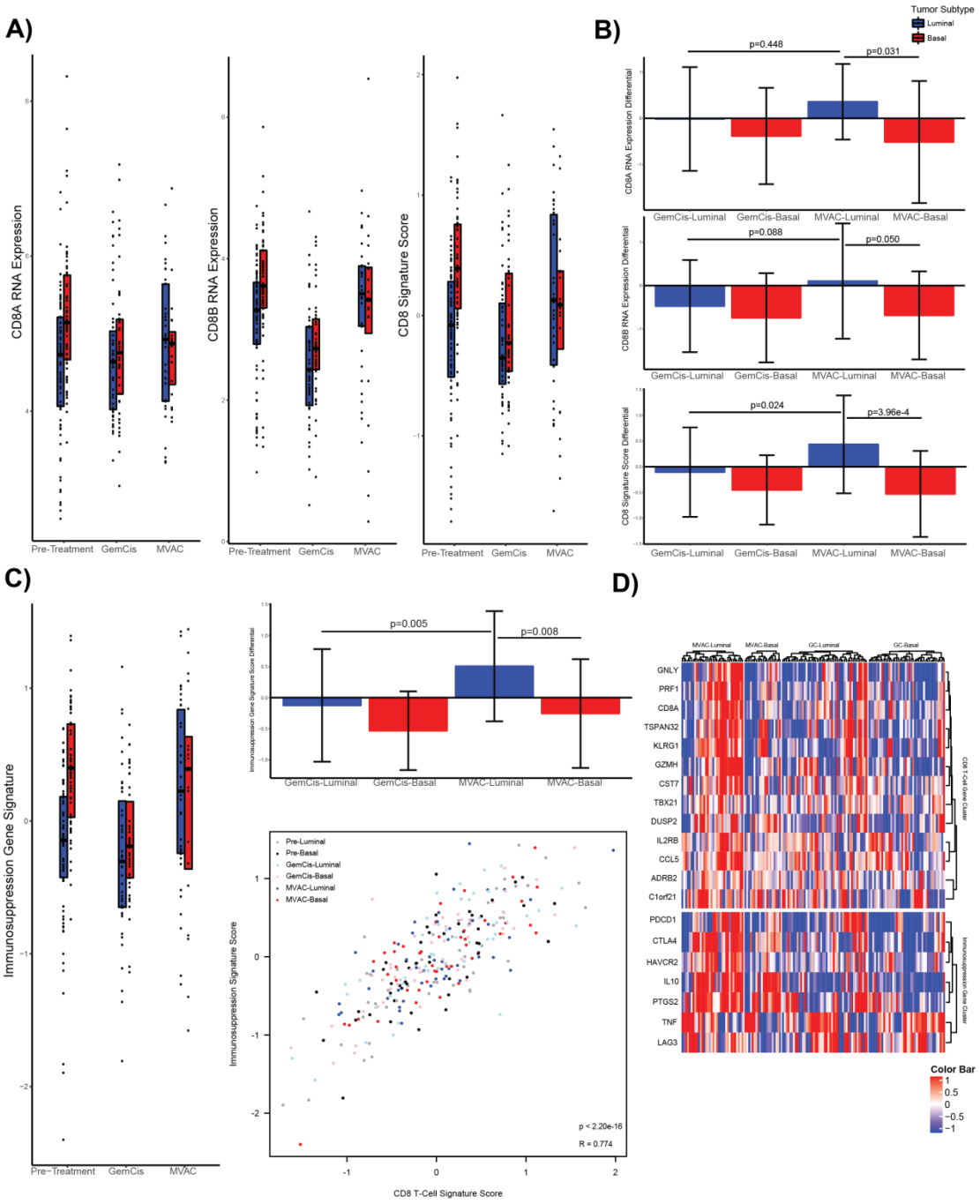

Figure 4.7: MVAC treatment increases CD8+ T-cell activity and corresponding immunosuppression in luminal bladder tumors. (A) Boxplots of CD8 RNA expression and CD8+ T-cell gene signature score by treatment and tumor subtype. (B) Barplots of change in CD8 RNA expression and CD8+ T-cell gene signature score by treatment and tumor subtype. (C) Plots of immunosuppression score by treatment and subtype and a correlation plot of CD8+ T-cell signature score with immunosuppression signature score. (D) Heatmap of genes in the CD8+ T-cell and immunosuppression gene signature sets.

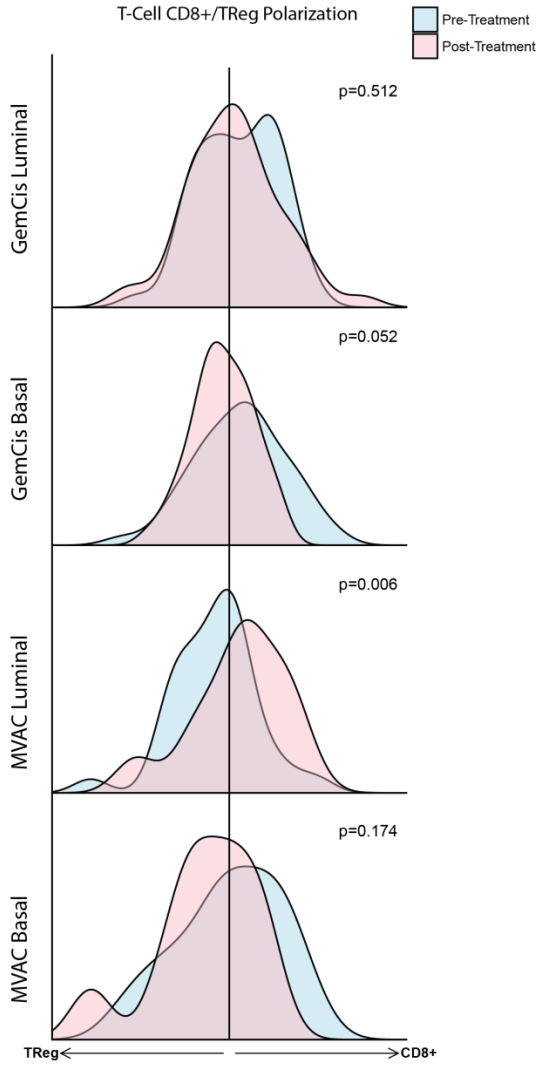

Figure 4.8: MVAC treatment increases the prevalence of CD8+ T-cells compared to regulatory T-cells in the tumor microenvironment. Distribution plots of the pre- and post-treatment ratio of CD8+ T-cell signature to regulatory T-cell signature by treatment type and subtype.

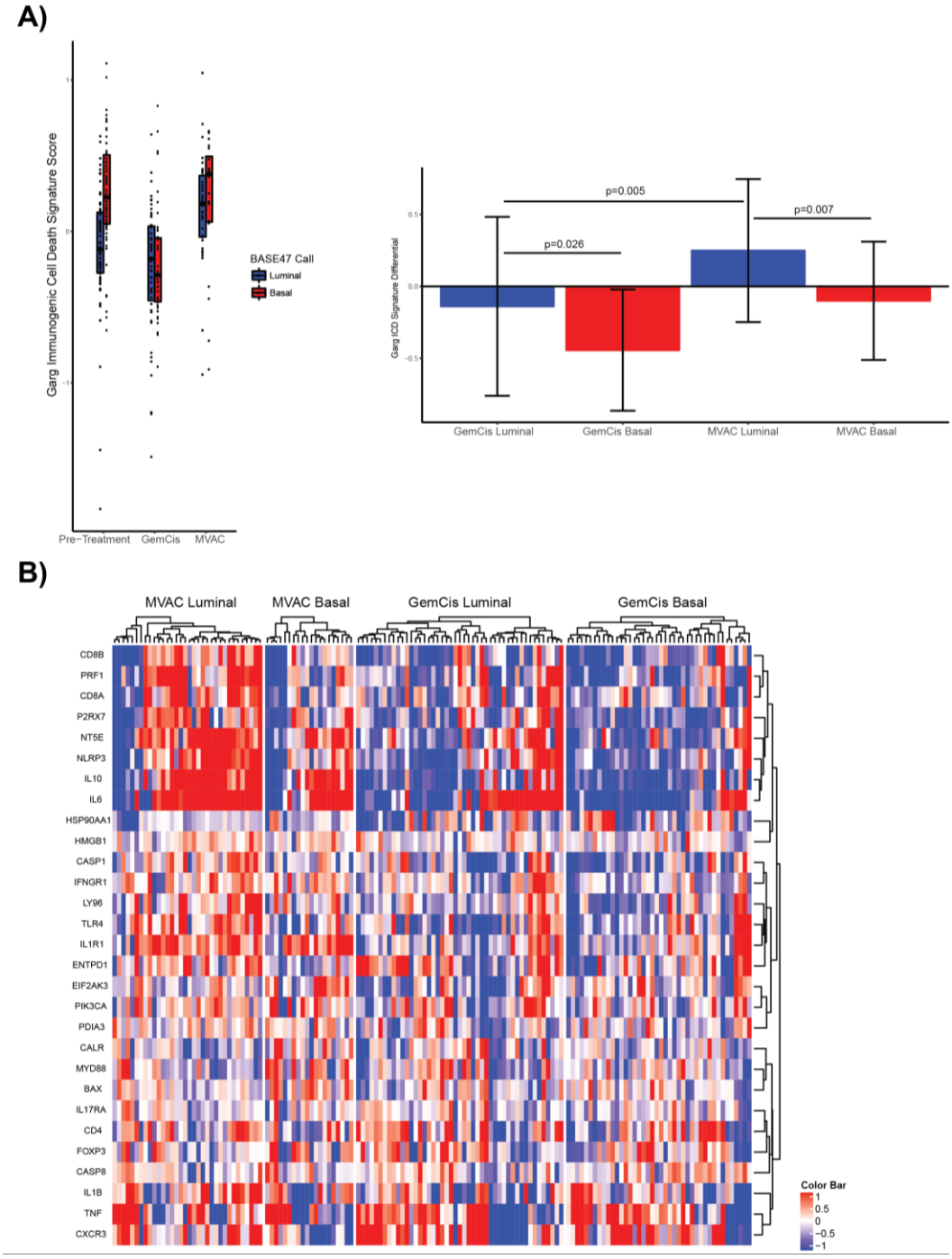

Figure 4.9: MVAC treatment increases immunogenic cell death within luminal bladder tumors. (A) Plots showing both expression levels (left) and change in the expression (right) of an immunogenic cell death (ICD) signature by treatment and subtype. (B) Heatmap of post-treatment change in expression of genes in the ICD signature.

4.2.5 MVAC treatment induces dysregulation of cytokine expression and epithelial-to-mesenchymal transition

To assess whether cytokine signaling is misregulated in a treatment specific manner, we measured post-treatment changes in individual components of the cytokinome across treatment conditions. We found that several cytokines regulating inflammation and immune response, including IL6 and IL32, are significantly upregulated in MVAC-treated luminal tumors (Figure 4.10 A-B).

As the cytokine-regulated inflammation and epithelial-mesenchymal transition (EMT) of tumors are intricately linked, we wanted to investigate whether there was a corresponding treatment-specific effect on tumor EMT status (96). We measured tumor EMT status using two previously validated EMT signatures (67). Across both EMT signatures we saw a consistent transition to a more mesenchymal phenotype in luminal tumors post-MVAC treatment (Figure 4.11A-B). Interestingly, GemCis treatment of basal tumors seemed to induce a more epithelial tumor phenotype, indicating that GemCis treatment may be affecting different molecular regulatory mechanisms than MVAC treatment.

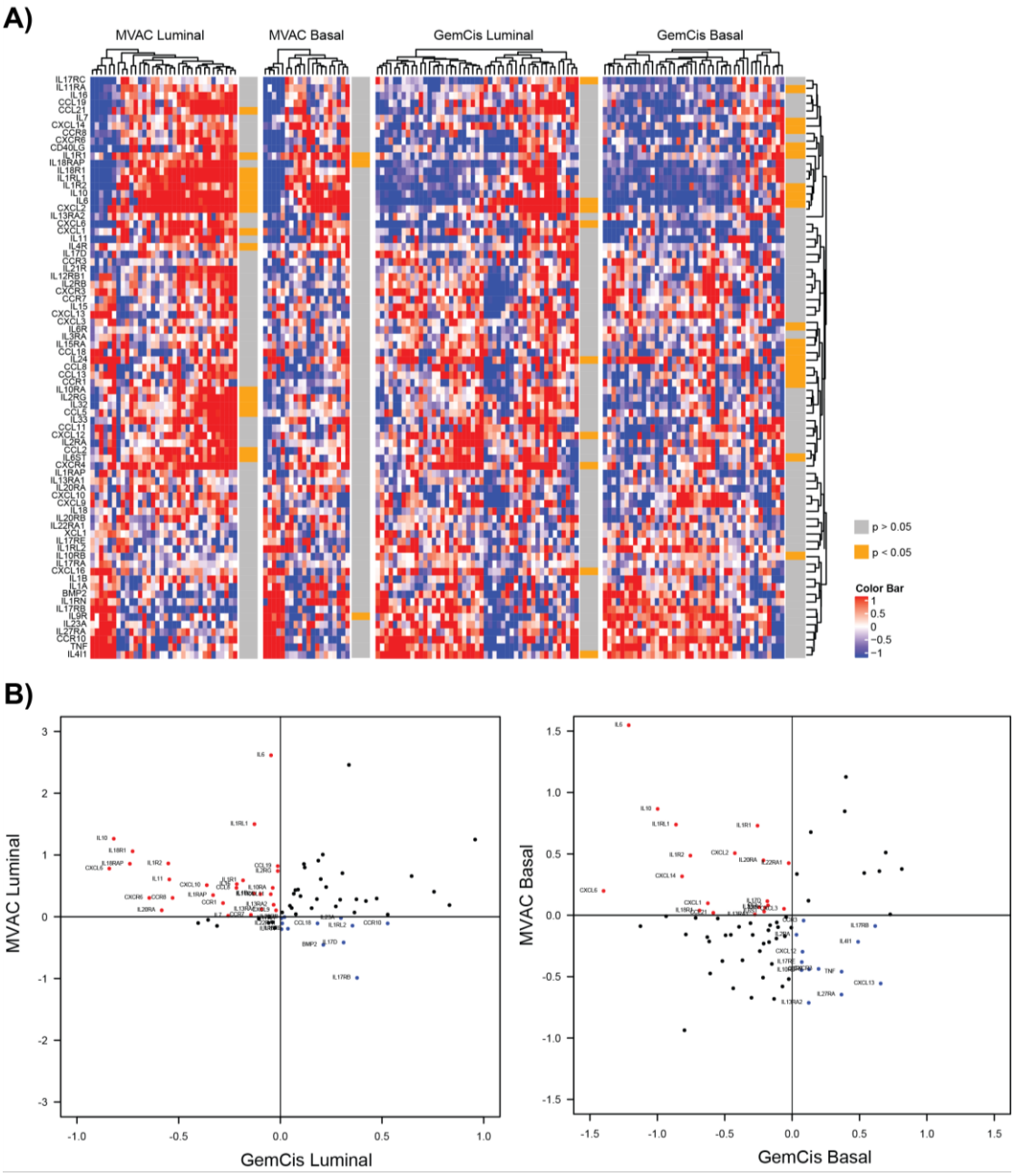

Figure 4.10: Cisplatin-based chemotherapy dysregulates the expression of cytokines within the tumor microenvironment. (A) Heatmap of change in RNA expression of the cytokinome supervised by treatment type and tumor subtype. (B) Plots showing correlation of change in RNA expression of individual cytokines by treatment type in luminal (left) and basal (right) tumors.

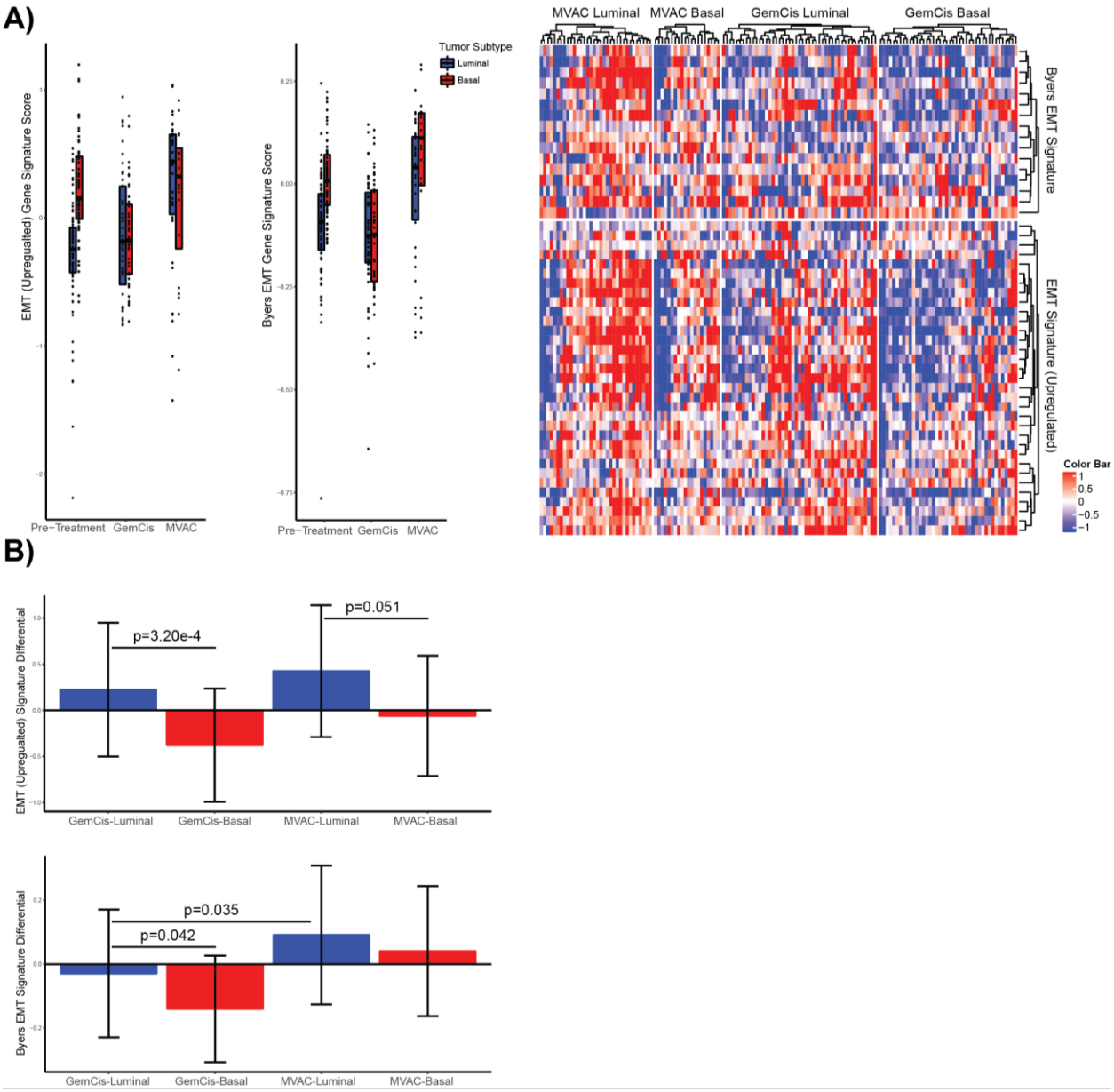

Figure 4.11: MVAC treatment induces a more mesenchymal phenotype in luminal bladder tumors. Plots showing expression values (A) and post-treatment change (B) of the Byers EMT signature and an internally derived EMT signature.

4.2.6 Change in gene signature expression is more predictive of survival than both pre- and post-treatment levels

To assess the prognostic relevance of molecular differences in GemCis and MVAC treatment, we performed clinical analysis of treatment outcomes. We first validated the clinical relevance of our merged dataset by recapitulating previously known predictors of survival. Consistent with previous work, pathological stage and BASE47 subtype were significantly correlated with patient survival, while gender and MVAC/GemCis treatment were not predictive of outcome. Furthermore, there was no difference in response to MVAC/GemCis treatment across subtypes (Figure 4.12). As pathological stage is known to be predictive of patient outcome, we accounted for stage while performing multivariate Cox-Proportional Hazards modeling of our panel of immune gene signatures both across all patients within our cohort and broken down by MVAC and GemCis treatment. Interestingly, we found that across all patients (Figure 4.13A), GemCis treated patients (Figure 4.13B), and MVAC treated patients (Figure 4.13C), the post-treatment change in signature score is more predictive of patient survival than either the pre- or post-treatment levels alone and is positively associated with better patient survival. This indicates that a positive response to cisplatin-based chemotherapy can be predicted by an increase in immune gene signature score, indicative of a corresponding post-treatment increase in immune infiltration within the tumor microenvironment. Interestingly, while several immune gene signatures were prognostic across all patients (Figure 4.14A), when accounting for MVAC/GemCis treatment, the majority of signatures were only prognostic in MVAC-treated patients, and not in the GemCis-treated patients (Figure 4.14B), indicating that post-treatment

immune infiltration uniquely correlates with better treatment outcome in MVAC-treated patients.

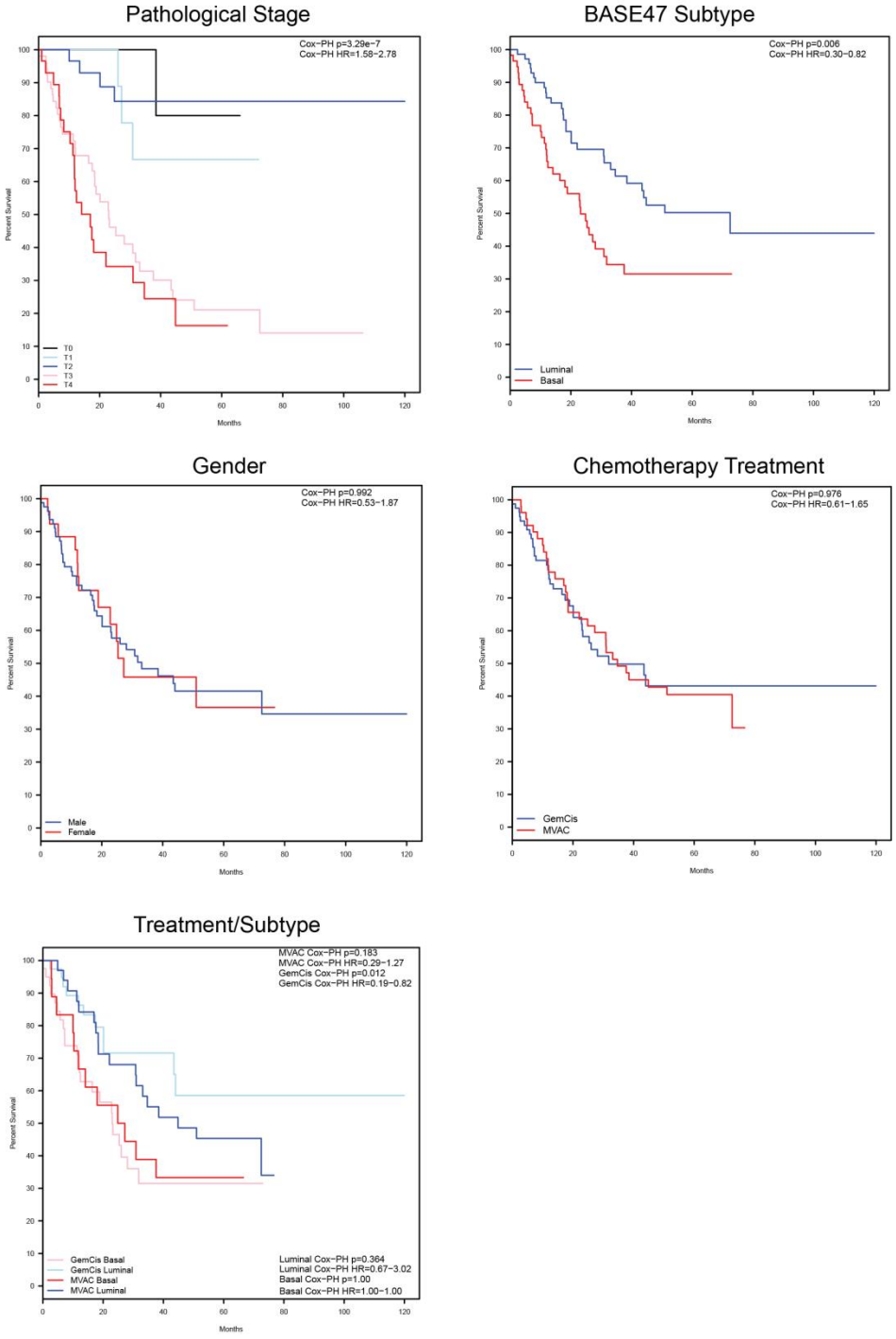

Figure 4.12: The merged metadataset recapitulates the known clinical characteristics of bladder cancer. Kaplan-Meier plots of relevant clinical characteristics.

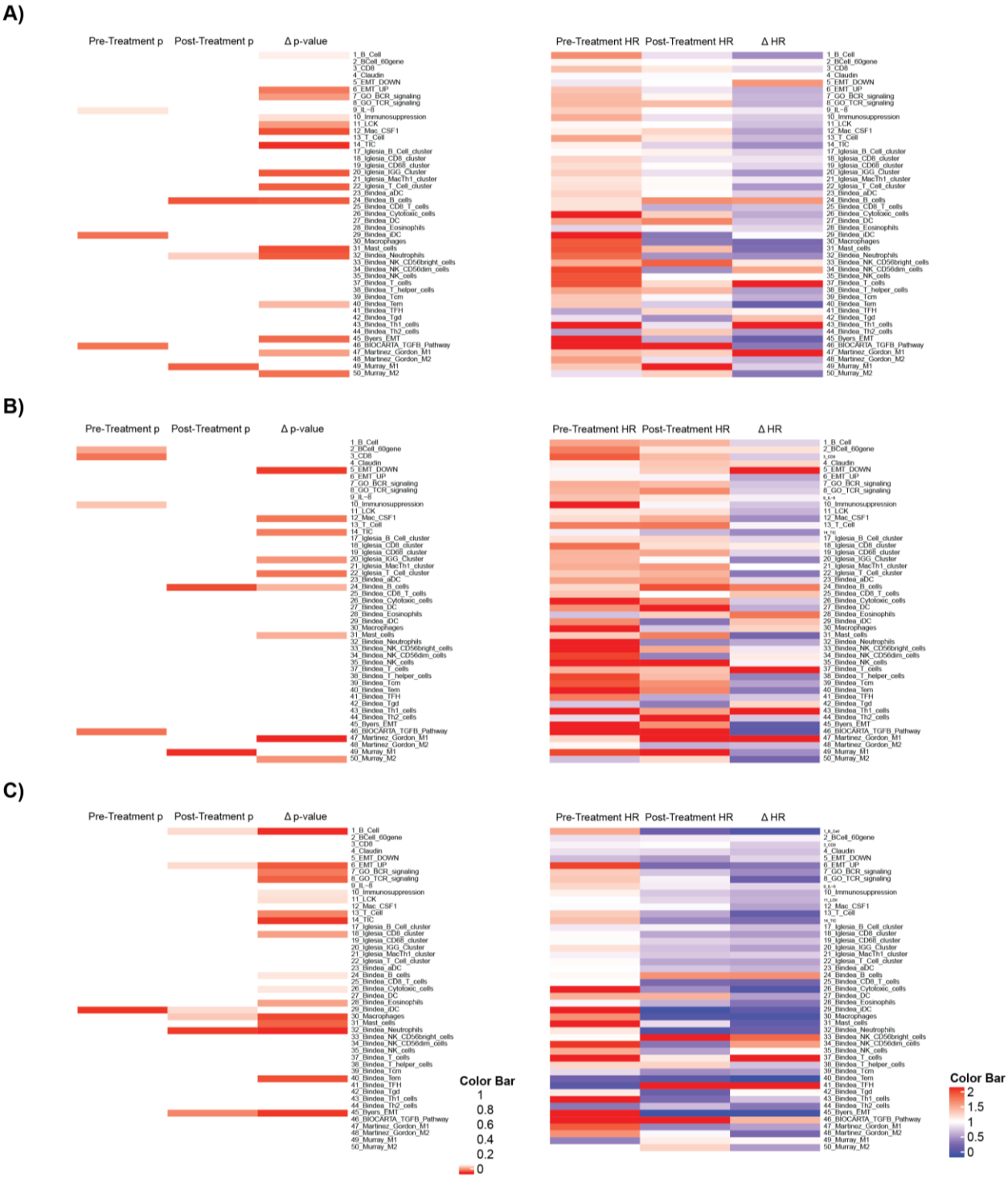

Figure 4.13: Change in gene signature expression is more predictive of survival than pre- or post-treatment expression levels. Heatmaps of significance (left) and hazard ratio (right) across all patients (A), GemCis treated patients (B), and MVAC treated patients (C) after accounting for tumor stage and grade.

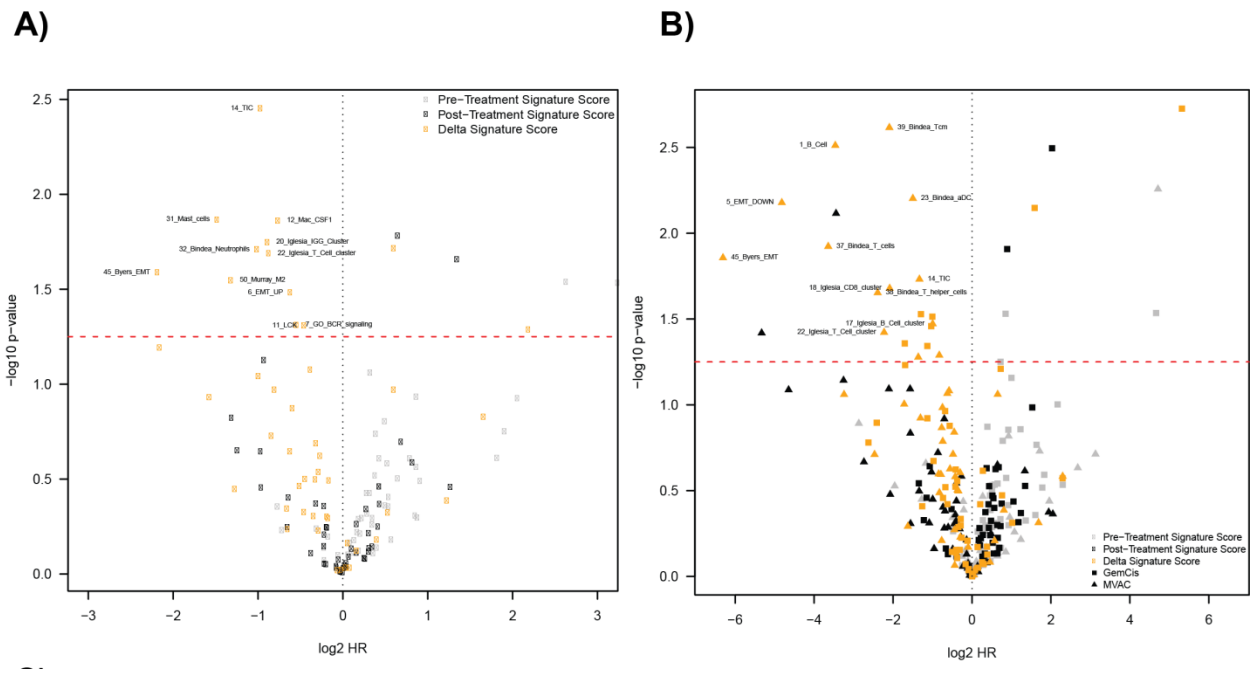

Figure 4.14: Change in immune gene signatures are predictive of survival in MVAC treated patients. Volcano plot of the hazard ratio and p-value of Cox-PH modeling of gene signature scores across all patients (A) and within GemCis/MVAC treated cohorts (B) after accounting for tumor stage and grade.

4.2.7 *In vitro* treatment with Methotrexate is sufficient to induce epithelial to mesenchymal transition in murine bladder cancer cell lines

Our lab has previously developed murine bladder cancer cell line models that accurately recapitulate the intrinsic molecular subtypes of bladder cancer (69). One of these cell lines is BBN963. To assess differences in the effect of MVAC and GemCis treatment on bladder cancer cells we treated a BBN963 cell line with concentrations of MVAC/GemCis and each of their individual component drugs for 72hr, and measured changes in cellular markers of EMT. We found that MVAC treatment induces a greater increase in Vimentin expression than GemCis treatment, and that Methotrexate treatment was sufficient to induce an increase in Vimentin expression (Figure 4.15A). Methotrexate is a dihydrofolate reductase inhibitor which is necessary for the synthesis

of tetrahydrofolate, a key precursor for purine and pyrimidine synthesis (98). We treated both BBN963 and UPPL1694 murine bladder cancer cell lines with a combination of methotrexate and leucovorin (the drug name for tetrahydrofolate). We found that across both cell lines, treatment with methotrexate increased Vimentin expression, and treatment with a combination of methotrexate and leucovorin restores lower levels of vimentin expression (Figure 4.15B). This supports the notion that the inhibition of dihydrofolate reductase by methotrexate is the driving mechanism of the induction of a mesenchymal phenotype and the corresponding increase in immune infiltration in MVAC-treated tumors.

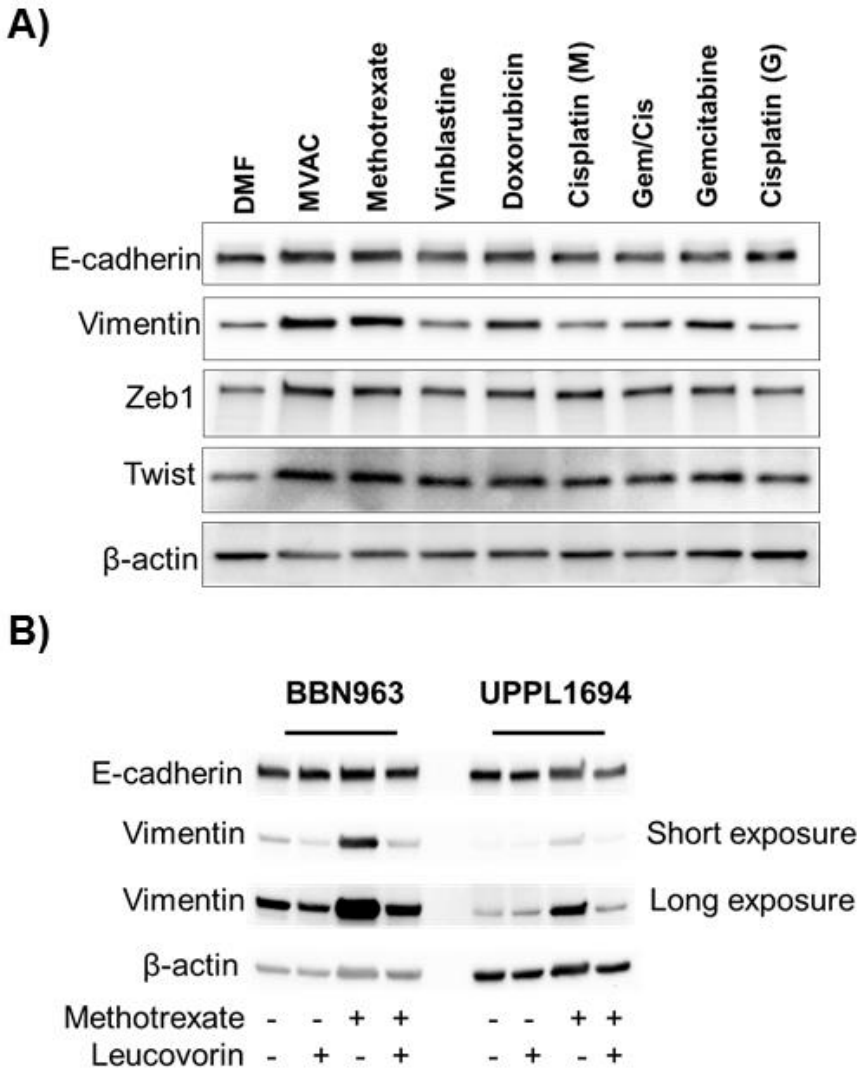

Figure 4.15: Methotrexate treatment is sufficient to induce a mesenchymal phenotype in murine bladder cancer cell lines. (A) Western blot of EMT markers after treatment with MVAC, GemCis, and the individual drug components in a BBN963 cell line. (B) Western blot of EMT markers after methotrexate/leucovorin treatment in BBN963 and UPL1694 cell lines.

4.2.8 *In vivo* treatment of murine bladder cancer models with MVAC/GemCis reveals differences in the effect on the tumor immune microenvironment

To assess the effects of MVAC and GemCis treatment on the immune microenvironment, we used previously developed murine models of bladder cancer (69). Bladder cell lines were subcutaneously injected in immune-competent B6 mice.

Once the tumor had reached a volume of 200mm^3, mice were enrolled in a treatment condition for 2 weeks, after which tumors were isolated and analyzed (Figure 4.16A). Both GemCis and MVAC treated tumors progressed slower and had smaller tumor endpoint volumes than saline treated mice (Figure 4.16B-C), indicating that we were dosing with biologically relevant concentrations of chemotherapeutic regimens.

Tumors were analyzed through a T-cell flow cytometry panel across treatment conditions. The percentage of CD8 effector memory T-cells was significantly higher in MVAC-treated cells compared with both GemCis and saline treated tumors across both cell lines (Figure 4.17A). Furthermore, MVAC treatment also induced significantly higher levels of the percentage of CD4 effector memory T-cells across both cell lines (Figure 4.17B). Interestingly, treatment with just methotrexate was sufficient to induce the same phenotype as the combination MVAC treatment (Figure 4.17A-B). This further supports that MVAC treatment preferentially induces an activated immune response in the bladder cancer microenvironment that is not activated in response to GemCis treatment.

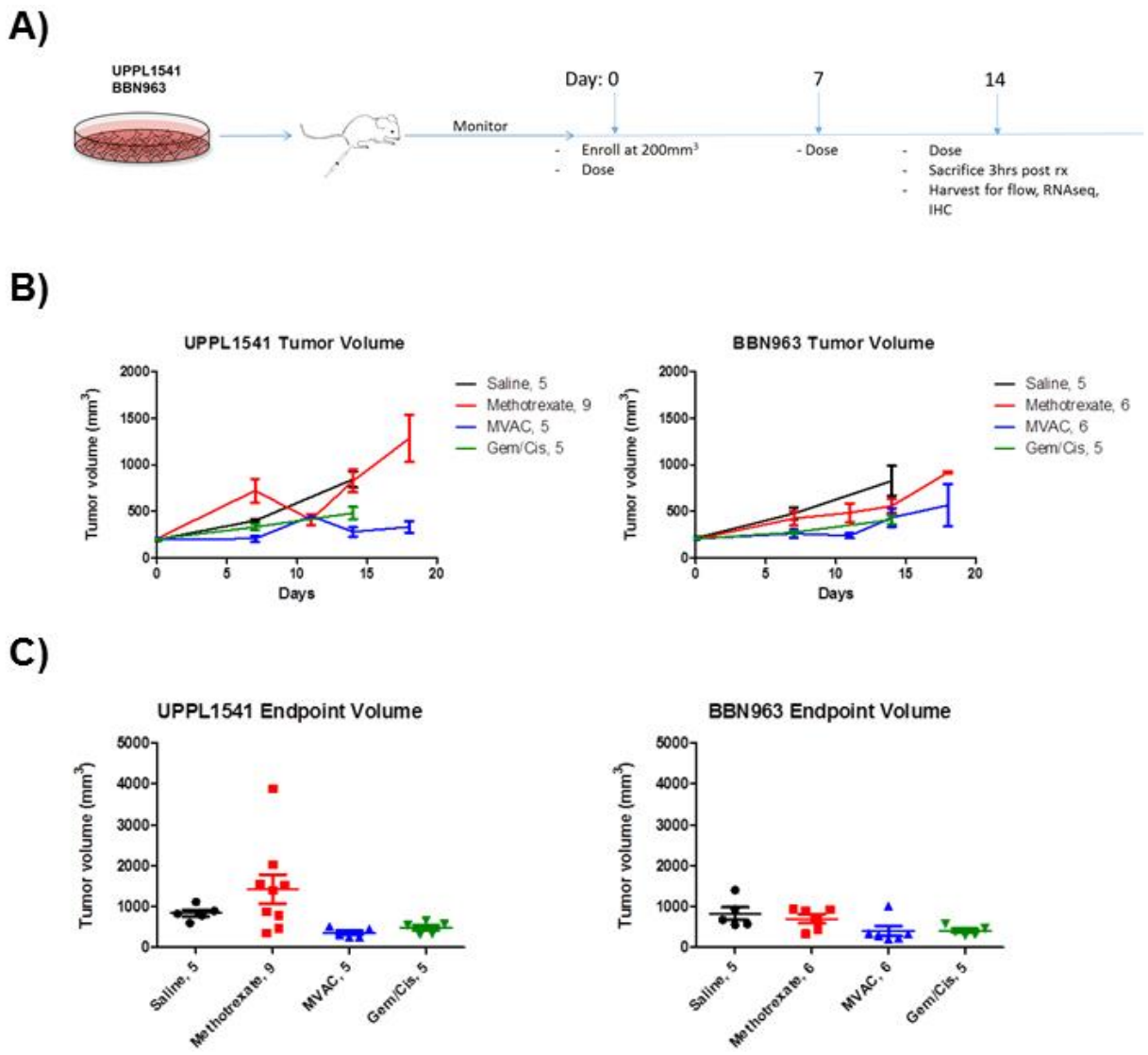

Figure 4.16: Treatment of murine bladder cancer models accurately recapitulate treatment of basal and luminal subtypes of bladder cancer. (A) A workflow of study design for treatment of murine bladder cancer models. (B) Plots of change in tumors volume after treatment start date of UPPL1541 (left) and BBN963 (right) tumors. (C) Plots of final tumor volume of UPPL1541 (left) and BBN963 (right) tumors.

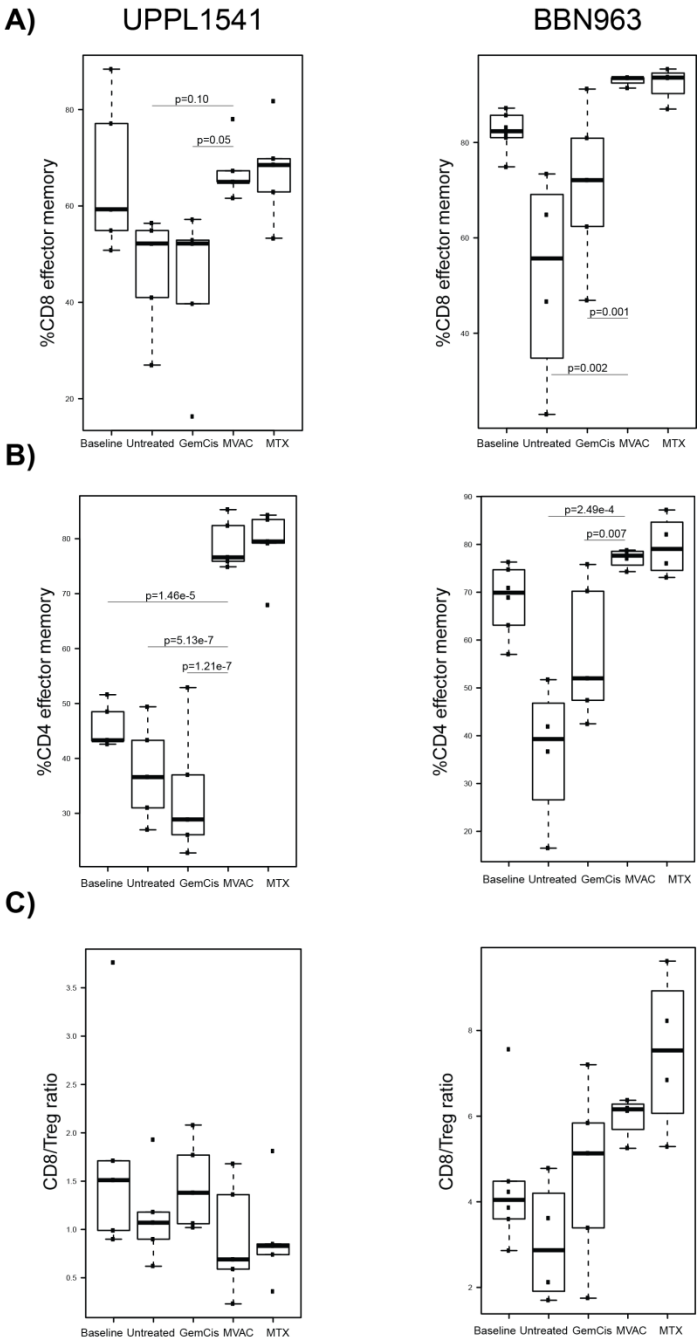

Figure 4.17: MVAC treatment has differential effect on the murine tumor immune microenvironment than GemCis treatment. Boxplots by treatment condition for percentage of CD8+ cytotoxic effector memory T-cells (A), percentage of CD4+ helper effector memory T-cells (B), and the overall CD8+ cytotoxic T-cell to regulatory t-cell ratio (C) within the tumor microenvironment.

4.3 Discussion

Here we describe the effects of cisplatin-based chemotherapy on the tumor microenvironment. We find that GemCis and MVAC treatment, the two main frontline chemotherapeutic regimens approved for the treatment of muscle invasive bladder cancer, have differing effects on the tumor microenvironment. MVAC treatment of luminal tumors in particular appears to induce significantly higher levels of immune infiltration and corresponding immune suppression than GemCis treatment. We further show that this effect appears to be induced by a misregulation of the cytokine production and EMT induction, and that methotrexate treatment alone, through its inhibition of dihydrofolate reductase, is sufficient to induce a mesenchymal and immune-infiltrated phenotype. In aggregate this work shows that while MVAC and GemCis have the same clinical response in patients with bladder cancer, they have differing effects on the tumor microenvironment that has important implications on how immune checkpoint therapy is combined or sequenced with chemotherapy.

This could have potential implications for patient care as response to immune checkpoint inhibition in bladder cancer has been shown to be correlated with immune suppression. Immune checkpoint inhibition is becoming more prevalent as a treatment for refractory tumors after frontline neoadjuvant chemotherapy and cystectomy treatment. As both MVAC and GemCis are approved as frontline treatments of bladder cancer we should explore the possibility of treating patients in a subtype-specific manner. Patients with basal tumors, who show no significant change in the immune microenvironment in response to MVAC treatment, could receive GemCis treatment. Patients with luminal tumors, in which immune infiltration is significantly increased with

MVAC treatment, could receive MVAC treatment to potentially prime them for follow-up immune checkpoint inhibition therapy if they do not respond to frontline chemotherapy.

Furthermore, we have found that the change in the immune microenvironment induced by MVAC appears to be mediated by methotrexate. Methotrexate inhibits dihydrofolate reductase, an enzyme that functions in nucleotide synthesis. Thus, methotrexate induces replicative stress within tumor cells, and the transition to a more mesenchymal and immune infiltrated phenotype appears to be in response to this stress. In line with this, previous studies have shown that inhibition of folate production is associated with EMT and oncogenesis across tumor types (99,100). Of note, a recent clinical trial of combination platinum-based chemotherapy plus pemetrexed, another dihydrofolate inhibitor, with follow-up immune checkpoint inhibition was shown to have significantly better patient response than chemotherapy alone, indicating that inhibition of folate synthesis can potentially be used to improve the efficacy of immune checkpoint inhibitors (101). The effects of other drugs and therapies on the tumor microenvironment that target this mechanism should be further explored.

Interestingly, we also found that the post-treatment change in several immune gene signatures between TURBT and RC samples is correlated with response to both GemCis and MVAC therapy. This could potentially better inform patient care by being able to predict at cystectomy whether a patient will respond to treatment, and if a patient will not respond they can more quickly be transitioned to secondary therapies. Additional exploration of incorporating both immune biomarkers and patient tumor subtyping into patient care should be considered.

4.4 Methods

4.4.1 Sample Data Processing and Sequencing

Patient sample clinical characteristics and RNA expression matrices were provided by collaborators at MD Anderson Cancer Center (70), Fox Chase Cancer Center (71), and GenomeDx Biosciences. The UNC cohort of tissue samples was collected from patients at UNC who underwent neoadjuvant gemcitabine and cisplatin chemotherapy followed by cystectomy between 2012 and 2017. Clinical information was annotated for all patients, including patient demographics (age, gender, race, and smoking status) and tumor stage and grade. All included patients had FFPE tissue available with adequate quality and amount. This study was reviewed and approved by the Institutional Review Board at UNC.

RNA was isolated from 10uM FFPE slides from all patient samples using the Roche High Pure RNA Paraffin Kit according to protocol. Isolated RNA was eluted in 50uL volume and tested using a Nanodrop One spectrophotometer to ensure it met both Nanodrop and our previous sequencing specifications for concentration (>15 ng/uL) and purity (OD 260/280 & 260/230 nm >1.6). For RNA sequencing, a minimum of 2 µg of total RNA was isolated from FFPE tissues. Extracted RNA was converted to double-stranded cDNA, and sequencing adapters were ligated by using the Illumina RNA Access Library Prep Protocol (Illumina). Samples were sequenced by paired-end, 150-bp sequencing on an Illumina NextSeq500 in the Kim Lab at UNC. Sequence reads were aligned to the human reference transcriptome, and gene expression was generated as reads per kilobase of exon model per million mapped reads per gene by using MapSplice. RNA sequencing data were normalized for variations in read counts,

and $\log_2$ transformed before analysis. When combining data sets, we adjusted for batch effects using the surrogate variable analysis R package (version 3.12.0; R Foundation, Vienna, Austria).

4.4.2 Gene Expression and Signature Analysis

Differential gene expression analysis was performed using SAMR analysis. Cellular pathway analysis across treatment conditions was performed using QIAGEN's IPA (www.qiagen.com/ingenuity). Comparison across conditions was done using the gene list with an FDR of 0.00 as determined by SAM analysis. Gene signatures were compiled from previously validated publications (32,34,52,67,69). Cytokines were identified using a RegEx search to capture all members of the molecular families. Signature scores were generated for gene signatures as previously described (74). All figures were generated using a locally designed script.

4.4.3 *In vitro* treatment analysis

BBN963 and UPPL1541 cell lines were cultured according to standard protocol. Cell lines were treated for 72 hours with either MVAC (Methotrexate 13.8nm, Vinblastine 0.8nm, Doxorubicin 11.9nm, Cisplatin 49.4nm) or GemCis (Gemcitabine 29.6nm, Cisplatin 1.9nm) regimens consistent with clinical dosing regimens. Cells were collected and a western blot was run according to standard laboratory protocol. Antibodies used were from Abcam.

4.4.4 *In vivo* treatment analysis

BBN963 and UPPL1541 cell lines were injected subcutaneously in C57BL/6J mice at 1e7 and 1.5e6 respectively. Once tumors reached 200mm^3 in tumor volume, treatment with either MVAC, GemCis, Methotrexate, or Saline began (Gemcitabine: 200 mpk. Resuspended with saline to 40 mg/mL day of dosing (ip qwk), Cisplatin: 3 mpk with Gemcitabine and 4 mpk in MVAC cocktail (stock @ 1mg/mL) (ip qwk), Methotrexate: 2 mpk in saline (ip qwk) (stock @ 25mg/mL → dilute to 0.5mg/mL), Vinblastine: 0.2 mpk in saline (ip qwk) (stock @ 1mg/mL), Adriamycin (aka Doxorubicin): 4 mpk in saline (ip qwk) (stock @ 2mg/mL)). Treatment was administered once per week and tumor size was measure accordingly. Tumors were taken down and tissue samples collected 3 hours after that last treatment on day 14.

4.4.5 Flow cytometry analysis

Tissues were homogenized in cold media using the GentleMACs Dissociator and the samples were passed through a 70 µM cell strainer, followed by homogenization using a 5 mL syringe plunger. The samples were centrifuged for 7 minutes at 1200 RPM, 4°C, decanting the supernatant. The remaining pellet was resuspended into 1 mL of ACK lysis buffer (150 mM NH_4Cl, 10 mM, $KHCO_3$, 0.1 nM Na_2EDTA in DPBS, pH 7.3) for 2 minutes at room temperature before quenching with 10 mL of cold media. The samples were centrifuged for 7 minutes at 1200 RPM, 4°C, resuspended in 10 mL of cold media, and passed through a 40 µM cell strainer. Cell counting was performed by running a diluted aliquot of sample on a MACSQuant flow cytometer, counting lymphocytes as gated by forward scatter area versus side scatter area.

Samples were washed and resuspended in cold DPBS, normalized by count, and transferred onto a 96 well V-bottom plate at 2.5 million lymphocytes per well. Cells were resuspended in FVS700 viability stain (BD, 1:1000 dilution in 100 µL DPBS) for 40 minutes on ice. Wells not receiving viability staining were resuspended in DPBS. Cells were washed twice in staining buffer (0.02% NaN_3, 2% BSA in DPBS), resuspended in 50 µL Fc block (1:50 dilution in staining buffer), and incubated on ice for 15 minutes. Antibody master mix was added to samples at 50 µL per sample with final antibody concentrations of (All mAbs from BD Biosciences):

T-cell panel: CD3e APC (1:100; 145-2C11), CD8a APC-H7 (1:100; 53-6.7), CD4 FITC (1:200; RM4-5), CD44 PerCP-Cy5.5 (1:200; IM7), CD62L BV421 (1:200; MEL-14), CD45 BV510(1:200;), FoxP3 PE (1:100;).

Cells were incubated on ice in the dark for 45 minutes and washed twice with staining buffer. Cells were fixed in 2% paraformaldehyde overnight. The following morning, a minimum of 100,000 events were collected for each sample on a BD LSRFortessa flow cytometer. FlowJo flow cytometry software Version 10 (Treestar) was used for analyses. Fluorescence Minus One (FMO) controls were used to guide gating strategies.

REFERENCES

1. Ferlay J, Soerjomataram I, Dikshit R, Eser S, Mathers C, Rebelo M, Parkin DM, Forman D, Bray F. Cancer incidence and mortality worldwide: sources, methods and major patterns in GLOBOCAN 2012. Int. J. Cancer. 2015 Mar 1;136(5):E359–86.

2. Siegel RL, Miller KD, Jemal A. Cancer statistics, 2016. CA Cancer J Clin. 3rd ed. 2016 Jan;66(1):7–30.

3. Maase von der H, Hansen SW, Roberts JT, Dogliotti L, Oliver T, Moore MJ, Bodrogi I, Albers P, Knuth A, Lippert CM, Kerbrat P, Sanchez Rovira P, Wersall P, Cleall SP, Roychowdhury DF, Tomlin I, Visseren-Grul CM, Conte PF. Gemcitabine and cisplatin versus methotrexate, vinblastine, doxorubicin, and cisplatin in advanced or metastatic bladder cancer: results of a large, randomized, multinational, multicenter, phase III study. J. Clin. Oncol. 2000 Sep;18(17):3068–77.

4. Sjödahl G, Lauss M, Lövgren K, Chebil G, Gudjonsson S, Veerla S, Patschan O, Aine M, Fernö M, Ringnér M, Månsson W, Liedberg F, Lindgren D, Höglund M. A molecular taxonomy for urothelial carcinoma. Clin. Cancer Res. 2012 Jun 15;18(12):3377–86.

5. Choi W, Porten S, Kim S, Willis D, Plimack ER, Hoffman-Censits J, Roth B, Cheng T, Tran M, Lee I-L, Melquist J, Bondaruk J, Majewski T, Zhang S, Pretzsch S, Baggerly K, Siefker-Radtke A, Czerniak B, Dinney CPN, McConkey DJ. Identification of distinct basal and luminal subtypes of muscle-invasive bladder cancer with different sensitivities to frontline chemotherapy. Cancer Cell. 2014 Feb 10;25(2):152–65. PMCID: PMC4011497

6. Damrauer JS, Hoadley KA, Chism DD, Fan C, Tiganelli CJ, Wobker SE, Yeh JJ, Milowsky MI, Iyer G, Parker JS, Kim WY. Intrinsic subtypes of high-grade bladder cancer reflect the hallmarks of breast cancer biology. Proceedings of the National Academy of Sciences. 2014 Feb 25;111(8):3110–5. PMCID: PMC3939870

7. Robertson AG, Kim J, Al-Ahmadie H, Bellmunt J, Guo G, Cherniack AD, Hinoue T, Laird PW, Hoadley KA, Akbani R, Castro MAA, Gibb EA, Kanchi RS, Gordenin DA, Shukla SA, Sanchez-Vega F, Hansel DE, Czerniak BA, Reuter VE, Su X, de Sa Carvalho B, Chagas VS, Mungall KL, Sadeghi S, Pedamallu CS, Lu Y, Klimczak LJ, Zhang J, Choo C, Ojesina AI, Bullman S, Leraas KM, Lichtenberg TM, Wu CJ, Schultz N, Getz G, Meyerson M, Mills GB, McConkey DJ, TCGA Research Network, Weinstein JN, Kwiatkowski DJ, Lerner SP. Comprehensive Molecular Characterization of Muscle-Invasive Bladder Cancer. Cell. 2017 Oct 19;171(3):540–556.e25.

8. Cancer Genome Atlas Research Network. Comprehensive molecular characterization of urothelial bladder carcinoma. Nature. 2014 Mar 20;507(7492):315–22. PMCID: PMC3962515

9. Yadav M, Jhunjhunwala S, Phung QT, Lupardus P, Tanguay J, Bumbaca S, Franci C, Cheung TK, Fritsche J, Weinschenk T, Modrusan Z, Mellman I, Lill JR, Delamarre L. Predicting immunogenic tumour mutations by combining mass spectrometry and exome sequencing. Nature. Nature Publishing Group; 2014 Nov 27;515(7528):572–6.

10. Tran E, Turcotte S, Gros A, Robbins PF, Lu YC, Dudley ME, Wunderlich JR, Somerville RP, Hogan K, Hinrichs CS, Parkhurst MR, Yang JC, Rosenberg SA. Cancer Immunotherapy Based on Mutation-Specific CD4+ T Cells in a Patient with Epithelial Cancer. Science. 2014 May 8;344(6184):641–5.

11. Ott PA, Hu Z, Keskin DB, Shukla SA, Sun J, Bozym DJ, Zhang W, Luoma A, Giobbie-Hurder A, Peter L, Chen C, Olive O, Carter TA, Li S, Lieb DJ, Eisenhaure T, Gjini E, Stevens J, Lane WJ, Javeri I, Nellaiappan K, Salazar AM, Daley H, Seaman M, Buchbinder EI, Yoon CH, Harden M, Lennon N, Gabriel S, Rodig SJ, Barouch DH, Aster JC, Getz G, Wucherpfennig K, Neuberg D, Ritz J, Lander ES, Fritsch EF, Hacohen N, Wu CJ. An immunogenic personal neoantigen vaccine for patients with melanoma. Nature. Nature Research; 2017 Jul 5;348:69.

12. Carreno BM, Magrini V, Becker-Hapak M, Kaabinejadian S, Hundal J, Petti AA, Ly A, Lie WR, Hildebrand WH, Mardis ER, Linette GP. A dendritic cell vaccine increases the breadth and diversity of melanoma neoantigen-specific T cells. Science. 2015 May 14;348(6236):803–8.

13. Sahin U, Derhovanessian E, Miller M, Kloke B-P, Simon P, Löwer M, Bukur V, Tadmor AD, Luxemburger U, Schrörs B, Omokoko T, Vormehr M, Albrecht C, Paruzynski A, Kuhn AN, Buck J, Heesch S, Schreeb KH, Müller F, Ortseifer I, Vogler I, Godehardt E, Attig S, Rae R, Breitkreuz A, Tolliver C, Suchan M, Martic G, Hohberger A, Sorn P, Diekmann J, Ciesla J, Waksmann O, Brück A-K, Witt M, Zillgen M, Rothermel A, Kasemann B, Langer D, Bolte S, Diken M, Kreiter S, Nemecek R, Gebhardt C, Grabbe S, Höller C, Utikal J, Huber C, Loquai C, Türeci Ö. Personalized RNA mutanome vaccines mobilize poly-specific therapeutic immunity against cancer. Nature. 2017 Jul 13;547(7662):222–6.

14. Rosenberg JE, Hoffman-Censits J, Powles T, van der Heijden MS, Balar AV, Necchi A, Dawson N, O'Donnell PH, Balmanoukian A, Loriot Y, Srinivas S, Retz MM, Grivas P, Joseph RW, Galsky MD, Fleming MT, Petrylak DP, Perez-Gracia JL, Burris HA, Castellano D, Canil C, Bellmunt J, Bajorin D, Nickles D, Bourgon R, Frampton GM, Cui N, Mariathasan S, Abidoye O, Fine GD, Dreicer R. Atezolizumab in patients with locally advanced and metastatic urothelial carcinoma who have progressed following treatment with platinum-based chemotherapy: a single-arm, multicentre, phase 2 trial. Lancet. 2016 Mar 4.

15. Snyder A, Nathanson T, Funt SA, Ahuja A, Buros Novik J, Hellmann MD, Chang E, Aksoy BA, Al-Ahmadie H, Yusko E, Vignali M, Benzeno S, Boyd M, Moran M, Iyer G, Robins HS, Mardis ER, Merghoub T, Hammerbacher J, Rosenberg JE, Bajorin DF. Contribution of systemic and somatic factors to clinical response and resistance to PD-L1 blockade in urothelial cancer: An exploratory multi-omic analysis. Minna JD, editor. Plos Med. 2017 May;14(5):e1002309.

16. Miao D, Margolis CA, Gao W, Voss MH, Li W, Martini DJ, Norton C, Bossé D, Wankowicz SM, Cullen D, Horak C, Wind-Rotolo M, Tracy A, Giannakis M, Hodi FS, Drake CG, Ball MW, Allaf ME, Snyder A, Hellmann MD, Ho T, Motzer RJ, Signoretti S, Kaelin WG, Choueiri TK, Van Allen EM. Genomic correlates of response to immune checkpoint therapies in clear cell renal cell carcinoma. Science. American Association for the Advancement of Science; 2018 Jan 4;:eaan5951.

17. Mariathasan S, Turley SJ, Nickles D, Castiglioni A, Yuen K, Wang Y, Kadel EE III, Koeppen H, Astarita JL, Cubas R, Jhunjhunwala S, Banchereau R, Yang Y, Guan Y, Chalouni C, Ziai J, Şenbabaoğlu Y, Santoro S, Sheinson D, Hung J, Giltnane JM, Pierce AA, Mesh K, Lianoglou S, Riegler J, Carano RAD, Eriksson P, Höglund M, Somarriba L, Halligan DL, van der Heijden MS, Loriot Y, Rosenberg JE, Fong L, Mellman I, Chen DS, Green M, Derleth C, Fine GD, Hegde PS, Bourgon R, Powles T. TGFβ attenuates tumour response to PD-L1 blockade by contributing to exclusion of T cells. Nature. Nature Publishing Group; 2018 Feb 14;515(7693):563–548.

18. Snyder A, Makarov V, Merghoub T, Yuan J, Zaretsky JM, Desrichard A, Walsh LA, Postow MA, Wong P, Ho TS, Hollmann TJ, Bruggeman C, Kannan K, Li Y, Elipenahli C, Liu C, Harbison CT, Wang L, Ribas A, Wolchok JD, Chan TA. Genetic Basis for Clinical Response to CTLA-4 Blockade in Melanoma. N Engl J Med. 2014 Nov 19;:141121104951001.

19. Gao J, Shi LZ, Zhao H, Chen J, Xiong L, He Q, Chen T, Roszik J, Bernatchez C, Woodman SE, Chen P-L, Hwu P, Allison JP, Futreal A, Wargo JA, Sharma P. Loss of IFN-γ Pathway Genes in Tumor Cells as a Mechanism of Resistance to Anti-CTLA-4 Therapy. Cell. 2016 Oct 6;167(2):397–9. PMCID: PMC5088716

20. Rizvi NA, Hellmann MD, Snyder A, Kvistborg P, Makarov V, Havel JJ, Lee W, Yuan J, Wong P, Ho TS, Miller ML, Rekhtman N, Moreira AL, Ibrahim F, Bruggeman C, Gasmi B, Zappasodi R, Maeda Y, Sander C, Garon EB, Merghoub T, Wolchok JD, Schumacher TN, Chan TA. Cancer immunology. Mutational landscape determines sensitivity to PD-1 blockade in non-small cell lung cancer. Science. American Association for the Advancement of Science; 2015 Apr 3;348(6230):124–8.

21. Goebell PJ, Knowles MA. Bladder cancer or bladder cancers? Genetically distinct malignant conditions of the urothelium. Urol. Oncol. 2010 Jul;28(4):409–28.

22. Rebouissou S, Bernard-Pierrot I, de Reyniès A, Lepage M-L, Krucker C, Chapeaublanc E, Hérault A, Kamoun A, Caillault A, Letouzé E, Elarouci N, Neuzillet Y, Denoux Y, Molinié V, Vordos D, Laplanche A, Maillé P, Soyeux P, Ofualuka K, Reyal F, Biton A, Sibony M, Paoletti X, Southgate J, Benhamou S, Lebret T, Allory Y, Radvanyi F. EGFR as a potential therapeutic target for a subset of muscle-invasive bladder cancers presenting a basal-like phenotype. Science Translational Medicine. 2014 Jul 9;6(244):244ra91–1.

23. Dyrskjøt L, Thykjaer T, Kruhøffer M, Jensen JL, Marcussen N, Hamilton-Dutoit S, Wolf H, Ørntoft TF. Identifying distinct classes of bladder carcinoma using microarrays. Nat Genet. 2003 Jan;33(1):90–6.

24. Volkmer J-P, Sahoo D, Chin RK, Ho PL, Tang C, Kurtova AV, Willingham SB, Pazhanisamy SK, Contreras-Trujillo H, Storm TA, Lotan Y, Beck AH, Chung BI, Alizadeh AA, Godoy G, Lerner SP, van de Rijn M, Shortliffe LD, Weissman IL, Chan KS. Three differentiation states risk-stratify bladder cancer into distinct subtypes. Proc. Natl. Acad. Sci. U.S.A. 2012 Feb 7;109(6):2078–83. PMCID: PMC3277552

25. Prat A, Karginova O, Parker JS, Fan C, He X, Bixby L, Harrell JC, Roman E, Adamo B, Troester M, Perou CM. Characterization of cell lines derived from breast cancers and normal mammary tissues for the study of the intrinsic molecular subtypes. Breast Cancer Res Treat. 2013 Nov;142(2):237–55. PMCID: PMC3832776

26. Massard C, Gordon MS, Sharma S, Rafii S, Wainberg ZA, Luke J, Curiel TJ, Colon-Otero G, Hamid O, Sanborn RE, O'Donnell PH, Drakaki A, Tan W, Kurland JF, Rebelatto MC, Jin X, Blake-Haskins JA, Gupta A, Segal NH. Safety and Efficacy of Durvalumab (MEDI4736), an Anti-Programmed Cell Death Ligand-1 Immune Checkpoint Inhibitor, in Patients With Advanced Urothelial Bladder Cancer. Journal of Clinical Oncology. 2016 Sep 10;34(26):3119–25.

27. Apolo AB, Infante JR, Balmanoukian A, Patel MR, Wang D, Kelly K, Mega AE, Britten CD, Ravaud A, Mita AC, Safran H, Stinchcombe TE, Srdanov M, Gelb AB, Schlichting M, Chin K, Gulley JL. Avelumab, an Anti-Programmed Death-Ligand 1 Antibody, In Patients With Refractory Metastatic Urothelial Carcinoma: Results From a Multicenter, Phase Ib Study. Journal of Clinical Oncology. 2017 Apr 4;:JCO2016716795.

28. Sharma P, Shen Y, WEN S, Yamada S, Jungbluth AA, Gnjatic S, Bajorin DF, Reuter VE, Herr H, Old LJ, Sato E. CD8 tumor-infiltrating lymphocytes are predictive of survival in muscle-invasive urothelial carcinoma. Proc. Natl. Acad. Sci. U.S.A. National Acad Sciences; 2007 Mar 6;104(10):3967–72. PMCID: PMC1820692

29. Bellmunt J, de Wit R, Vaughn DJ, Fradet Y, Lee J-L, Fong L, Vogelzang NJ, Climent MA, Petrylak DP, Choueiri TK, Necchi A, Gerritsen W, Gurney H, Quinn

DI, Culine S, Sternberg CN, Mai Y, Poehlein CH, Perini RF, Bajorin DF. Pembrolizumab as Second-Line Therapy for Advanced Urothelial Carcinoma. http://dx.doi.org/10.1056/NEJMoa1613683. Massachusetts Medical Society; 2017 Feb 17;:NEJMoa1613683.

30. Powles T, Eder JP, Fine GD, Braiteh FS, Loriot Y, Cruz C, Bellmunt J, Burris HA, Petrylak DP, Teng S-L, Shen X, Boyd Z, Hegde PS, Chen DS, Vogelzang NJ. MPDL3280A (anti-PD-L1) treatment leads to clinical activity in metastatic bladder cancer. Nature. 2014 Nov 27;515(7528):558–62.

31. Prat A, Parker JS, Karginova O, Fan C, Livasy C, Herschkowitz JI, He X, Perou CM. Phenotypic and molecular characterization of the claudin-low intrinsic subtype of breast cancer. Breast Cancer Res. 2010;12(5):R68. PMCID: PMC3096954

32. Chan KS, Espinosa I, Chao M, Wong D, Ailles L, Diehn M, Gill H, Presti J, Chang HY, van de Rijn M, Shortliffe L, Weissman IL. Identification, molecular characterization, clinical prognosis, and therapeutic targeting of human bladder tumor-initiating cells. Proc. Natl. Acad. Sci. U.S.A. 2009 Aug 18;106(33):14016–21. PMCID: PMC2720852

33. Choi W, Czerniak B, Ochoa A, Su X, Siefker-Radtke A, Dinney C, McConkey DJ. Intrinsic basal and luminal subtypes of muscle-invasive bladder cancer. Nat Rev Urol. 2014 Jul;11(7):400–10.

34. Iglesia MD, Vincent BG, Parker JS, Hoadley KA, Carey LA, Perou CM, Serody JS. Prognostic B-cell signatures using mRNA-seq in patients with subtype-specific breast and ovarian cancer. Clin. Cancer Res. American Association for Cancer Research; 2014 Jul 15;20(14):3818–29. PMCID: PMC4102637

35. Fridman WH, Galon J, Dieu-Nosjean M-C, Cremer I, Fisson S, Damotte D, Pagès F, Tartour E, Sautès-Fridman C. Immune infiltration in human cancer: prognostic significance and disease control. Curr. Top. Microbiol. Immunol. Berlin, Heidelberg: Springer Berlin Heidelberg; 2011;344(Chapter 46):1–24.

36. Horn T, Laus J, Seitz AK, Maurer T, Schmid SC, Wolf P, Haller B, Winkler M, Retz M, Nawroth R, Gschwend JE, Kübler HR, Slotta-Huspenina J. The prognostic effect of tumour-infiltrating lymphocytic subpopulations in bladder cancer. World J Urol. 2015 Jun 9;34(2):181–7.

37. Tumeh PC, Harview CL, Yearley JH, Shintaku IP, Taylor EJM, Robert L, Spasic M, Henry G, Ciobanu V, West AN, Carmona M, Kivork C, Seja E, Cherry G, Gutierrez AJ, Grogan TR, Mateus C, Tomasic G, Glaspy JA, Emerson RO, Robins H, Pierce RH, Elashoff DA, Ribas A. PD-1 blockade induces responses by inhibiting adaptive immune resistance. Nature. Nature Publishing Group; 2014 Nov 27;515(7528):568–71. PMCID: PMC4246418

38. Choudhury NJ, Kiyotani K, Yap KL, Campanile A, Antic T, Yew PY, Steinberg G, Park JH, Nakamura Y, O'Donnell PH. Low T-cell Receptor Diversity, High Somatic Mutation Burden, and High Neoantigen Load as Predictors of Clinical Outcome in Muscle-invasive Bladder Cancer. European Urology Focus. European Association of Urology; 2015 Oct 7;:1–8.

39. Schumacher TN, Schreiber RD. Neoantigens in cancer immunotherapy. Science. American Association for the Advancement of Science; 2015 Apr 3;348(6230):69–74.

40. Snook AE, Magee MS, Schulz S, Waldman SA. Selective antigen-specific CD4(+) T-cell, but not CD8(+) T- or B-cell, tolerance corrupts cancer immunotherapy. Eur. J. Immunol. 2014 Jul;44(7):1956–66. PMCID: PMC4107120

41. Brown SD, Warren RL, Gibb EA, Martin SD, Spinelli JJ, Nelson BH, Holt RA. Neo-antigens predicted by tumor genome meta-analysis correlate with increased patient survival. Genome Research. 2014 May;24(5):743–50. PMCID: PMC4009604

42. Van Allen EM, Miao D, Schilling B, Shukla SA, Blank C, Zimmer L, Sucker A, Hillen U, Foppen MHG, Goldinger SM, Utikal J, Hassel JC, Weide B, Kaehler KC, Loquai C, Mohr P, Gutzmer R, Dummer R, Gabriel S, Wu CJ, Schadendorf D, Garraway LA. Genomic correlates of response to CTLA-4 blockade in metastatic melanoma. Science. 2015 Oct 9;350(6257):207–11.

43. Rajasagi M, Shukla SA, Fritsch EF, Keskin DB, DeLuca D, Carmona E, Zhang W, Sougnez C, Cibulskis K, Sidney J, Stevenson K, Ritz J, Neuberg D, Brusic V, Gabriel S, Lander ES, Getz G, Hacohen N, Wu CJ. Systematic identification of personal tumor-specific neoantigens in chronic lymphocytic leukemia. Blood. American Society of Hematology; 2014 Jul 17;124(3):453–62. PMCID: PMC4102716

44. Choi N, Zhang B, Zhang L, Ittmann M, Xin L. Adult murine prostate basal and luminal cells are self-sustained lineages that can both serve as targets for prostate cancer initiation. Cancer Cell. 2012 Feb 14;21(2):253–65. PMCID: PMC3285423

45. Peters JM, Shah YM, Gonzalez FJ. The role of peroxisomeproliferator-activated receptors incarcinogenesis and chemoprevention. Nat Rev Cancer. Nature Publishing Group; 2012 Feb 9;12(3):181–95.

46. Chen L, Gibbons DL, Goswami S, Cortez MA, Ahn Y-H, Byers LA, Zhang X, Yi X, Dwyer D, Lin W, Diao L, Wang J, Roybal JD, Patel M, Ungewiss C, Peng D, Antonia S, Mediavilla-Varela M, Robertson G, Jones S, Suraokar M, Welsh JW, Erez B, Wistuba II, Chen L, Di Peng, Wang S, Ullrich SE, Heymach JV, Kurie JM, Qin FX-F. Metastasis is regulated via microRNA-200/ZEB1 axis control of tumour cell PD-L1 expression and intratumoral immunosuppression. Nat Commun. Nature Publishing Group; 2014 Oct 28;5:5241.

47. Mak M, Tong P, Diao L, Cardnell RJ, Gibbons DL, William WN, Skoulidis F, Parra ER, Rodriguez-Canales J, Wistuba II, Heymach JV, Weinstein JN, Coombes KR, Wang J, Byers LA. A patient-derived, pan-cancer EMT signature identifies global molecular alterations and immune target enrichment following epithelial to mesenchymal transition. Clin. Cancer Res. 2015 Sep 29.

48. Peters JM, Shah YM, Gonzalez FJ. The role of peroxisome proliferator-activated receptors in carcinogenesis and chemoprevention. Nat Rev Cancer. 2012 Feb 9;12(3):181–95. PMCID: PMC3322353

49. Rooney MS, Shukla SA, Wu CJ, Getz G, Hacohen N. Molecular and Genetic Properties of Tumors Associated with Local Immune Cytolytic Activity. Cell. Elsevier; 2015 Jan;160(1):48–61.

50. Korpal M, Puyang X, Wu ZJ, Seiler R, Furman C, Oo HZ, Seiler M, Irwin S, Subramanian V, Joshi JJ, Wang CK, Rimkunas V, Tortora D, Yang H, Kumar N, Kuznetsov G, Matijevic M, Chow J, Kumar P, Zou J, Feala J, Corson L, Henry R, Selvaraj A, Davis A, Bloudoff K, Douglas J, Kiss B, Roberts M, Fazli L, Black PC, Fekkes P, Smith PG, Warmuth M, Yu L, Hao M-H, Larsen N, Daugaard M, Zhu P. Evasion of immunosurveillance by genomic alterations of PPARγ/RXRα in bladder cancer. Nat Commun. Nature Publishing Group; 2017 Jul 24;8(1):103.

51. Hoadley KA, Yau C, Wolf DM, Cherniack AD, Tamborero D, Ng S, Leiserson MDM, Niu B, McLellan MD, Uzunangelov V, Zhang J, Kandoth C, Akbani R, Shen H, Omberg L, Chu A, Margolin AA, van't Veer LJ, López-Bigas N, Laird PW, Raphael BJ, Ding L, Robertson AG, Byers LA, Mills GB, Weinstein JN, Van Waes C, Chen Z, Collisson EA, Cancer Genome Atlas Research Network, Benz CC, Perou CM, Stuart JM. Multiplatform analysis of 12 cancer types reveals molecular classification within and across tissues of origin. Cell. 2014 Aug 14;158(4):929–44. PMCID: PMC4152462

52. Subramanian A, Tamayo P, Mootha VK, Mukherjee S, Ebert BL, Gillette MA, Paulovich A, Pomeroy SL, Golub TR, Lander ES, Mesirov JP. Gene set enrichment analysis: a knowledge-based approach for interpreting genome-wide expression profiles. Proc. Natl. Acad. Sci. U.S.A. 2005 Oct 25;102(43):15545–50. PMCID: PMC1239896

53. Cancer Genome Atlas Research Network. Comprehensive genomic characterization of squamous cell lung cancers. Nature. 2012 Sep 27;489(7417):519–25. PMCID: PMC3466113

54. Bai Y, Ni M, Cooper B, Wei Y, Fury W. Inference of high resolution HLA types using genome-wide RNA or DNA sequencing reads. BMC Genomics. BioMed Central Ltd; 2014 May 1;15(1):325. PMCID: PMC4035057

55. Gopalan A, Sharp DS, Fine SW, Tickoo SK, Herr HW, Reuter VE, Olgac S. Urachal Carcinoma. Am. J. Surg. Pathol. 2009 May;33(5):659–68.

56. Siefker-Radtke A. Urachal adenocarcinoma: a clinician's guide for treatment. Seminars in Oncology. 2012 Oct;39(5):619–24.

57. Wright JL, Porter MP, Li CI, Lange PH, Lin DW. Differences in survival among patients with urachal and nonurachal adenocarcinomas of the bladder. 2006 Aug 15;107(4):721–8.

58. Sirintrapun SJ, Ward M, Woo J, Cimic A. High-stage urachal adenocarcinoma can be associated with microsatellite instability and KRAS mutations. Hum. Pathol. 2014 Feb;45(2):327–30.

59. Singh H, Liu Y, Xiao X, Lin L, Kim J, Van Hummelen P, Wu C-L, Bass AJ, Saylor PJ. Whole exome sequencing of urachal adenocarcinoma reveals recurrent NF1 mutations. Oncotarget. 2016 Apr 7.

60. Collazo-Lorduy A, Castillo-Martin M, Wang L, Patel V, Iyer G, Jordan E, Al-Ahmadie H, Leonard I, Oh WK, Zhu J, McBride RB, Cordon-Cardo C, Solit DB, Sfakianos JP, Galsky MD. Urachal Carcinoma Shares Genomic Alterations with Colorectal Carcinoma and May Respond to Epidermal Growth Factor Inhibition. European Urology. 2016 May 10.

61. Cancer Genome Atlas Network. Comprehensive molecular characterization of human colon and rectal cancer. Nature. 2012 Jul 19;487(7407):330–7. PMCID: PMC3401966

62. Grabiner BC, Nardi V, Birsoy K, Possemato R, Shen K, Sinha S, Jordan A, Beck AH, Sabatini DM. A Diverse Array of Cancer-Associated MTOR Mutations Are Hyperactivating and Can Predict Rapamycin Sensitivity. Cancer Discovery. American Association for Cancer Research; 2014 May 1;4(5):554–63. PMCID: PMC4012430

63. Mermel CH, Schumacher SE, Hill B, Meyerson ML, Beroukhim R, Getz G. GISTIC2.0 facilitates sensitive and confident localization of the targets of focal somatic copy-number alteration in human cancers. Genome Biol. 2011;12(4):R41. PMCID: PMC3218867

64. Dudley JC, Lin M-T, Le DT, Eshleman JR. Microsatellite Instability as a Biomarker for PD-1 Blockade. Clin. Cancer Res. American Association for Cancer Research; 2016 Feb 15;22(4):813–20.

65. Rayner E, van Gool IC, Palles C, Kearsey SE, Bosse T, Tomlinson I, Church DN. A panoply of errors: polymerase proofreading domain mutations in cancer. Nat Rev Cancer. Nature Publishing Group; 2016 Feb 1;16(2):71–81.

66. Le DT, Uram JN, Wang H, Bartlett BR, Kemberling H, Eyring AD, Skora AD, Luber BS, Azad NS, Laheru D, Biedrzycki B, Donehower RC, Zaheer A, Fisher GA, Crocenzi TS, Lee JJ, Duffy SM, Goldberg RM, la Chapelle de A, Koshiji M, Bhaijee F, Huebner T, Hruban RH, Wood LD, Cuka N, Pardoll DM, Papadopoulos

N, Kinzler KW, Zhou S, Cornish TC, Taube JM, Anders RA, Eshleman JR, Vogelstein B, Diaz LA. PD-1 Blockade in Tumors with Mismatch-Repair Deficiency. N Engl J Med. 2015 Jun 25;372(26):2509–20. PMCID: PMC4481136

67. Kardos J, Chai S. Claudin-low bladder tumors are immune infiltrated and actively immune suppressed. 2016 Feb p. 1–41.

68. Verhaak RGW, Hoadley KA, Purdom E, Wang V, Qi Y, Wilkerson MD, Miller CR, Ding L, Golub T, Mesirov JP, Alexe G, Lawrence M, Kelly MO, Tamayo P, Weir BA, Gabriel S, Winckler W, Gupta S, Jakkula L, Feiler HS, Hodgson JG, James CD, Sarkaria JN, Brennan C, Kahn A, Spellman PT, Wilson RK, Speed TP, Gray JW, Meyerson M, Getz G, Perou CM, Hayes DN, Network TCGAR. Integrated Genomic Analysis Identifies Clinically Relevant Subtypes of Glioblastoma Characterized by Abnormalities in PDGFRA, IDH1, EGFR, and NF1. Cancer Cell. Elsevier Ltd; 2010 Jan 19;17(1):98–110.

69. Saito R, Smith CC, Utsumi T, Bixby LM, Kardos J, Wobker SE, Stewart KG, Chai S, Manocha U, Byrd KM, Damrauer JS, Williams SE, Vincent BG, Kim WY. Molecular subtype-specific immunocompetent models of high-grade urothelial carcinoma reveal differential neoantigen expression and response to immunotherapy. Cancer Research. 2018 May 21;:canres.0173.2018.

70. McConkey DJ, Choi W, Shen Y, Lee I-L, Porten S, Matin SF, Kamat AM, Corn P, MILLIKAN RE, Dinney C, Czerniak B, SIEFKER-RADTKE AO. A Prognostic Gene Expression Signature in the Molecular Classification of Chemotherapy-naïve Urothelial Cancer is Predictive of Clinical Outcomes f... - PubMed - NCBI. European Urology. 2016 May;69(5):855–62. PMCID: PMC4775435

71. Plimack ER, Hoffman-Censits JH, Viterbo R, Trabulsi EJ, Ross EA, Greenberg RE, Chen DYT, Lallas CD, Wong Y-N, Lin J, Kutikov A, Dotan E, Brennan TA, Palma N, Dulaimi E, Mehrazin R, Boorjian SA, Kelly WK, Uzzo RG, Hudes GR. Accelerated methotrexate, vinblastine, doxorubicin, and cisplatin is safe, effective, and efficient neoadjuvant treatment for muscle-invasive bladder cancer: results of a multicenter phase II study with molecular correlates of response and toxicity. Journal of Clinical Oncology. American Society of Clinical Oncology; 2014 Jun 20;32(18):1895–901. PMCID: PMC4050203

72. Liu D, Abbosh P, Keliher D, Reardon B, Miao D, Mouw K, Weiner-Taylor A, Wankowicz S, Han G, Teo MY, Cipolla C, Kim J, Iyer G, Al-Ahmadie H, Dulaimi E, Chen DYT, Alpaugh RK, Hoffman-Censits J, Garraway LA, Getz G, Carter SL, Bellmunt J, Plimack ER, Rosenberg JE, Van Allen EM. Mutational patterns in chemotherapy resistant muscle-invasive bladder cancer. Nat Commun. Nature Publishing Group; 2017 Dec 19;8(1):2193.

73. Faltas BM, Prandi D, Tagawa ST, Molina AM, Nanus DM, Sternberg C, Rosenberg J, Mosquera JM, Robinson B, Elemento O, Sboner A, Beltran H,

Demichelis F, Rubin MA. Clonal evolution of chemotherapy-resistant urothelial carcinoma. Nat Genet. 2016 Oct 17.

74. Kardos J, Wobker SE, Woods ME, Nielsen ME, Smith AB, Wallen EM, Pruthi RS, Hayward MC, McGinty KA, Grilley-Olson JE, Patel NM, Weck KE, Black P, Parker JS, Milowsky MI, Hayes DN, Kim WY. Comprehensive Molecular Characterization of Urachal Adenocarcinoma Reveals Commonalities With Colorectal Cancer, Including a Hypermutable Phenotype. JCO Precision Oncology. 2017 Jul;(1):1–12.